NOVA SCHOOL OF SCIENCE & TECHNOLOGY

DEPARTMENT OF ELECTRICAL AND COMPUTER ENGINEERING

FÁBIO JOSÉ DA ENCARNAÇÃO GREGÓRIO

BSc in Electrical and Computer Engineering

THERMOELECTRIC-STRUCTURAL ANALYSIS OF AN AXIAL FLUX SUPERCONDUCTING MOTOR

MASTER IN ELECTRICAL AND COMPUTER ENGINEERING

NOVA University Lisbon
March, 2022

NOVA SCHOOL OF
SCIENCE & TECHNOLOGY

DEPARTMENT OF ELECTRICAL
AND COMPUTER ENGINEERING

THERMOELECTRIC-STRUCTURAL ANALYSIS OF AN AXIAL FLUX SUPERCONDUCTING MOTOR

FÁBIO JOSÉ DA ENCARNAÇÃO GREGÓRIO

BSc in Electrical and Computer Engineering

Adviser: Roberto André Henrique de Oliveira
Researcher, University of Bath

Co-adviser: João Miguel Murta Pina
Assistant Professor, NOVA University Lisbon

Examination Committee

Chair: João Almeida das Rosas
Assistant Professor, NOVA University Lisbon

Rapporteur: Anabela Monteiro Gonçalves Pronto
Assistant Professor, NOVA University Lisbon

MASTER IN ELECTRICAL AND COMPUTER ENGINEERING

NOVA University Lisbon
March, 2022

Thermoelectric-Structural Analysis of an Axial Flux Superconducting Motor

This document was created with the (pdf/Xe/Lua)LaTeX processor and the NOVAthesis template (v6.9.4) Lourenço, 2021.

Acknowledgements

The delivery and defense of this dissertation is one of the most important moments of my life. This would not be possible without the support and help of some people that I will list in the next paragraphs.

To my advisers, Dr. Roberto Oliveira and Prof. João Murta Pina for the opportunity to work on this interesting and challenging dissertation and for the advice and support given during the course of the dissertation.

To Prof. Isabel Catarino for the small but precious contribution in the section of cryogenics.

To Prof. Anabela Pronto for giving me the opportunity to be a monitor in the subject of Electromechanical Energy Conversion.

À minha família, meus pais e avós, com quem sempre cresci. Aos meus pais por sempre terem procurado dar-me o melhor possível dentro das suas possibilidades, nunca me deixando de transmitir os melhores valores e educação. Aos meus avós, por me terem criado e pelos bons momentos na minha infância. Indubitavelmente sem a educação, valores e confiança nas minhas capacidades transmitidos quer pelos meus pais, quer pelos meus avós, jamais teria chegado até aqui.

Ao meu melhor amigo, Henrique Caldeira, que sempre "aturou" o meu pessimismo e que sempre teve uma palavra amiga nos cafés e saídas que me convidava para "espairecer".

À minha amiga também muito especial, Daniela Sousa, pelas palavras de apoio e bons momentos, quer presenciais, quer à distância e por ter sempre acreditado que eu conseguiria chegar aqui.

Aos meus companheiros do Núcleo de Fotografia, em especial, Hugo Calhau e Paulo Maciel pelos momentos de lazer e diversão a fazer o que mais gostamos: fotografar.

Não posso também deixar de mencionar também quem me apoiou, embora mais à distância, porém sem nenhum demérito: Adriana Reino, Daniel Sousa, Daniela Muntean, Edgar Filipe e Maria Carvalho.

Por fim, às outras pessoas que direta ou indiretamente também contribuíram para a realização desta dissertação, um muito obrigado!

"If I have seen further it is by standing on the shoulders of Giants." (Isaac Newton)

Abstract

The growing environmental concerns to reduce global warming caused by the high levels of CO_2 expelled to the atmosphere have played an important role in the electrification of combustion machines. Following this trend, superconducting machines have proved to be an interesting option, because they allow a higher current density. However, the superconducting compounds require cryogenic operating temperatures. This becomes a problem, because, during its working, the machine operation temperature tends to be increased, heat up due to the losses. With that, the losses study becomes a relevant topic to be studied.

In this work, a partially superconducting machine will be analyzed, through an electromagnetic, thermal, and structural finite element simulation of its conventional stator.

The superconducting electrical machine studied is an axial flux machine with a disc rotor made of second-generation high-temperature superconducting (2G HTS) strips and two ferromagnetic conventional semi-stators. This study is focused on the losses of these last ones because the superconducting strips have minimal losses compared to the semi-stators ones.

It is concluded that the semi-stators losses are inversely proportional to the pole number and that the stator lamination typology with fewer losses is circularly laminated.

Keywords: superconductivity, axial flux machines, superconducting machines, electromagnetic losses, thermal losses, structural analysis

Resumo

As crescentes preocupações com o meio ambiente com vista à diminuição do aquecimento global causado pelas altas taxas de CO_2 expelidos para a atmosfera, têm tido um papel importante na eletrificação de máquinas anteriormente predominantemente de combustão. Seguindo esta tendência, as máquinas supercondutoras revelaram-se uma opção interessante, pois possibilitam uma densidade de corrente superior. No entanto, os materiais supercondutores requerem temperaturas criogénicas. Isto torna-se um problema, pois durante o seu funcionamento a máquina tende a aquecer devido às perdas. Com isto, o estudo de perdas torna-se um tópico relevante de ser estudado.

Neste trabalho, será alvo de estudo uma máquina parcialmente supercondutora através de uma análise de elementos finitos no plano eletromagnético, térmico e estrutural do seu estator convencional.

A máquina elétrica supercondutora analisada é de fluxo axial com um rotor em disco constituído por fitas supercondutoras de alta temperatura de segunda geração (2G SAT) e dois semi-estatores ferromagnéticos convencionais. Este estudo é apenas concentrado nas perdas destes últimos, pois as fitas supercondutoras as perdas são mínimas comparativamente com as dos semi-estatores.

É concluido que as perdas no semi-estatores são inversamente proporcionais ao número de pólos e que a topologia de laminação do estator com menores perdas é a circularmente laminada.

Palavras-chave: supercondutividade, máquinas de fluxo axial, máquinas supercondutoras, perdas eletromagnéticas, perdas térmicas, análise estrutural

Contents

List of Figures

List of Tables

Acronyms

(RE)BCO	Rare earth barium cooper oxide 4, 9, 43
AC	Alternating Current xx, 9, 12–14, 16, 27, 28, 55, 61, 63, 68–71
AFIR	Axial Flux Interior Rotor 32, 52
AFM	Axial Flux Machines xviii, 31, 32, 37
AFSM	Axial Flux Superconducting Motor xix–xxi, 1, 2, 52–55, 57–59, 61–69, 71, 72, 81–85
AMSC	American Superconductor xvii, xviii, 13–17, 25
ASCEND	Advanced Superconducting & Cryogenic Experimental Powertrain Demonstrator xviii, 26
BSCCO	Bismuth strontium calcium cooper oxide 4, 9, 12, 13, 20, 25, 28
CTS-UNINOVA	Centre for Technologies and Systems of UNINOVA 1, 52
DC	Direct Current 12–14, 16, 23, 28
DSSR	Double-Stator Single-Rotor 27, 32, 52
FCL	Fault Current Limiters 10, 15
FEM	Finite Elements Method xix, xxi, 2, 41–45, 47, 49, 51, 55, 59, 71
FSCM	Fully Superconducting Machines xiv, xviii, 27, 28
GM	Gifford-McMahon 23
HTS	High Temperature Superconducting xiii, xvii, xviii, xxi, 1, 4, 5, 9–14, 17, 18, 20, 24, 25, 27–30, 33, 43, 52, 53, 55, 56
ICMAB-CISC	Institute of Materials Science of Barcelona 52, 53
IFW-Dresden	Leibniz Institute for Solid State and Materials Research Dresden 17

LBCO Lanthanum barium cooper oxide 4

LTS Low Temperature Superconducting xvii, xxi, 4, 10, 13, 19, 20, 23, 24

Maglev Magnetic levitation train 17

PSCM Partially Superconducting Machines xiv, xviii, 27, 28, 31, 32, 43, 52

RFM Radial Flux Machines 27, 31, 32

SFCL Superconducting Fault Current Limiters xvii, 15–17

SMES Superconducting Magnetic Energy Storage xvii, 10, 12, 13

SSDR Single-Stator Double-Rotor 27, 32

SSSR Single-Stator Single-Rotor 27, 32

SUPRAPOWER Superconducting, Reliable, lightweight, and more powerful offshore wind turbine xviii, 25, 26

UEx University of Extremadura 52

UFRJ Federal University of Rio de Janeiro 18

YBCO Yttrium barium cooper oxide 1, 4, 9, 12, 13, 18, 20, 28, 52, 53

Symbols

A_c	Area normal to the conduction flow path direction [m^2] 37
$A_{s,max}$	Maximum stator load current [A] 10
A_c	Area of the current flow [m^2] xvii, 7
$\mathbf{A_n}$	Nodal magnetic vector potential [$V.s.m^{-1}$] 48
D_{avg}	Average diameter of the semi-stator [m] 54, 55
p_{avg}	Average perimeter of the semi-stator [m] 54
$\overline{P_{cr}}$	Steady-state semi-stators average core AC losses [W] 68, 69
$\mathbf{B_{ex}}$	Expelled flux vector [T] xvii, 8
$B_{g,max}$	Maximum airgap flux density strength [T] 10
$\mathbf{B_{tr}}$	Trapped flux vector [T] xvii, 8
$\mathbf{B}$	Magnetic flux density vector [T] xviii, 6, 35, 47, 48
B_{max}	Maximum magnetic flux density [T] 30, 35, 36
T_B	Body temperature [K] 49
B_r	Remnant magnetic flux density [T] 36
B_{sat}	Saturation magnetic flux density [T] 35
B_x	Magnetic flux density x-component [T] 48
B_y	Magnetic flux density y-component [T] 48
c	Width of each semi-stator slot [m] 54, 55
$[c_p]$	Specific heat matrix [J/kg.K] 50
λ_i	Coating thickness [m] 35
A_{cold}	Cold surface area [m^2] 39
$\mathcal{S}_c$	Conduction area [m^2] 49
k_v	Convection coefficient [W/m.K] 38, 57
$\mathcal{S}_v$	Conduction area [m^2] 49
P_{cr}	Core losses [W] 34
λ_c	Laminated core plate thickness [m] 35
T_{cr}	Cryoliquid critical temperature [K] 19, 20

$\mathbf{v_c}$	Current velocity vector [m/s] 48
I	Current [A] xviii, 6, 34, 35
$\mathbf{D}$	Electric flux density vector [C/m^2] 47
δ_x	Displacement x-component [m] 48
δ_y	Displacement y-component [m] 48
δ_{sc}	Current penetration depth of the superconducting wire [m] xvii, 6, 7
$\mathcal{D}$	Density [kg/m^3] 49, 57
$\mathbf{E}$	Electric field vector [V/m] 47
$\mathbf{I_{ed}}$	Eddy current vector [A] xviii, 35
P_{ed}	Eddy current losses [W] 34, 35
η	Efficiency [%] 33
$[N(x,y,z)]$	Element shape functions matrix regarding the space 49
$\epsilon_{\mathbf{el}}$	Elastic strain vector 52
V_n	Nodal electric scalar potential [V] 48
P_{em}	Electromagnetic losses [W] 33, 34
e	Surface emissivity 38
ε_{cold}	Cold surface emissivity 39
ε_{hot}	Hot surface emissivity 39
E_x	Magnetic flux density x-component [V/m] 49
E_y	Magnetic flux density y-component [V/m] 49
$F_{hot,cold}$	Shape factor associated to the relative orientation of the two gray surfaces 39
$\mathbf{F_{el}}$	Electrostatic force vector [N] 48
C	Finite elements domain boundary xix, 41, 42, 44
$\mathbf{\Delta_1}$	Displacement vector of the element 1 [m] 45
$\mathbf{\Delta_m}$	Displacement vector of the element m [m] 43, 47
δ_{mn}	Displacement vector of the n-th node of the m-th element [m] xxi, 45, 47
δ_1	Displacement component of the node 1 [m] 46
δ_2	Displacement component of the node 2 [m] 46
δ_3	Displacement component of the node 3 [m] 46
$\mathbf{\Delta}$	Displacement vector [m] 43
Γ	Finite elements domain xix, 41, 42, 44–46
$\mathbf{F_1}$	Force vector of the element 1 [N] 45
$\mathbf{F_m}$	Force vector of the element m [N] 43, 47
f_{mn}	Force vector of the n-th node of the m-th element [N] xxi, 45, 47
f_1	Force component of the node 1 [N] 46
f_2	Force component of the node 2 [N] 46
f_3	Force component of the node 3 [N] 46

$\mathbf{F}$	Force vector [N] 43
$[K_1]$	Stiffness matrix of the element 1 46
$[K_m]$	Stiffness matrix of the element m 43
n	Element node 47
N_n	Total number of nodes of the domain D 41, 43, 46, 48
K_2	Stiffness matrix of the Element 1 46
K_2	Stiffness matrix of the sub-domain 2 46
$[K]$	Stiffness matrix 43
Γ_m	Finite elements sub-element m 47
Γ_1	Finite elements element 1 xix, 45–47
Γ_2	Finite elements element 2 xix, 46, 47
N_m	Total number of elements of the domain D xix, 41–43, 45
f	Operating frequency [Hz] 35, 36, 58
H_{c1}	Lower critical magnetic field [A/m] 8
H_{c2}	Upper critical magnetic field [A/m] 8
H	Magnetic field strength [H] 35
$\mathbf{H}$	Magnetic field vector [A/m] 6, 47
H_c	Critical magnetic field [A/m] 5–8
$H_c(0)$	Critical magnetic field at absolute zero (0 K) [A/m] 6
ΔP_c	Rate of heat transferred by conduction [W] 37
ΔP_v	Rate of heat transfer by convection [W] 38
$\phi_{\mathbf{q}}$	Heat flux vector [W/m^2] 49
ΔP_r	Rate of heat transfer by radiation [W] 38
ΔP_{rn}	Net rate of heat transfer by radiation [W] 39
$\boldsymbol{\Delta}\ddot{\mathbf{Q}}$	Heat generation rate per unit volume [W/m^3] 49
$\mathbf{v_h}$	Heat velocity vector [m/s] 49
$\mathbf{H_g}$	Generalized magnetic field vector [A/m] 47
A_{hot}	Hot surface area [m^2] xix, 38, 39
$\mathbf{H}_\phi$	Gradient of the generalized magnetic field potential vector [A/m] 47
n	Power constant for the hysteresis losses 30, 36
τ_h	Hysteresis torque [N. m] 30
P_h	Hysteresis losses [W] 34–36
$i_{sc}(t)$	Resistive SFCL time-vary fault current [A] 15
I_c	Critical current [A] 6, 15, 16
D_{in}	Inner diameter of the semi-stator [m] 54, 55
$\mathcal{S}$	Body surface area [m^2] 48
$\mathcal{V}$	Body volume [m^3] 48, 49
$[K]^{-1}$	Inverse stiffness matrix 52

J_n	Nodal current density [A/m^2] 49
$\mathbf{J}$	Current density vector [A/m^2] 47, 48
J_c	Critical current density [A/m^2] 7
$\dddot{Q}$	Joule heat per unit volume [J/m^3] 49
$[K_C]$	Convection surface conductivity matrix 50
$[K_D]$	Diffusion conductivity matrix 50
k_{ed}	Proportionality constant for the eddy current losses 35
k_h	Proportionality constant for the hysteresis losses 36
k_i	Laminated core stacking factor 35, 56, 57
$[K_T]$	Mass transport matrix 50
l_c	Conduction flow path length [m] xix, 37
L	Latent heat of vaporization [kJ/Kg] 19, 20
$\mathbf{F_{jb}}$	Lorentz force vector [N] 48
$\dot{m}$	Internal cooling mass flow [Kg/s] 22
$\mathbf{M}$	Magnetization vector [A/m] 6
$\phi_{\mathbf{m}}$	Magnetic flux vector [Wb] xix, 45
$\mathbf{A}$	Magnetic vector potential [V.s.m^{-1}] xix, 44, 45
ϵ	Strain 50
σ	Stress [Pa] 50
d	Material bar height [m] 50
L	Material bar length [m] 50
b	Material bar width [m] 50
$\mathbf{F_{mx}}$	Maxwell force vector [N] 48
P_{mec}	Mechanical losses [W] 33, 34
$[\mu]$	Permeability matrix 48
$[N]$	Element shape function matrix 47
$[N_A]$	Element shape functions for the magnetic vector potential 48
ΔT_n	Nodal temperature variation [K] 49
$[N_V]$	Element shape functions for the electric scalar potential 48
P_{oh}	Ohmic losses [W] 34
D_{out}	Outer diameter of the semi-stator [m] 54, 55
P_{in}	Power input [W] 33
P_{out}	Power output [W] 10, 33

ε_0	Vacuum permittivity [8.8542×10^{-12} F/m] 49
$[\varepsilon]$	Permittivity matrix [F/m] 48
ν	Poisson ratio 50, 51, 57
p	Number of poles 45
$\mathbf{Q_C}$	Convection surface heat flow vector 50
$\dot{q}_{circ}$	Heat generated by the pump or compressor [J] 22
$\mathbf{Q_F}$	Mass flux vector 50
$\mathbf{Q_H}$	Heat generation load vector 50
$\dot{q}_{ref}$	Heat generated by the refrigerator [J] 22
R_p	Resistive SFCL parallel resistance [Ω] 15
R_{sc}	Resistive SFCL superconducting resistance [Ω] 15
r_w	Wire radius [m] xvii, 7
$[\mathcal{R}]$	Reluctance matrix 48
ρ	Resistivity [$\Omega.m$] 34, 57
$[\rho]$	Resistivity matrix 48
ρ_0	Resistivity at T_0 [$\Omega.m$] 34
$U_{in,rms}$	RMS input voltage [V] 58
r_m	Rotating machine radius [m] 45
N_r	Rotation speed [rpm] 10
S_l	Resistive SFCL switch 15
A_G	Shear load tangential area [m^2] 51
F_G	Shear load [N] 51
γ	Shear strain 51
τ	Shear stress [N/m^2] 51
G	Shear modulus 51
G_{xy}	Shear modulus xy-component 52
G_{xz}	Shear modulus xz-component 52
G_{yz}	Shear modulus yz-component 52
s	Slip [%] 56
c_p	Specific heat [J/kg.K] 49, 57
k_{sb}	Stefan-Boltzmann constant [5.6697×10^{-8} $W/m^2.K^4$] 38
$P_{cr,st}$	Semi-stators core AC losses [W] 55, 63
$\epsilon_{30,max}$	Semi-stators maximum strain at 30 seconds of operation 68, 69
$\sigma_{30,max}$	Semi-stators maximum stress at 30 seconds of operation [Pa] 68, 69
ϵ_{st}	Semi-stators strain 55
σ_{st}	Semi-stators stress [Pa] 55
T_{st}	Semi-stators temperature [K] 55

ΔT_{30}	Semi-stators temperature variation at 30 seconds of operation [K] 68, 69
τ_{m0}	Start torque [N · m] 30
F_σ	Stress load [N] xix, 51
A_σ	Stress load area [m^2] xix, 51
σ	Stress vector [Pa] 52
N_s	Synchronous speed [rpm] 30
T_b	Boiling temperature at 1 atm [K] 19, 20
T_{cold}	Temperature of the cold-temperature region [K] 37–39
T_{hot}	Temperature of the high-temperature region [K] 37–39
T_c	Critical temperature [K] xviii, 4–7, 19, 20, 32
T	Temperature [K] 32, 34, 38
T_0	Initial temperature [K] 34
α	Thermo-resistivity coefficient [K^{-1}] 34, 57
$T(x,y,z,t)$	Temperature as space and time function [K] 49
$\mathbf{T_n(t)}$	Time vary nodal temperature vector [K] 49
$[k_c]$	Thermal conductivity matrix W/m.K] 49
$\epsilon_{\mathbf{th}}$	Thermal strain vector 52
k_c	Thermal conductivity [W/m.K] 37, 55
P_{th}	Thermal losses [W] 33, 34, 36
μ_0	Magnetic permeability in the vacuum [$4\pi \times 10^{-7}$H/m] 6
V_r	Rotor active volume [m^3] 10
$[d_v]$	Virtual displacement of the nodes [m] 48
$\mathbf{F_s}$	Virtual force vector [N] 48
A_w	Wire cross area [m^2] xviii, 34, 35
l_w	Wire length [m] xviii, 34, 35
R_w	Wire resistance [Ω] 34
χ_m	Magnetic susceptibility 6
Y	Young's modulus 50, 57, 67

Chemical Symbols

$Bi_2Sr_2Ca_2Cu_3O_{10}$	Bismuth strontium calcium cooper oxide 4, 9
Gd	Gadolinium 4
H_2	Hydrogen 20
He	Hellium 3, 4, 20
Hg	Mercury xvii, 3, 4
LaBaCuO	Lanthanum barium cooper oxide 4
LHe	Liquid helium 19, 20
LN_2	Liquid nitrogen 1, 13, 14, 16, 17, 20, 61, 72
MgB_2	Magnesium diboride xviii, 4, 20, 25, 28
N_2	Nitrogen 4, 20
Nb_3Sn	Niobium–tin 4, 10, 19
NbTi	Niobium–titanium 4, 10, 19, 23
Nd	Neodymium 4
Ne	Neon 20
O_2	Oxygen 20
Sm	Samarium 4
Y	Yttrium 4
$YBa_2Cu_3O_7$	Yttrium barium cooper oxide 4

1 Introduction

1.1 Motivation

Nowadays, more and more electrical machines play an important role in society due to the growing environmental concerns. The combustion machines use fossil energy as fuel and produce high levels of CO_2 to the atmosphere. Hence, even more, the combustion machines are being replaced by electrical machines.

The development of electrical machines searches for the highest efficiency and compactness. Aiming these two goals, superconductivity applied to electrical machines has become an attractive concept. The higher current density and fewer power losses provided by the superconducting compounds led to more compactness and efficient machines, respectively.

To reach the superconducting state, the material must be under a critical temperature which is 77 K in High Temperature Superconducting (HTS) case. This temperature only can be reached recurring to cryogenic methods such as cryoliquids like LN_2 or cryocoolers. So, the operating temperature of the superconducting machines must be maintained at a cryogenic level. This becomes a problem because the electrical machine tends to heat up during operation.

The analysed machine in this dissertation is an Axial Flux Superconducting Motor (AFSM), which is under development in Centre for Technologies and Systems of UNINOVA (CTS-UNINOVA). Its rotor is made of HTS 2G YBCO tapes, while the semi-stators core is made of conventional ferromagnetic material. The machine is immersed in liquid nitrogen (LN_2) at −196.15 °C (77 K) to keep the tapes in the superconducting state. Due to the superconducting lower losses, the main source of the machine losses, and consequently its heat, is the stator. The machine heat causes the LN_2 evaporation. Another consequence of the stator heat is its deformation which causes an irregular deformation of the machine airgap.

For that reason, a thermoelectric-structural analysis of the AFSM stator losses becomes an important topic to be studied. Moreover, in this analysis, a few stator lamination and pole configurations must be analyzed to find the most attractive machine setup. To make

the first approach of this analysis, a computer performed Finite Elements Method (FEM) simulation is a rather valid solution, due to the low cost when compared with prototype tests.

1.2 Objectives

This dissertation aims to achieve the following objectives:

- Perform electromagnetic, thermal and structural FEM simulations with Ansys Electronics Desktop, Mechanical and Workbench, for a AFSM 2D linearized model;
- Analyze different AFSM stator lamination topologies and pole configuration;
- Draw conclusions about the most advantageous pole configuration and lamination topology regarding electromagnetic and thermal losses and deformation.

1.3 Original Contributions

The analysis and optimization through the losses and structural analysis is a topic never explored before in this machine. With that, must be concluded which configuration presents the fewer stator losses and distortion. This can form the basis to define which configuration is the most advantageous to proceed to prototype test. The obtained data can be used also to dimension the AFSM cryogenic system.

1.4 Dissertation Organization

This dissertation is organized in five chapters:

- **Chapter 1: Introduction** - the present chapter of Introduction;
- **Chapter 2: Literature Review/State of the Art** - literature review about superconductivity, cryogenic systems, superconducting machines, machine losses and FEM. A state of the art about superconducting applications and machines is also done;
- **Chapter 3: Methodology** - detailed description of the analysed machine, simulation conditions and parameters;
- **Chapter 4: Simulation Results and Discussion** - presentation of the obtained results;
- **Chapter 5: Conclusions and Future Work** - reflection about the obtained results and future work.

2

Literature Review/State of the Art

2.1 Superconductivity

2.1.1 Introduction

The history of superconductivity begins long before its discovery. The search for methods to reach the absolute zero by liquefaction was one of the main challenges for the scientists of the 19th century. In 1908, Karmeling-Onnes, reached the liquefaction of the helium (He) (Rogalla & Kes, 2011). In 1911, the same person measured the temperature of mercury (Hg) throughout its cooling (figure 2.1) and discovered a particular phenomenon that won him the 1913 Nobel Prize in Physics (Onnes, 1913):

> *The mercury at 4.2 K has entered a new state, which, owing to its particular electrical properties, can be called the state of superconductivity.*
>
> — Kamerlingh-Onnes, Nobel Lecture, December 11, 1913

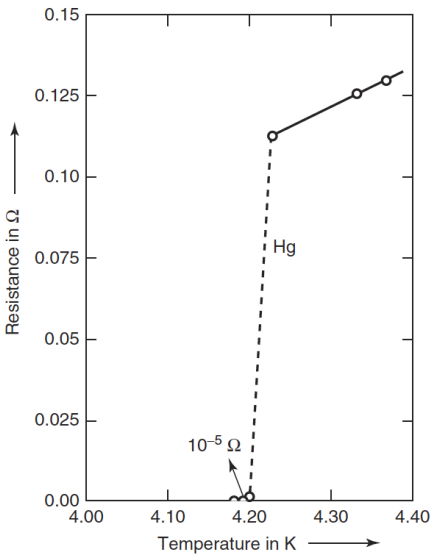

Figure 2.1: Temperature vs. resistance of the Hg (Kleiner & Buckel, 2016).

The "particular electrical properties" described by Onnes is the zero electrical resistance. As can be seen in the figure 2.1, the Hg resistivity at 4.2 K is insignificant. This behavior was never been seen in any material until then (Kleiner & Buckel, 2016; Rogalla & Kes, 2011). With that, the definition of superconductivity was established as the capability of certain compounds to exhibit zero resistivity below a critical temperature (T_c).

In 1933, the second characteristic of superconductors was discovered by Walther Meissner and Robert Ochsenfeld: the perfect diamagnetism. This characteristic makes a complete expulsion of the magnetic field that tries to enter the superconductor material and it is called Meissner effect (Thinkham, 1996). The theoretical explanation of this phenomenon was done by Fritz and Heinz London, in 1935, resulting in the London equations (London & London, 1935). Nevertheless, the entire theoretical superconducting understanding was formulated in 1957 by John Bardeen, Leon Neil Cooper, and John Robert Schrieffer resulting in the BCS theory (Kleiner & Buckel, 2016; Poole Jr., Farach, Creswick, & Prozorov, 2007).

However, the major issue of the superconductivity was still the low temperatures required by this state. Although, the first superconducting applications prototypes appeared in the 1960s using superconducting compounds like niobium-titanium and niobium-tin (NbTi and Nb_3Sn, respectively). The T_c of both compounds is 9.2 and 18 K, respectively. The refrigeration liquid chosen was the He. But, this solutions had the drawback of the economical infeasibility due to the difficult to put He at 4.2 K (Gieras, 2008; Malozemoff, 2012; Rogalla & Kes, 2011).

In 1986, thanks to George Bednorz and Karl Alexander Müller, an high transition temperature of 30 K was registered in lanthanum barium cooper oxide (LaBaCuO or LBCO) compound (Bednorz & Miiller, 1986). This was the first step of the High Temperature Superconducting (HTS) era. Right after, the yttrium barium cooper oxide ($YBa_2Cu_3O_7$ or YBCO) and bismuth strontium calcium cooper oxide ($Bi_2Sr_2Ca_2Cu_3O_{10}$ or BSCCO) compounds were discovered, with T_c of 93 and 105 K, respectively (figure 2.2). In both compounds the transition temperatures are above the nitrogen (N_2) boiling temperature which is 77 K (Kleiner & Buckel, 2016). Due to this fact, the energy and effort required by the HTS cooling are much lower than the Low Temperature Superconducting (LTS) like NbTi and Nb_3Sn (Gieras, 2009). Later, the YBCO compound was expanded to a larger group called (RE)BCO where RE means rare earth elements such as neodymium (Nd), samarium (Sm), gadolinium (Gd) or indeed ytrium (Y) itself (Melhem, 2012).

For many years the Yttrium barium cooper oxide (YBCO) and Bismuth strontium calcium cooper oxide (BSCCO) were the most used HTS compounds until 2001, when the magnesium diboride (MgB_2) was introduced. Although its T_c of 39 K is much lower than either YBCO and BSCCO, the manufacturing of tis compound is cheaper and easier than the others (Ballarino & Flükiger, 2017). The classification of MgB_2 as HTS compound is not consensual. Some authors does not consider the MgB_2 an HTS because its T_c is above the nitrogen boiling temperature which is 77 K (Pina, 2010b).

With the HTS compounds, the superconductivity could be applied much more easily

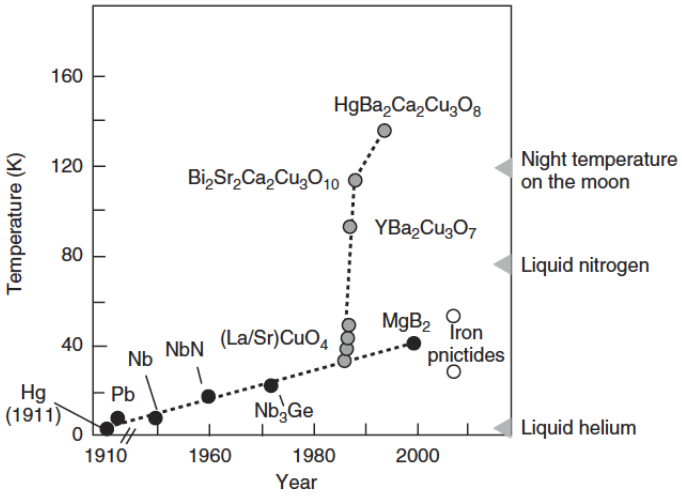

Figure 2.2: Evolution of the superconducting critical temperature since the discovery of superconductivity in 1911 (Kleiner & Buckel, 2016)

than before. Currently, most of the power superconducting devices use HTS compounds. These are described in more detail in section 2.1.5.

2.1.2 Definition and properties

Superconductivity is a phenomenon of perfect conductivity and diamagnetism that occurs in some materials when cooled below the critical temperature (T_c). To achieve the necessary temperatures and maintain them, cryogenic systems are necessary. These ones are described in the section 2.2.

When a material is in the superconducting state, not only exhibits perfect conductivity but also expels the magnetic field. This phenomenon of perfect diamagnetism is called Meissner effect (figure 2.3). As long as the magnetic field does not exceed its critical value (H_c), the induction inside the material is zero, except in the boundaries (Kleiner & Buckel, 2016).

(a) Conducting (or normal) state.

(b) Superconducting state.

Figure 2.3: Meissner effect. In the conducting state, the flux lines cross normally the material. In the superconducting state, the flux lines are moved away by the material, except in the boundaries (Gieras, 2008).

The flux density vector (**B**) inside the superconductor is given by:

$$\mathbf{B} = \mu_0 \cdot (\mathbf{H} + \mathbf{M}) \tag{2.1}$$

where μ_0 is the vacuum permeability, **H** the magnetic field applied vector and **M** the magnetization vector (Poole Jr. et al., 2007). Due to the Meissner effect, inside the superconductor, **B** is equal to 0. Replacing it in the equation 2.1:

$$\mathbf{H} = -\mathbf{M} \tag{2.2}$$

So, the magnetic field and the magnetization are equal in absolute value, but with opposite signs, which results in magnetic susceptibility (χ_m) of −1. Thus, this proves the perfect diamagnetism of the superconductors (Poole Jr. et al., 2007). In other words, the superconductors produce a magnetization opposite to the applied magnetic field.

Regarding the critical temperature and magnetic field (H_c) there is a relation between them:

$$H_c(T) = H_c(0) \cdot \left[1 - \left(\frac{T}{T_c}\right)^2\right] \tag{2.3}$$

where $H_c(0)$ represents the value of critical magnetic field in the absolute zero (0 K). As the temperature rises from the absolute zero to T_c, the critical magnetic field (H_c) decreases (figure 2.4). These critical values separate the superconducting state from the normal one.

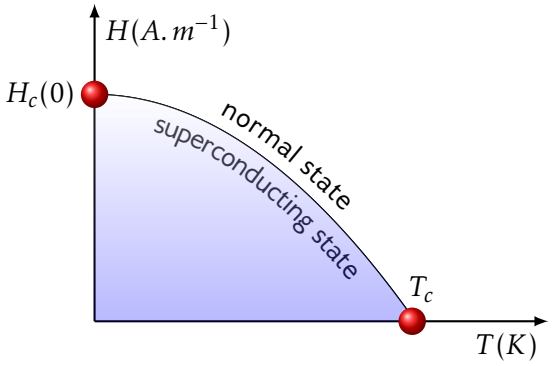

Figure 2.4: Temperature dependence of the critical field (Thinkham, 1996).

Nevertheless, the temperature and the magnetic field are not sufficient conditions to reach the superconducting state. Considering a superconducting wire with current I with flux penetration surface depth of δ_{sc} (figure 2.5). By Ampere's Law, I is given by the equation 2.4 (Pina, 2010a).

$$H = \frac{I}{2 \cdot \pi \cdot r_w} \tag{2.4}$$

Then, from the equation 2.4 the relation between the critical current (I_c) and H_c is:

$$I_c = 2 \cdot \pi \cdot r_w \cdot H_c \tag{2.5}$$

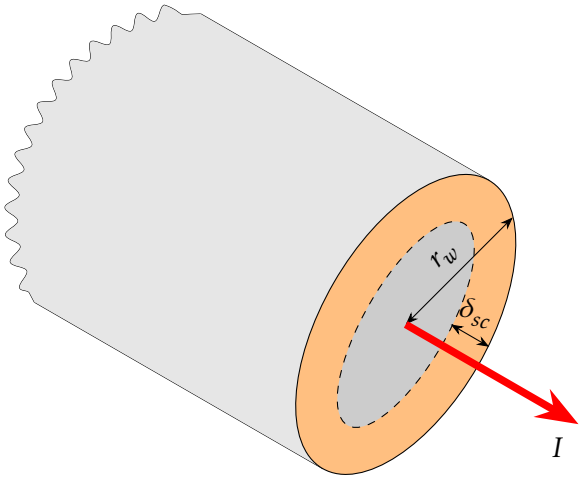

Figure 2.5: Cross section of a superconducting wire. The area of the current flow (A_c) is represented by orange. This figure is not to scale ($\delta_{sc} \ll r_w$).

The area of the current flow (A_c) is given by:

$$A_c = \pi \cdot r_w^2 - \pi \cdot (r_w - \delta_{sc})^2 \tag{2.6}$$

Considering that $\delta_{sc} \ll r_w$ and using the equation 2.5, the relation between the critical density of current (J_c) and H_c can be obtained (Pina, 2010a; Poole Jr. et al., 2007):

$$J_c = \frac{I_c}{A_c} = \frac{I_c}{\pi \cdot r_w^2 - \pi \cdot (r_w - \delta_{sc})^2} \approx \frac{I_c}{2 \cdot \pi \cdot r_w \cdot \delta_{sc}} = \frac{H_c}{\delta_{sc}} \tag{2.7}$$

Thus, it can be concluded that the superconducting state can be summed up to three variables: temperature, magnetic field, and current density. The superconducting state is summarized by the T-H-J diagram (figure 2.6). To be on that, the material needs to be below T_c, H_c and J_c.

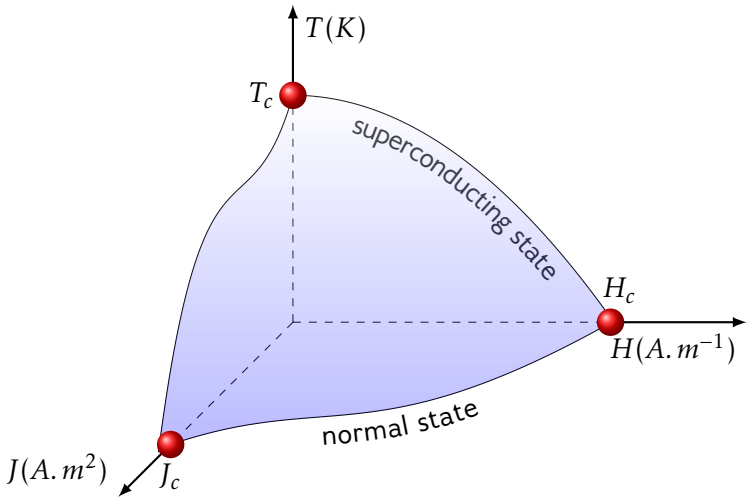

Figure 2.6: The T-H-J diagram. The blue region represents the superconducting state (Pina, 2010a).

2.1.3 Types of Superconductors

There are two types of superconductors: type-I and type-II. In type-I superconductors, the magnetic field is totally expelled by the material when it is below H_c. Above the H_c, the superconductor is in the normal state, i.e., the magnetic field penetrates the material completely (figure 2.7a) (Blundell, 2009; Thinkham, 1996).

The type-II superconductors introduce an intermediate state between normal and superconducting: the mixed state (Abrikosov, 1957). In this type of superconductors, there are two values for the critical magnetic field: upper and lower (H_{c1} and H_{c2}, respectively) (figure 2.7b). That is, the type-II superconductors do not have an abrupt transition between the superconductor and the normal state.

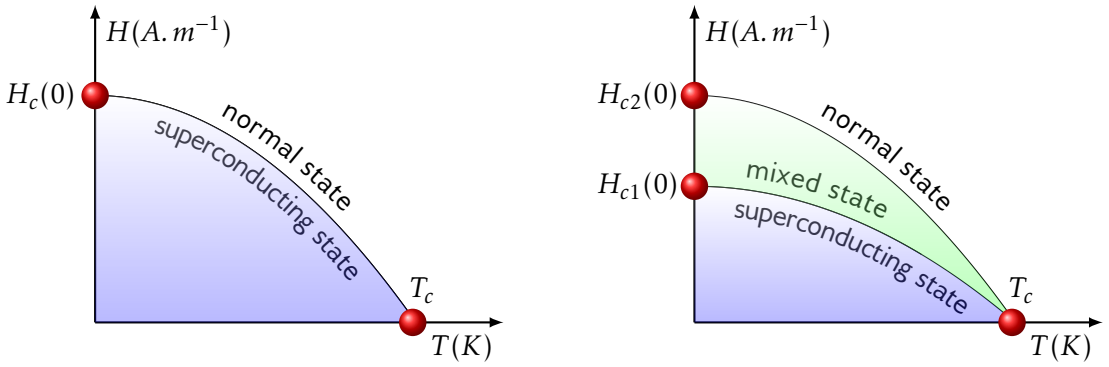

(a) Type I (b) Type II

Figure 2.7: Phase diagram for the two types of superconductors (D. D. P. Inácio, 2014).

The mixed state, consists of a continuous increase in flux penetration, without any loss of superconductivity (figure 2.8). In other words, some of the flux is trapped and some is expelled ($\mathbf{B_{tr}}$ and $\mathbf{B_{ex}}$, respectively).

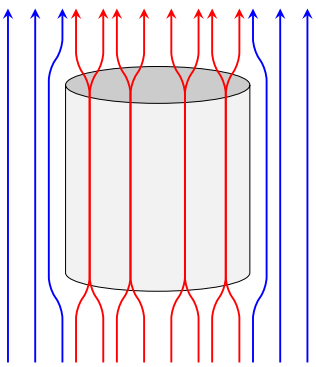

Figure 2.8: Mixed state. The $\mathbf{B_{tr}}$ and $\mathbf{B_{ex}}$ are represented by red and blue, respectively.

The flux penetration is done by a quantum of magnetic flux single tubes triangularly arranged called vortices (Blundell, 2009; Thinkham, 1996). Each one contains current around itself to protect the material superconductor from the magnetic field. The set of fluids inside a superconductor forms an Abrikosov lattice (figure 2.9).

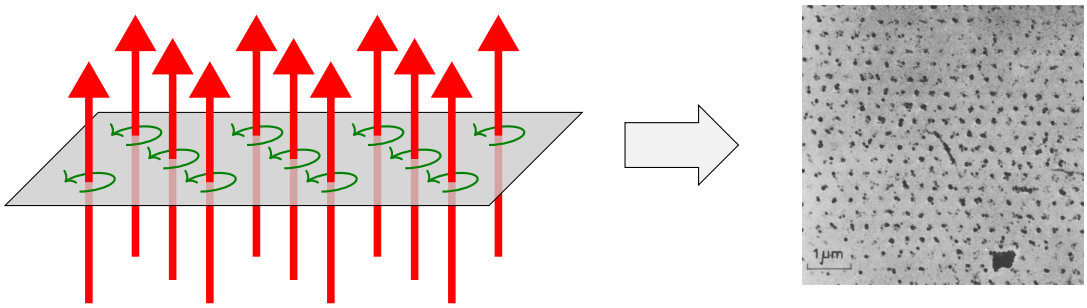

Figure 2.9: Abrikosov lattice. The red arrows represents the trapped magnetic flux triangularly arranged. The vortex circulating current lines are represented by green (Essmann & Trauble, 1964).

2.1.4 HTS Tapes

There are two generations of HTS tapes:

- BSCCO 1G (first generation);
- (RE)BCO 2G (second generation).

The BSCCO 1G HTS tapes are made of $Bi_2Sr_2Ca_2Cu_3O_{10}$ multi-filamentary composite embedded by a silver alloy matrix (figure 2.10a). This HTS tapes allow current density of order 50 kA/cm^2, at 77 K. This generation was used on early demonstrations of electric power equipment and it is commercially available and used today (Malozemoff, 2012).

The (RE)BCO 2G HTS tapes is constituted by coated thin layer between several substrates (figure 2.10b). For example, the YBCO tapes allows current density of order 3000 kA/cm^2 at 77 K, which is 60 times higher than the BSCCO wire. Hence, the YBCO wire has reduced AC losses when compared with the BSCCO (Gieras, 2008; Malozemoff, 2012).

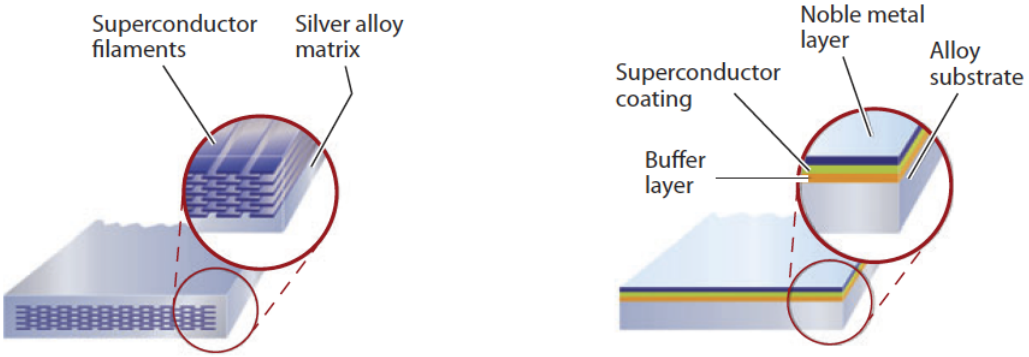

(a) 1G BSCCO wire.

(b) 2G (RE)BCO wire.

Figure 2.10: HTS tapes (Malozemoff, 2012).

Another important issue for the lower cost of the 2G HTS tapes, is the production process. Due to their substrate construction, these tapes can be manufactured in wide

strips and after silted in many tapes. Meanwhile, the 1G tapes must be processed wire by wire (Malozemoff, 2012). Moreover, the 2G HTS tapes have better mechanical properties like flexibility than the 1G HTS tapes (Gieras, 2008).

2.1.5 Applications

The development of superconductivity devices aims at its highest efficiency, smaller size, and reduced weight due to the higher current density provided by the superconductors when compared with the existing technologies. Before the HTS discovery, many practical applications of superconductivity have appeared using LTS such as NbTi and Nb_3Sn. However, as mentioned in section 2.1.1, these solutions were not feasible. Thus, the discovery of the HTS materials was an important achievement to apply superconductivity to practical applications.

The superconductivity can be employed in many practical applications such as (Gieras, 2008; Malozemoff, 2012; Rogalla & Kes, 2011):

- Electrical machines;
- Transformers;
- Superconducting Magnetic Energy Storage (SMES);
- Transmission cables;
- Fault Current Limiters (FCL);
- Electric vehicles.

2.1.5.1 Electrical Machines

The power output of a rotating machine (P_{out}) is given by the following proportionality relation (Vajda, Szalay, Göbl, Meerovich, & Sokolovsky, 1999):

$$P_{out} \propto B_{g_{max}} \cdot A_{s_{max}} \cdot N_r \cdot V_r \tag{2.8}$$

where $B_{g,max}$ is the maximum airgap flux density strength, $A_{s,max}$ is the maximum stator linear current, N_r is the machine rotation speed and V_r rotor active volume. In conventional machines, $B_{g,max}$ is limited by the saturation of the rotor and stator ferromagnetic core. So, the higher current density provided by the superconductors lead to a higher magnetic flux density in the machine airgap, and consequently to a torque increase (Gieras, 2008; Haran et al., 2017; Melhem, 2012). In conventional machines, the current density is $3-5\,A/mm^2$, while in superconducting machines is about at least $200\,A/mm^2$ (Melhem, 2012). So, according to equation 2.8, the power of a superconducting machine is higher than the conventional counterpart. This made the employment of superconductivity attractive in electrical machines.

Another consequence of the higher current density provided by the superconducting windings is the reduction of the machine size and weight for the same power machine (Haran et al., 2017; Rogalla & Kes, 2011). To get an idea, the superconducting machines can be 30% of the conventional counterpart size (Melhem, 2012). Getting a 10 MW generator as example, in figure 2.11, the impact on machine size and weight that the use of superconductivity in electrical machines brings is represented (Jensen & Masson, 2012). Furthermore, the more compact and weightless structure of the superconducting machines led to a reduction of the machine moment of inertia. This can be a problem because the transient response of the machine can be inhibited (Haran et al., 2017).

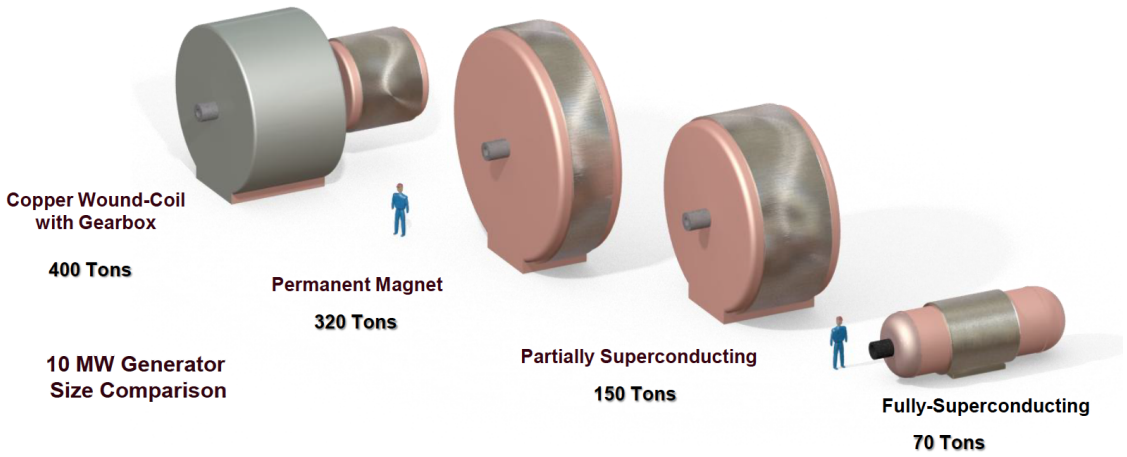

Figure 2.11: Size and weight comparison for a 10 MW generator (Jensen & Masson, 2012).

Although the superconducting machines have lower life-cycle costs and consequently reduced capital costs than the conventional ones, this technology is still more expensive due to the superconducting wires and cryogenic systems of refrigeration cost. Another important issue relative to the cryogenic systems is its reliability. The correct operation of the superconducting machine depends on the cryogenic systems of refrigeration which are fundamental to maintain such temperatures (Haran et al., 2017). The superconducting machines are more detailed in section 2.3.

2.1.5.2 Transformers

The superconducting transformers have enhanced efficiency, weight, and size due to the low superconducting losses and high current density. In addition, this type of transformer can run in an overloaded condition without impacting insulation life (Rogalla & Kes, 2011).

The use of coolant in the superconducting transformers instead of oil as in the conventional ones eliminates the risk of fire. One drawback is the need for coupling to a current limiter because of the low impedance caused by this type of transformer (Malozemoff, 2012). The primary and secondary of the current HTS transformers are made

of superconducting coils, constituted by HTS tape-shaped wires arranged vertically or horizontally (Malozemoff, 2012).

There are many projects of superconducting transformers, using HTS 1G BSCCO and, more recently, HTS 2G YBCO tapes. In 2001, Siemens built and demonstrated a single-phase 25 kV/1.4 MVA traction transformer operating at 67 K using BSCCO tapes (figure 2.12a) (Meinert, Henning, Schlosser, & Leghissa, 2002; Staines, Jiang, Glasson, Buckley, & Pannu, 2015). The Nakoya University, in Japan, is developing a YBCO superconducting transformer which operates as a fault current limiting (figure 2.12b). A single-phase 22 kV/6.6 kV, 0.67 MVA demonstrator for a three-phase 22 kV/6.6 kV, 2 MVA transformer was built in 2010 (Kotari, Kojima, Hayakawa, Endo, & Okubo, 2010; Staines et al., 2015).

(a) Siemens BSSCO single-phase traction transformer (Meinert, Henning, Schlosser, & Leghissa, 2002).

(b) Nakoya University YBCO single-phase transformer (Kotari, Kojima, Hayakawa, Endo, & Okubo, 2010).

Figure 2.12: Superconducting transformers.

2.1.5.3 Superconducting Magnetic Energy Storage (SMES)

Nowadays, energy storage is becoming more and more important. The use of superconductivity on it has shown many benefits. In the Superconducting Magnetic Energy Storage (SMES), the energy is stored in a magnetic field of a superconducting magnet connected to an AC/DC converter (figure 2.13). The magnet is charged and discharged to the AC power line by a superconducting switch (Malozemoff, 2012; Rogalla & Kes, 2011).

The benefit of this type of energy storage is the lower losses and higher efficiency when compared with the traditional ones because the energy is stored in the form of electricity in the superconducting magnet, which has low losses. For instance, although they do not have the same functions, the pumped hydro-energy have only 70 – 80% of efficiency, while SMES have at least 90% (Rogalla & Kes, 2011). The SMES can be applied to increase the grid power quality and stability when occurs voltage dips and sags and

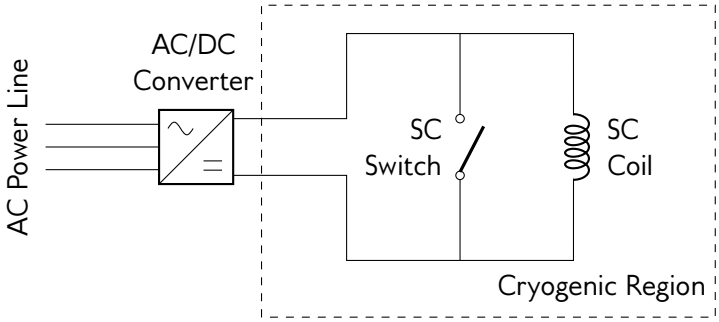

Figure 2.13: SMES equivalent schematic (Rogalla & Kes, 2011).

low-frequency oscillations. In this way, this type of energy storage can prevent blackouts (Malozemoff, 2012; Rogalla & Kes, 2011).

Currently, the SMES uses HTS wires, instead of LTS. In addition to the advantages already mentioned, the HTS wires flexibility allows more compact coils than the LTS ones. As result, as presented in figure 2.14, the HTS SMES can be more compact than the LTS SMES (Rogalla & Kes, 2011).

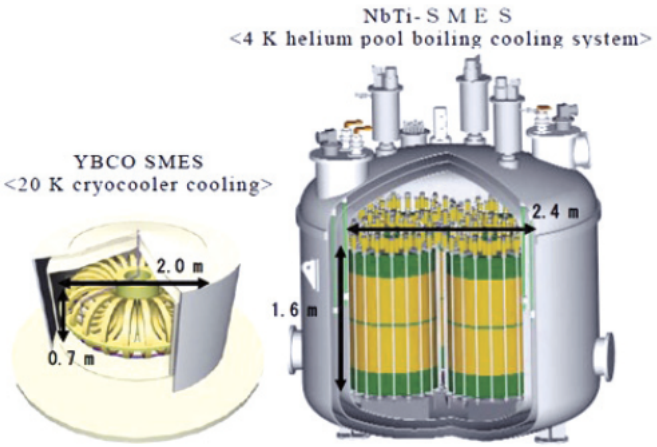

Figure 2.14: Comparison between a HTS and LTS SMES (Rogalla & Kes, 2011)

The first HTS SMES was developed by American Superconductor (AMSC) in 1997. Its capability is of 5 kJ using 1G HTS BSCCO conductors with an operating temperature of 4 K. More recently, due to the popularization of the 2G HTS YBCO tapes, the development of SMES is focused on its usage. In 2014, was developed in the University of Bath, England, a 2 kJ SMES using 1G HTS YBCO tapes at 77 K (Yuan & Zhang, 2015).

2.1.5.4 Transmission Cables

The HTS power cables can be employed to the AC and DC. The AC HTS power cables are divided in the following designs: warm and cold dielectric. The warm dielectric HTS cable (figure 2.15a) is based on a single conductor, with HTS wires stranded around a flexible core in a channel filled with LN_2. The cold dielectric HTS cable (figure 2.15b) has

two concentric HTS layers separated by a cold dielectric (Malozemoff, 2012; Rogalla & Kes, 2011).

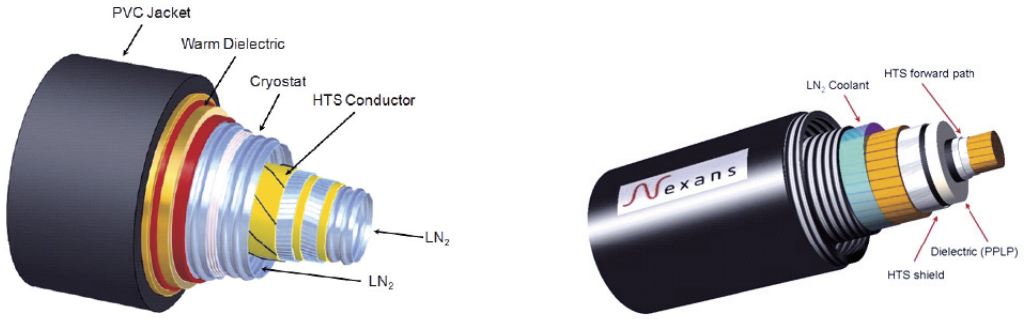

(a) Warm dielectric. (b) Cold dielectric.

Figure 2.15: Single-phase AC HTS cables (Rogalla & Kes, 2011)

The DC HTS power cables are applied in longer distances than the AC ones, due to superconductors zero resistance at DC operation (Rogalla & Kes, 2011; Seidel, 2015). The cooling substation of the DC cables can be more distant than the AC due to the smaller hysteresis and eddy current losses (Seidel, 2015). Furthermore, the DC HTS power cables are used also for high power transmissions and renewable energy as solar and wind ones. This type of HTS power cables uses two cryostat pipes: one for the power cable and other for the LN_2 return (figure 2.16) (Rogalla & Kes, 2011).

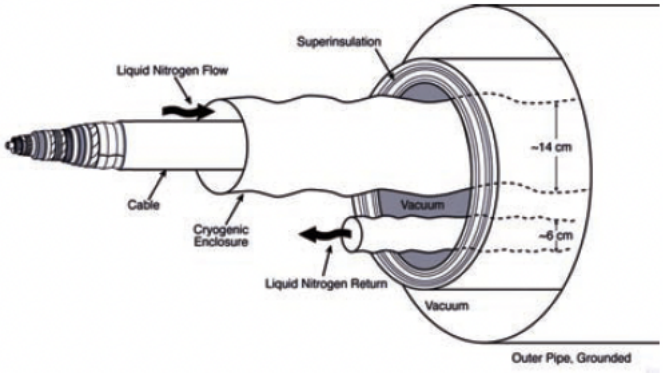

Figure 2.16: DC HTS cable (Rogalla & Kes, 2011).

The HTS power cables were applied several times in many experiments. One of them is in operation since 2008 in Long Island, USA, and consists of three HTS individual cables for three phases connected to the power grid. The cables were fabricated by Nexans and AMSC. Its length is 600 m long with transmission voltage of 138 kV and average current of 2400 A (Kleiner & Buckel, 2016).

Figure 2.17: Termination of the superconducting cables manufactured by Nexans and AMSC (Rogalla & Kes, 2011).

2.1.5.5 Fault Current Limiters (FCL)

The Fault Current Limiters (FCL) are devices used to limit the short-circuit currents when occurs a fault in the energy transmission. In high and low voltage, these devices have inductors and special switchgears to interrupt the fault current. These devices can be used in utility grids, industrial systems, and isolated power systems such as large ships (Rogalla & Kes, 2011).

The use of superconductors in the FCL has proved to be many benefits. The Superconducting Fault Current Limiters (SFCL) can be used in growing grid and power systems, in heavy load areas, in highly meshed systems, and in locations where new generator units have to be introduced (Rogalla & Kes, 2011). There are three SFCL types (Rogalla & Kes, 2011; Seidel, 2015): resistive, inductive and shielded-core.

The resistive SFCL are composed by superconducting wire, bulk or tape material (R_{sc}) in parallel with a conventional resistor (R_p) as presented in figure 2.18. A time vary fault current $i_{sc}(t)$ is driven through the superconductor with the capability to change from a superconducting to a resistive state when the current exceeds I_c, acting as normal resistance. The power grid is protected by the passive transition and current sharing with R_p. To restore the grid protection and protect the SFCL, the switch S_l must be opened after specific time (Rogalla & Kes, 2011).

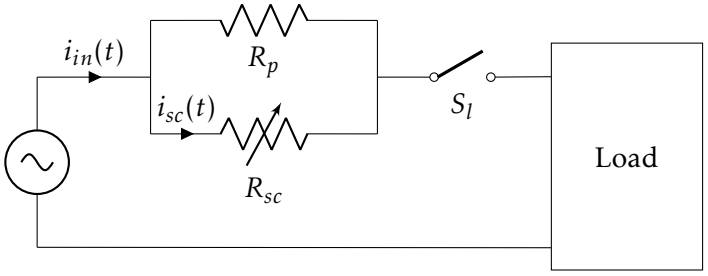

Figure 2.18: Schematic of a resistive SFCL (Rogalla & Kes, 2011).

In the inductive SFCL, the superconductor magnetically connected to the circuit to be protected, similarly to a transformer. Thus, the current is limited by a impedance caused by the high magnetic flux caused by the high current that penetrates the iron core (Malozemoff, 2012; Seidel, 2015). The inductive SFCL are further divided into shielded and saturable core (Rogalla & Kes, 2011).

The shielded-core SFCL (figure 2.19) are composed by a primary made of conventional conducting cooper coil and superconducting secondary coils wrapped around a iron core. In a normal operation, the flux induced in the iron core by the two coils is cancelled, due to the opposite currents between both and consequently the iron core is not considered in this circuit. When a current fault occurs, the superconducting current increases and may exceed I_c and so, the resistance of the superconductor increases, with a consequent decrease in its current. With that, the shielding effect of the superconductor is lost and the cooper impedance is determined by the iron core (Rogalla & Kes, 2011; Seidel, 2015).

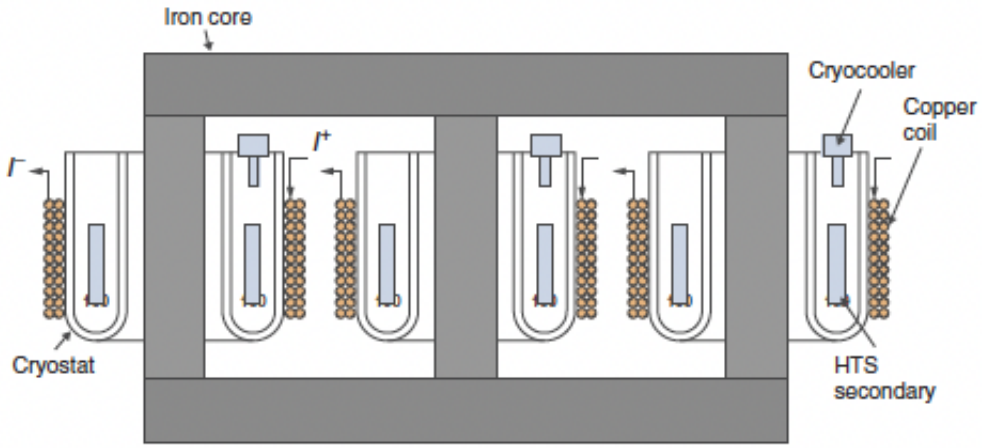

Figure 2.19: Shielded-core SFCL (Seidel, 2015).

The saturable-core SFCL (figure 2.20) are composed by two iron cores per phase AC conventional coils. In a normal operation, the DC superconducting coils drive the core into saturation and consequently reduce the impedance of the AC conventional coils. During a current fault, the current in the AC coils increases and the core goes out of saturation, increasing the impedance of the coil, limiting the fault current (Rogalla & Kes, 2011; Seidel, 2015).

There are many projects where the SFCL were applied. A resistive SFCL was developed by a Siemens/Nexans/AMSC collaboration (figure 2.21a). This SFCL limit faults on a single-phase, 60 Hz, 115 kV, 0.9 kA line with LN_2 as coolant (Malozemoff, 2012; Seidel, 2015). The Shigezhuang substation in China was built a 220 kV/300 MVA saturable-core SFCL by InnoPower (figure 2.21b) (Kleiner & Buckel, 2016; Seidel, 2015).

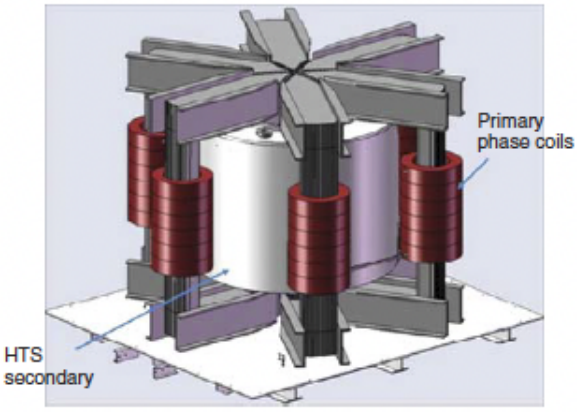

Figure 2.20: Saturable-core SFCL (Seidel, 2015).

(a) Siemens/Nexans/AMSC resistive SFCL.

(b) InnoPower saturable-core SFCL

Figure 2.21: SFCL projects (Seidel, 2015).

2.1.5.6 Electric Vehicles

The superconductivity can be applied to the electric vehicles, in the Magnetic levitation train (Maglev). This technology can be based on the perfect diamagnetism or in the flux pinning effect. The first one is no longer used due to its instability. Thus, nowadays the existing Maglev are based on the flux pinning effect with the diamagnetism provided by the type-II superconductors in the mixed state (described in section 2.1.3), which gives more stability (Han & Kim, 2016). There are two Maglev trains based on this principle: the SupraTrans and the Maglev-Cobra.

The SupraTrans (figure 2.22a) was developed in Germany by the Leibniz Institute for Solid State and Materials Research Dresden (IFW-Dresden) (Oliveira, Berger, Schultz, Stephan, & Ferreira, 2015). This system is composed of a permanent magnet guideway with a HTS block cooled inside a cryostat with LN_2. The lateral guidance is ensured by the superconducting pinning centers, while the levitation is done by the fields rejection

on the superconductor (Han & Kim, 2016).

The Maglev-Cobra project (figure 2.22b), has started in 2000, in the Federal University of Rio de Janeiro (UFRJ), in Brazil (Oliveira et al., 2015). The magnetic levitation is done by the interaction between HTS 2G YBCO and the magnetic field produced by the magnets.

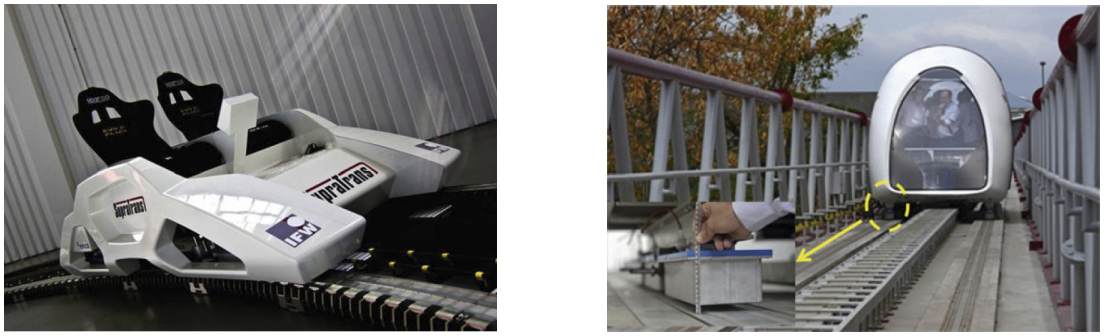

(a) Supratrans (b) Maglev-Cobra

Figure 2.22: Superconducting magnetic levitation trains (Han & Kim, 2016).

2.2 Cryogenic Cooling of the Superconductors

2.2.1 Introduction

The branch of physics that studies the methods to obtain and measure temperatures well below the room temperature, is called cryogenics (Ventura & Risegari, 2008). As already mentioned, in the section 2.1.1, the cryogenics and superconductivity history are related. The temperatures required by the superconducting materials can only be achieved through cryogenics.

Since the 19^{th} century, many gases were liquefied to reach absolute zero. Despite this evolution, absolute zero was never reached. As presented in figure 2.23, the lowest value of temperature reached was approximately 500 pK on a small number of atoms or molecules. Meanwhile, in nature, the lowest temperature is 2.7 K, corresponding to the deep space (Ventura & Risegari, 2008).

The practical superconducting applications described in section 2.1.5, must have cryogenic cooling systems associated, to maintain the operating temperature that allows the material to remain in its superconducting state with some margin. There are two cryogenic cooling methods: fluid cooling and cryocoolers. Both systems are dimensioned according to different parameters as (Seidel, 2015):

- Operating temperature;
- Heat load to be removed;
- Device design and dimensions;

- Coolant fluid.

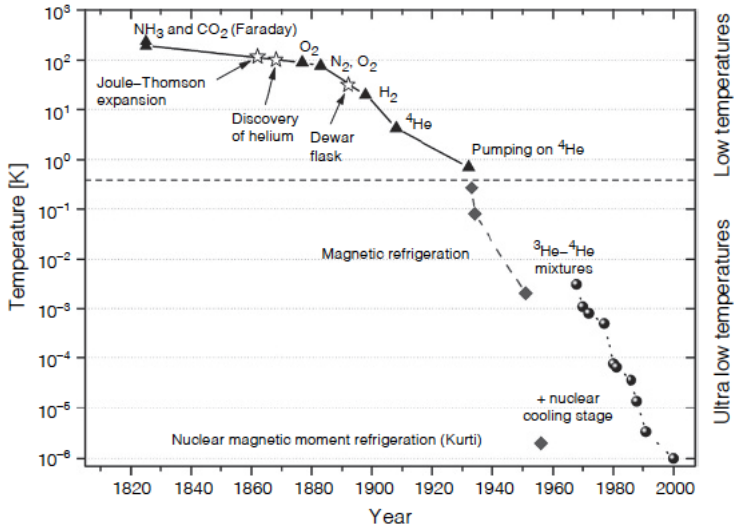

Figure 2.23: The evolution of the lowest temperature obtained by cryogenic methods (Ventura & Risegari, 2008).

2.2.2 Cryoliquids

The cryoliquids are coolants in the liquid state used to maintain the superconducting devices below the critical temperature (T_c). Three variables are important in the cryoliquids:

- **Boiling temperature at 1 atm of pressure** (T_b): must be inferior to the superconductor T_c in order to maintain the superconducting state;
- **Critical temperature**[1] (T_{cr}): maximum temperature where the cryoliquid can maintain the liquid state whatever the pressure. Above T_{cr}, the fluid no longer shows a dissipation between liquid and gas forms. It is called supercritical state. In such state, it is not adequate for cooling purposes.
- **Latent heat of evaporation** (L): energy necessary to evaporate an amount of the cryoliquid in the T_b.

In table 2.1, are represented the above described variables for the most used cryogenic fluids.

For LTS devices, the only cryoliquid suitable is the liquid helium (LHe), because NbTi and Nb_3Sn T_c is 9.2 and 18 K, respectively (figure 2.24) (Seidel, 2015). Maintaining the coolant near the boiling temperature of 4.2 K, the superconducting compound is always

[1] Do not confuse with the superconducting critical temperature (T_c)

Table 2.1: Characteristics of some cryogenic coolants at ambient pressure (Melhem, 2012; Seidel, 2015; Ventura & Risegari, 2008).

Coolant	T_b [°C]	L [kJ/kg]	T_{cr} [K]
Helium (He)	4.2	21	5.2
Hydrogen (H_2)	20.3	445	32.9
Neon (Ne)	27.1	86	44.4
Nitrogen (N_2)	77.3	199	126.3
Oxygen (O_2)	90.2	213	154.6

in the superconducting state. The LHe is inert, colorless, odourless, non-corrosive and non-flammable (Ventura & Risegari, 2008).

In the HTS devices the range of cryoliquids available is wider than the LTS: neon (Ne), hydrogen (H_2), oxygen (O_2) and nitrogen (N_2). The most used is the nitrogen in the liquid state (LN_2) in BSCCO and YBCO superconducting compounds with T_c of 93 and 105 K, respectively (figure 2.24). Nevertheless, for MgB_2 the hydrogen (H_2) is also suitable. The main advantages of the LN_2 are: low cost, no toxicity, good electrical insulation, performance and efficiency (Chen et al., 2012; Ventura & Risegari, 2008). Another important LN_2 advantage over the LHe is the L significantly higher, as presented in table 2.1. This means that, with the device heating, the LHe evaporates easier than the LN_2. Meanwhile, the displacement of oxygen in an enclosed volume is the main LN_2 disadvantage (Ventura & Risegari, 2008).

Taking advantage of its low cost, the LN_2 is used also to pre-cooling superconducting magnets to 80-100 K before LHe, because it is more economical than cooling directly from the room temperature to 4.2 K (Melhem, 2012).

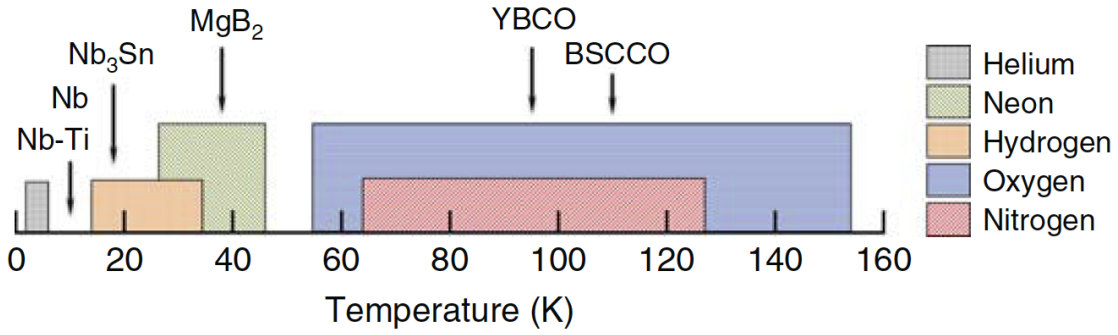

Figure 2.24: Cryoliquids operation range compared with T_c of the superconducting compounds (Seidel, 2015).

2.2.3 Cooling Methods

In the case of superconducting devices, there are three available cooling methods, i.e, ways to carry and circulate the cold produced, (Seidel, 2015): fluid mediated, conduction, and direct method (figure 2.25).

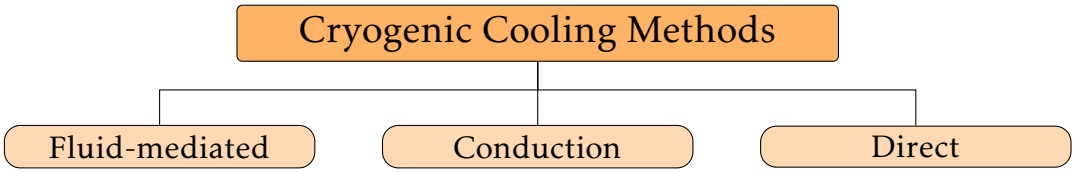

Figure 2.25: Cryogenic fluid cooling methods.

The fluid-mediated method consists of the transport of heat from a cold to a hot source intermediated by a fluid that circulates in a loop. The heat transfer is done by conduction and convection in the device and fluid loop, respectively. On the other hand, the conduction cooling method, as the name implies, is the heat removal by conduction in thermal links which are directly connected from the cold source to the device.

This dissertation will be focused on the direct cooling method that consists of the direct contact between the device and the coolant by channels integrated into the device. The heat transfer mechanism is mainly convection. Direct cooling can be done by bath and internal cooling.

In bath cooling, the superconducting device is immersed in a bath-cooled cryostat as presented in figure 2.26. The temperature of the coolant fluid is maintained by heat exchange (conduction and convection) or phase separation (evaporation and boiling). Nevertheless, during the operation, the bath needs to be refilled, due to the liquid losses by evaporation resulting from the device heat.

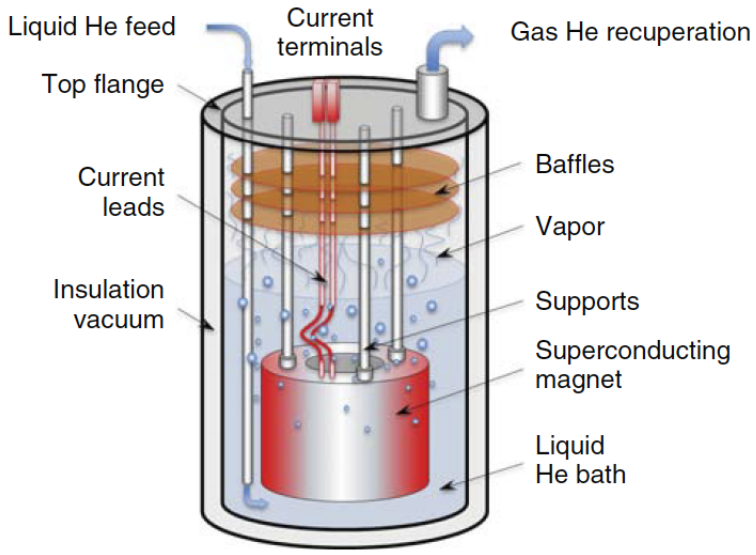

Figure 2.26: Superconducting magnet immersed in a bath-cooled cryostat (Seidel, 2015).

This method is indicated for small systems due to its simplicity and low cost. In addition, it can provide a high heat exchange in the submerged surfaces of the superconducting magnet. However, the bath cooling allows a low-temperature variation margin and has the limitation of not supporting high voltage devices. Finally, the high volume

of the cryostat increases the cost with coolant (Seidel, 2015).

In the internal cooling method, the device is cooled by a flow in internal channels and/or pipes that make part of the device. This devices can be seen as a loop represented in figure 2.27. The heat generated by refrigerator or storage reservoir ($\dot{q}_{ref}$) determines the mass flow $\dot{m}$ temperature. $\dot{m}$ is maintained by a pump or compressor, which generates the heat $\dot{q}_{circ}$, thus controlling the heat transfer. The main mechanism of heat exchange is convection.

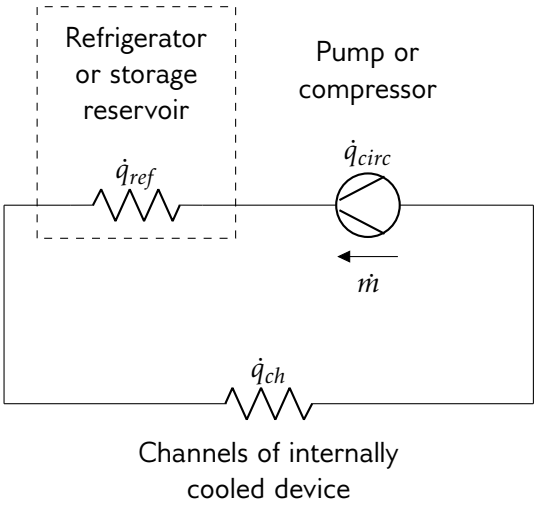

Figure 2.27: Internal cooling schematic. The mass flow is represented (Seidel, 2015).

A reduced coolant volume, relative to the bath cooling and compatibility with high-voltage devices are advantages of direct cooling. But, this method has the drawback of complexity because of the need for compressors and circuits to guarantee the flow of the coolant (Seidel, 2015).

In short, the bath cooling, despite being a simple implementation presents non-autonomy and a high cost of operation due to the coolant refills. Meanwhile, direct cooling is a more efficient and controlled method than the bath one, with the drawback of the need for a complex circulating system with a pump to maintain the flow.

2.2.4 Cryocoolers

Both cooling systems described in the previous section need to be refilled regularly with coolant, due to its evaporation caused by the device heat. This may become an obstacle for superconducting systems located in remote areas, for example. To overcome that, the more appropriate solution is the use of cryocoolers, powered by electricity.

Cryocoolers are refrigerators created to reach cryogenic temperatures. This solution has some advantages over cryoliquid cooling, such as higher efficiency, long lifetime, small size, and low price. Nevertheless, the vibrations, electromagnetic interferences, and temperature variations are disadvantages of this device (Seidel, 2015).

Two types of cryocoolers are commonly used today: Stirling (for high frequencies) and Gifford-McMahon (GM) (for lower frequencies) (Seidel, 2015). The design principle of both is depicted in figure 2.28. The heat is pumped from the cold to hot heat exchanger by the displacer in the compression and expansion of the cold space.

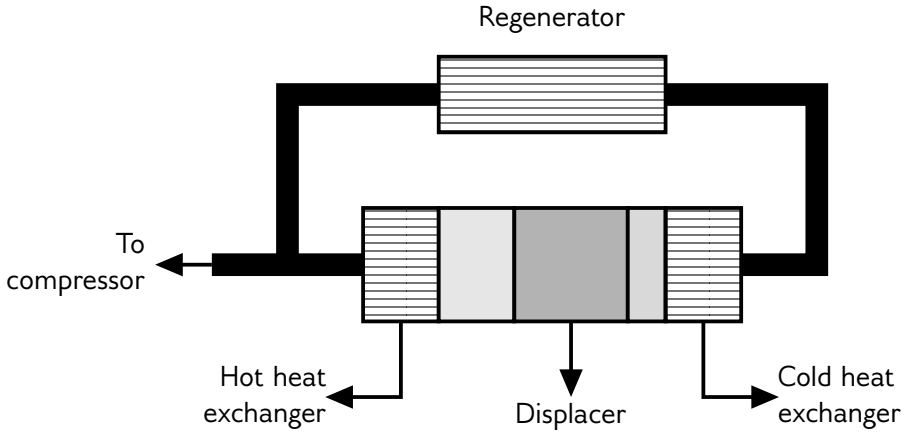

Figure 2.28: Design principle of Stirling and Gifford-McMahon cryocoolers (Seidel, 2015)

The Stirling cryocooler is composed of a pressure wave generation and a cold head equipped with a displacer, which increases the hot space during compression and the cold space during expansion. When these two ones are connected directly, the cryocooler is called integral. When not, it is referred to as a split cryocooler. The operation frequency of the Stirling cryocoolers is between 30 and 100 Hz, often coinciding with the electric line (50 or 60 Hz) (Seidel, 2015).

The GM cryocoolers operate at lower frequencies than the Stirling ones (between 1 and 5 Hz) and are always split cryocoolers. The composition of GM cryocoolers is made of a compressor package and cold head package (Seidel, 2015).

2.3 Superconducting Machines

2.3.1 Introduction

The first applications of superconductors to electrical machines date back to the 1960s. At the time, the material used was the multi-filamentary NbTi LTS. Its superconductors just could carry DC current. So, its first application was in the rotating machines DC field windings. Many typologies of LTS machines were developed during the following years by General Electric, Westinghouse, and Super-GM according to table 2.2. Nevertheless, the LTS were not economically practicable because of the high cost, instability, and unreliability of the cooling systems at 4.2 K (Haran et al., 2017). Another issue was the protection of NbTi from harmonics fields generated by the stator and the complications and costs of the stator windings (Haran et al., 2017).

Table 2.2: Some LTS machines concepts (Haran et al., 2017).

Year	**Power** [kW]	**Conductor type**	**Application**	**Developer**
1978	20000	NbTi	Utility	General Electric
1978	300000	NbTi	Utility	Westinghouse
1978	1200000	NbTi	Utility	Westinghouse
1980	20000	NbTi and Nb_3Sn	Air force	General Electric
1982	25000	NbTi	Utility	General Electric
1983	2250	NbTi	Navy	General Electric
1987	18	NbTi	Demo	General Electric
1997	78700	NbTi	Utility	Super-GM
2005	37000	NbTi	Navy	General Atomics

In 1986, with the discovery of the HTS compounds, the superconducting machines have become more viable to implement as presented in table 2.3 and described along the present section. The HTS conductors can operate in much higher temperatures than LTS. So, the cryogenic cooling systems are more stable due to the wider operating temperature range than the LTS conductors. Furthermore, due to the higher thermal heat capacity of the HTS, these compounds can absorb more heat with less temperature variation (Haran et al., 2017).

Table 2.3: Some HTS machines concepts (Haran et al., 2017).

Year	**Power** [kW]	**Conductor type**	**Application**	**Developer**
2001	3725	BSCCO	Industrial	AMSC
2001	400	BSCCO	Demo	Siemens
2003	1500	BSCCO	Utility	General Electric
2004	4000	BSCCO	Generator	Siemens
2004	5000	BSCCO	Marine	AMSC
2005	8000	BSCCO	Utility	AMSC
2006	36500	BSCCO	Marine	AMSC
2008	1300	BSCCO	Aerospace	General Electric
2009	7.5	YBCO	Marine	NEDO
2009	160	BSCCO	Marine	FAMU, Georgia Tech, NASA
2010	4000	BSCCO	Marine	Siemens
2010	1000	BSCCO	Marine	KHI
2011	1000	BSCCO	Marine	Wuhan Institute
2011	5000	BSCCO	Marine	Doosan
2012	17000	BSCCO	Hydro	General Electric
2012	3000	BSCCO	Marine	KHI
2013	400	BSCCO	Marine	IHI
2017	10000	MgB_2	Wind farm	European Commission

Aiming at its low-cost, high efficiency, and reliability, the HTS machines can be applied in (Haran et al., 2017):

- Electric utility/power industry;
- Wind farm generators;
- Aerospace motors and generators;
- Marine applications;
- Industrial applications.

In 2006, AMSC tested and shipped to US Navy the 36.5 MW HTS ship propulsion motor (figure 2.29). The motor weight is about 75 t, which represents more than 50% weight reduction when compared to a conventional motor with the same power capability (200 t). The excitation windings of rotor are made of 1G HTS BSCCO tape (Gieras, 2009).

Figure 2.29: 36.5 MW synchronous motor manufactured by AMSC (Gieras, 2009).

Between 2012 and 2017, a 10 MW superconducting wind turbine was developed by the Superconducting, Reliable, lightweight, and more powerful offshore wind turbine (SUPRAPOWER) research project from European Commission (figure 2.30). In this solution, the weight of the generator can be reduced by about 30% compared to the conventional ones. The rotor and stator windings are made of MgB_2 and cooper wires, respectively. These first ones are also packaged in a cryostat in a vacuum environment (Sun, Sanz, & Neumann, 2015).

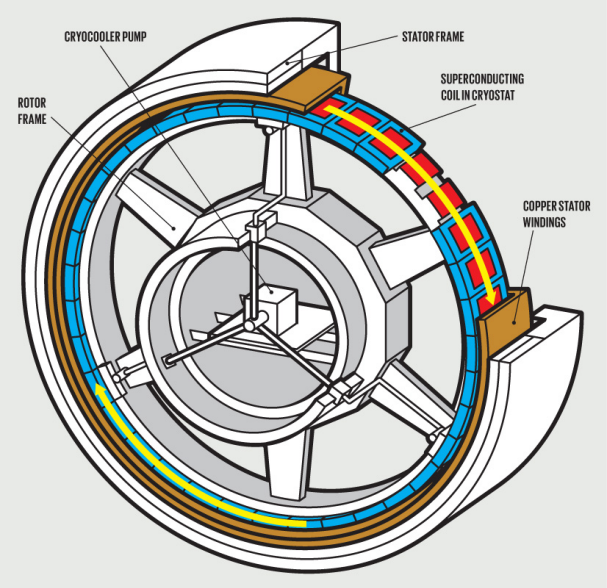

Figure 2.30: 10 MW SUPRAPOWER wind turbine (Moore, 2018).

In 2021, Airbus launched the Advanced Superconducting & Cryogenic Experimental Powertrain Demonstrator (ASCEND) project. This consists in a 500 kW electric or hybrid-electric propulsion system complemented with cryogenic and superconducting technologies (figure 2.31) (Airbus, 2021). This system can be 2 to 3 times lighter than a conventional one due to the reduction in the cable weight and power electronics limit of 30 kW/kg. Furthermore, the volume, complexity, and power losses of this system are less than the conventional systems (Duvelleroy, 2021).

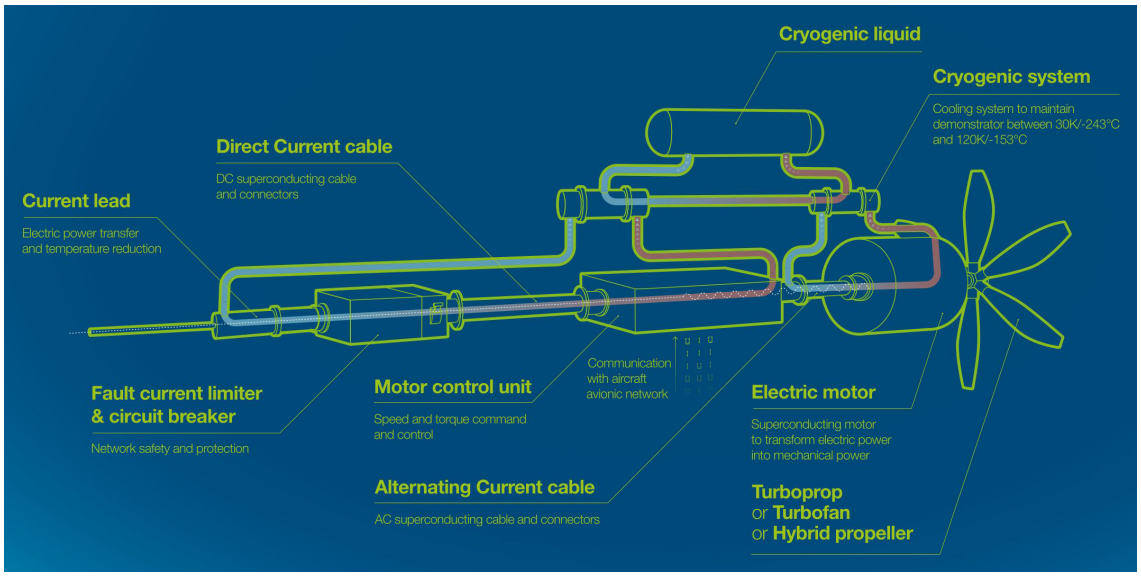

Figure 2.31: ASCEND system components (Airbus, 2021).

The superconducting machines can be classified regarding the superconductivity, input voltage, and flux direction as depicted in figure 2.32. In the next sections, each classification is detailed.

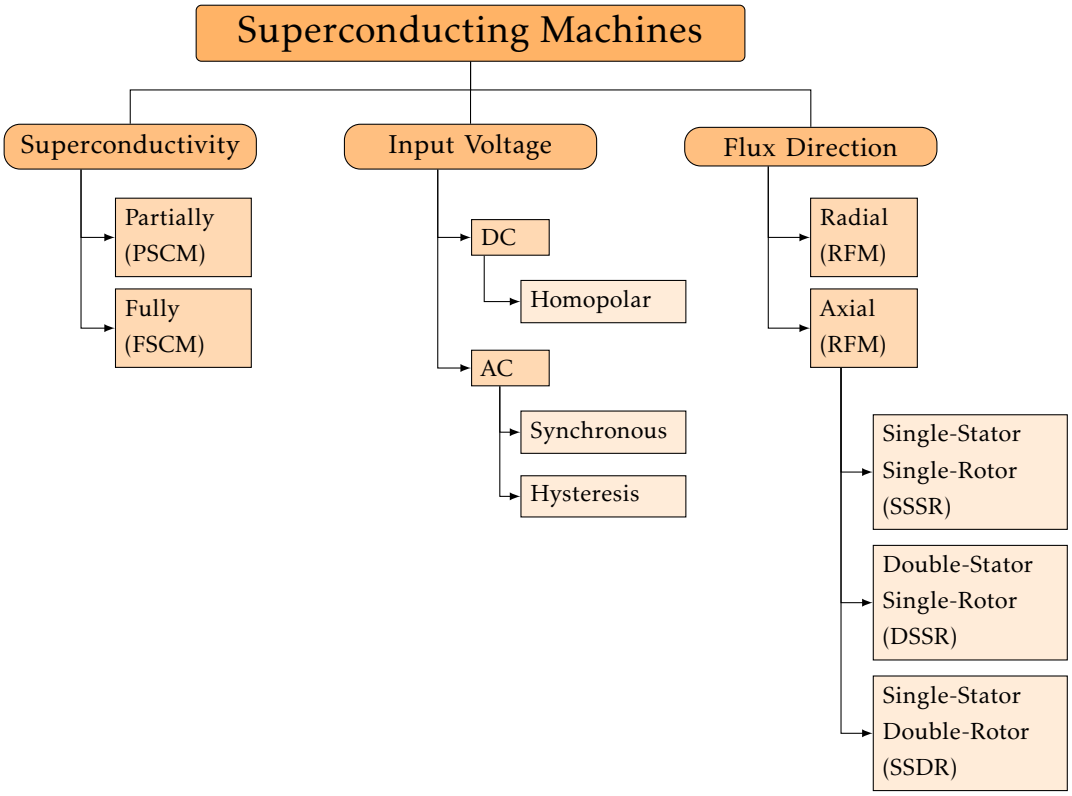

Figure 2.32: Superconducting machines classification.

2.3.2 Fully Superconducting Machines (FSCM) and Partially Superconducting Machines (PSCM)

Regarding the superconductivity, the superconducting machines are divided into two types: Fully Superconducting Machines (FSCM) and Partially Superconducting Machines (PSCM) (figure 2.33) (Haran et al., 2017; Sayed et al., 2021). In the FSCM, both stator and rotor windings are made of superconducting wires, while in the PSCM, only the rotor or stator windings are made of this compound.

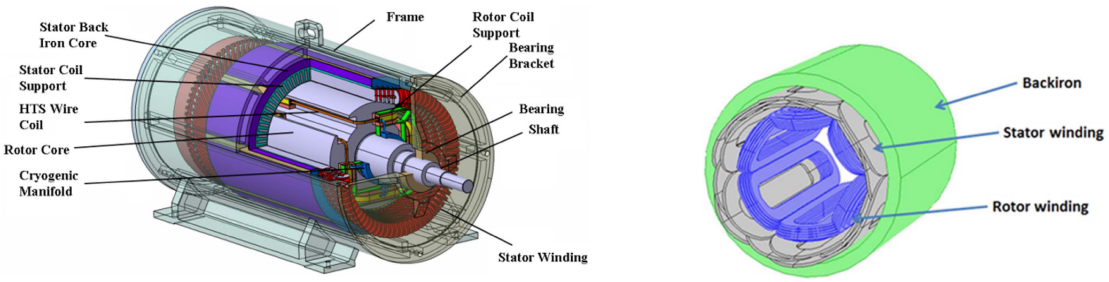

(a) PSCM (b) FSCM

Figure 2.33: HTS machines types regarding its superconductivity (Haran et al., 2017).

The FSCM are more efficient than the PSCM due to the higher superconducting employment and larger airgap. To get an idea, the FSCM power density is about 16 kW/kg, while in the PSCM this value is 7 kW/kg (Sayed et al., 2021). In the PSCM, the AC losses

are concentrated in the conventional stator windings. Nevertheless, the PSCM are projected to reach an efficiency of about 99%. So, to the FSCM be competitive, relatively to the PSCM, the AC flux must be about 10×10^3 T/s (Haran et al., 2017). On both types, the rotor windings are made of BSCCO or YBCO HTS wires. However, in order to reduce the AC losses, the PSCM stator windings are made of MgB_2 conductors with multifilament structure (Sayed et al., 2021; Terao, Kong, Ohsaki, Oyori, & Morioka, 2018).

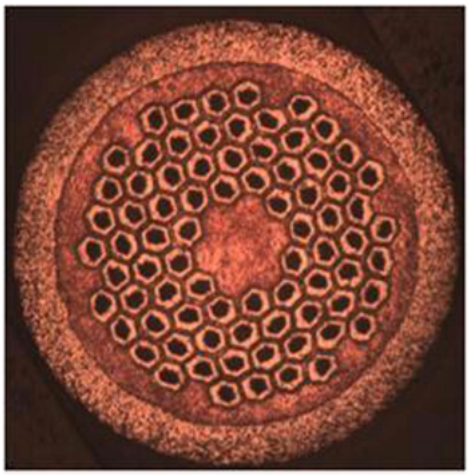

Figure 2.34: MgB_2 wire of the FSCM stator windings. The black circles represents the MgB_2 compounds (Haran et al., 2017).

2.3.3 Input Voltage

Regarding the input voltage, the superconducting machines are divided into DC and AC. The most part of the superconducting machines are AC, due to the typical drawbacks of the DC machines as the the cost of manufacturing and maintenance of the current collector and brushes (Gieras, 2009; Haran et al., 2017). Nevertheless, General Atomics developed an HTS DC homopolar motor presented in the figure 2.35. This solution, despite the drawbacks, is more efficient, simple, smaller and lighter than the AC counterpart (Gieras, 2008).

Typically, there are two types of AC superconducting machines: synchronous and induction. In synchronous machines, the rotor and traveling stator magnetic field have the same speed. Generally, this machines have AC and DC windings in the stator and rotor, respectively. This means that the rotor field excitation winding is made by superconducting wires. Meanwhile, in the stator, these machines, can be excited by cooper coils or permanent magnets (Gieras, 2009). Regarding the rotor construction, there are two types of synchronous machines: coreless and ferromagnetic (Gieras, 2009).

The superconducting synchronous machines with coreless rotor consists of an air-core rotor (figure 2.36). The torque of this machine is produced directly on the superconducting winding and transmitted through a low thermal-conductivity torque tube until the room temperature shaft.

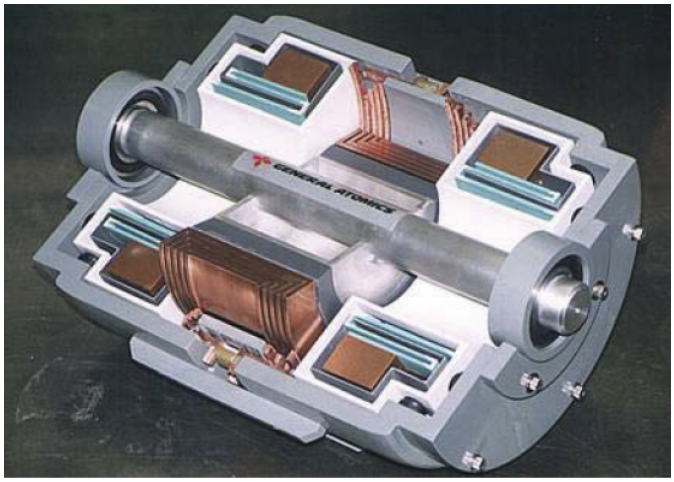

Figure 2.35: Longitudinal section of the General Atomics HTS DC homopolar motor (Gieras, 2008).

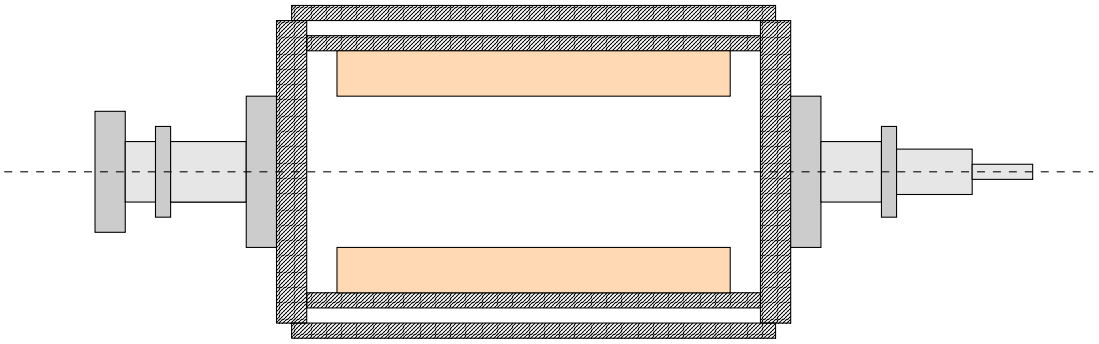

Figure 2.36: Superconducting coreless synchronous machine. The HTS coils are represented by orange (Gieras, 2009)

In the superconducting synchronous machines with a ferromagnetic core rotor, the torque is applied in a salient pole rotor, at ambient temperature, made of steel or another ferromagnetic (figure 2.37). The HTS coils are mounted in series and have pancake shape (figure 2.38).

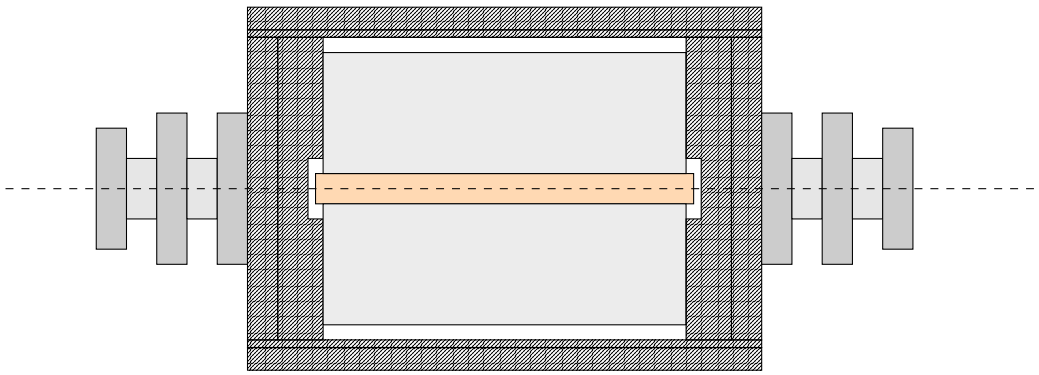

Figure 2.37: Superconducting ferromagnetic synchronous machine. The HTS coils are represented by orange (Gieras, 2009)

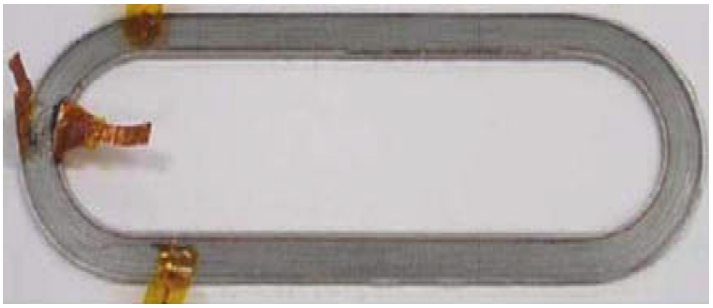

Figure 2.38: HTS rotor excitation winding (Gieras, 2009)

The difference between the magnetic permeability of the air and rotor compound leads to a reduction of the necessary magnetomotive force. Thus, this configuration results in less superconductor amount than the coreless configuration. Furthermore, the existence of a ferromagnetic core limits the airgap magnetic flux density in about 2 T, which is lower than the airgap rotor configuration. Despite that, the obtained torque density is slightly lower than the air core configuration. So, this configuration needs smaller coils and simpler mechanical support. Thus, it is more suitable for high-speed machines (Gieras, 2009).

In the hysteresis machines, the hysteresis phenomenon is exploited in order to generate torque. Regarding the conventional hysteresis machines, the rotor of this machine is a simple and solid cylinder of ferromagnetic material without windings, teethes, and protrusions (Chapman, 1991). Meanwhile, in the superconducting hysteresis machines, the rotor is made of type-II superconducting compound which have, as mentioned in section 2.1.3, the capability of flux pinning through the mixed state (Barnes, Mcculloch, & Dew-Hughes, 2000).

The torque-speed curve of the hysteresis machine is represented in figure 2.39. The machine starts with torque τ_{m0} and the stator traveling field magnetic field magnetizes the superconducting rotor and induces poles within it. However, the induced poles are lagging because the rotor hysteresis losses of the rotor are greater than the stator hysteresis losses. The higher the rotor material hysteresis cycle, the higher the angle between the rotor and stator magnetic field is (Chapman, 1991). So, during the machine operation, the magnetic fields tend to be aligned by the hysteresis torque (τ_h) calculated through the following expression (Pina, 2010b):

$$\tau_h = \frac{k_h \cdot (B_{max})^n}{2 \cdot \pi \cdot N_s} \tag{2.9}$$

where N_s is the synchronous speed, B_{max} is the rotor maximum flux density and n is the hysteresis power constant that depends on the rotor material. When the rotor and stator fields are aligned, the motor reaches N_s and the rotor acts as a permanent magnet.

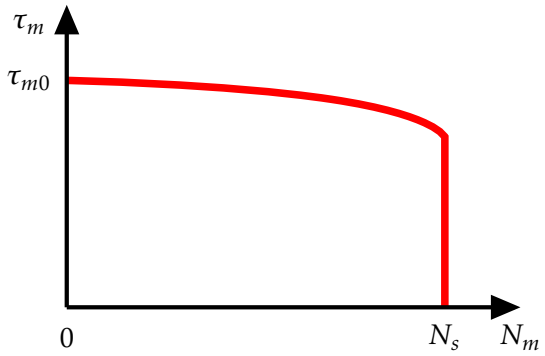

Figure 2.39: Torque-speed characteristic of an hysteresis motor (Chapman, 1991).

2.3.4 Flux direction

Regarding the flux direction, the superconducting machines are divided into Radial Flux Machines (RFM) and Axial Flux Machines (AFM). The RFM is the most popular construction for electrical machines, in general. That is constituted by a cylindrical stator surrounded by a single stator (figure 2.40a). Meanwhile, in the AFM, the airgap flux takes axial direction and the conductors have a radial position (figure 2.40b). Typically, the AFM have a pancake shape with thinner stators and disc rotors. This kind of construction can acquire a very compact form and the airgap can be adjustable (Gieras, Wang, & Kamper, 2008).

In the particular case of superconducting machines, due to the flatness of the AFM construction, the inserting of superconducting tapes is easier than the RFM. This makes the AFM an attractive construction for superconducting machines (González-Parada, Guía, Ibarra, & Guzmán, 2012).

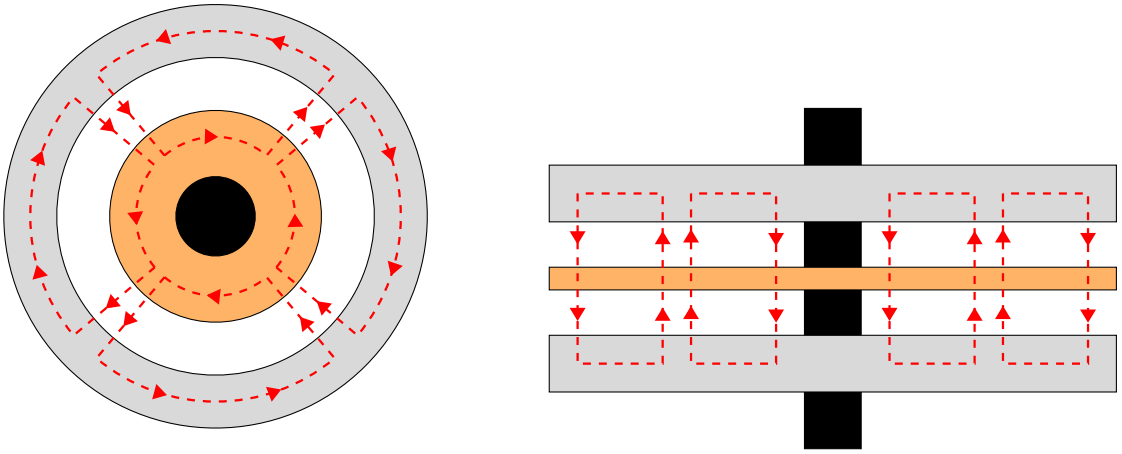

(a) RFM (b) AFM

Figure 2.40: The two typologies of four pole PSCM, regarding the flux direction. The core stator are represented by grey, the superconducting rotor by orange and the shaft by black. The red arrows represent the flux lines. The windings are hided from this representation This figures are not to scale.

The AFM are divided further into three configurations: Single-Stator Single-Rotor (SSSR), Double-Stator Single-Rotor (DSSR) and Single-Stator Double-Rotor (SSDR) (Chan, 1987; Husain, Tekgun, Sozer, & Hamdan, 2017).

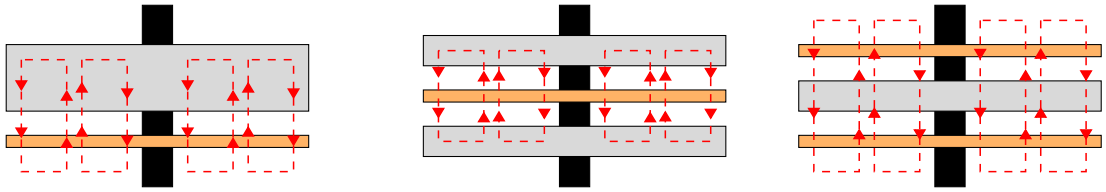

(a) SSSR (b) DSSR (c) SSDR

Figure 2.41: AFM types on four pole PSCM. The core stator, superconducting rotor and shaft are represented by gray, orange and black, respectively. The red lines represent the flux lines. The windings are hidden from this representation. This figures are not to scale (Husain, Tekgun, Sozer, & Hamdan, 2017).

The AFM SSSR is constituted by a unique rotor and stator (figure 2.41a), resulting on simple and easy to manufacture structure. Although, the imbalanced axial forces are an important issue (Husain et al., 2017).

The AFM DSSR (also called Axial Flux Interior Rotor (AFIR)), is constituted by two semi-stators and between them a disc stator (figure 2.41b). In contrast to the AFM SSSR, the axial forces are balanced and the rotor is more protected against mechanical impact, wear, or corrosion due to two semi-stator. This construction presents also, a high torque density and more fault-tolerant characteristics. Nevertheless, the drawbacks of the AFM DSSR, is the higher linkage flux and armature reaction and hence the high cooper losses (Husain et al., 2017).

The AFM SSDR is constituted by a single stator between two rotors (figure 2.41c). The main advantage is the lower cooper losses (Husain et al., 2017).

Regarding AFM advantages over RFM, the first one is the rectangular and more regular path for the flux not affected by the rotor teethes (Chan, 1987). Furthermore, because of its more compact structure, the AFM has a higher power density than the RFM. Another important issue is the better ventilation and cooling on the RFM. This happens because the size of the core relative to the area occupied by the shaft is much greater. Due to this fact, this type of machine is a solution when a higher number of poles are wanted. With that, the AFM is a valid solution for high frequencies or low-speed operations (Gieras et al., 2008).

2.3.5 Cryogenic systems

As with any superconducting device, the superconducting electrical machines needs cryogenic cooling systems, to assure its correct operation, maintaining the operating temperature below the critical one ($T < T_c$). Generally, the cooling systems used are the bath cooling or cryocoolers (Masson, Soban, Upton, Pienkos, & Luongo, 2005). As already described, bath cooling has the drawback of the coolant refill due to the evaporation

caused by the machine heat. The systems with cryocoolers have the layout of the figure 2.42. The machine is connected by channels to a dewar recipient with coolant which is refrigerated by a cryocooler.

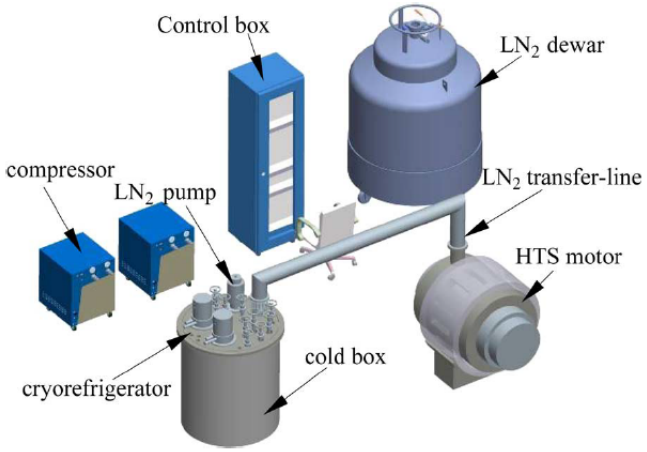

Figure 2.42: Layout of the HTS machine cooling system (Chen et al., 2012).

In the superconducting electrical machines, the rotor windings are composed of HTS compound and rotate with the machine operation. This is a problem in that there is a need to transfer cryogenic coolant from a stationary cryocooler to a rotating component (Melhem, 2012). This problem is solved by recurring to a rotating coupling with two concentric tubes rotating inside the other.

The machine cooling is not uniform, i.e, different parts of the machine can cool down at different rates. With that, the machine constituent materials experience non-uniform stresses between welded and bolted components. A solution is the use of flexible connections such as braids, bellows, and disc springs (Melhem, 2012).

2.4 Losses in Electrical Machines

2.4.1 Introduction

Whatever the type of electrical machine, the study of the losses is a very important topic. When a machine is projected, the goal is always to minimize the losses. More losses mean less efficiency and power output, and consequently more operation costs. It is important to mention that in rotary machines, the efficiency is high, except for high loads (Fitzgerald, Kingsley Jr., & Umans, 2003).

Typically, the efficiency (η) is represented by:

$$\eta = \frac{P_{out}}{P_{in}} \tag{2.10}$$

where the power input and output. is P_{in} and P_{out}, respectively.

On electrical machines the losses can be: electromagnetic (P_{em}), thermal (P_{th}) and mechanical (P_{mec})(figure 2.43). This last one will not be the focus of this dissertation.

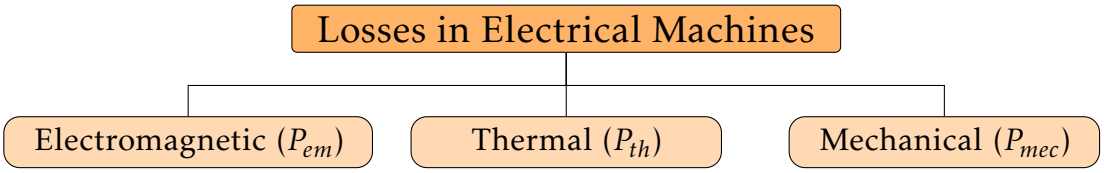

Figure 2.43: Losses in electrical machines.

2.4.2 Electromagnetic losses

The electromagnetic losses (P_{em}) are divided in ohmic (P_{oh}) and core (P_{cr}) losses as represented in the figure 2.44. This last one is further divided in eddy current (P_{ed}) and hysteresis (P_h) losses. On electrical machines, the ohmic and core losses are concentrated in the windings and machine ferromagnetic core, respectively (Fitzgerald et al., 2003).

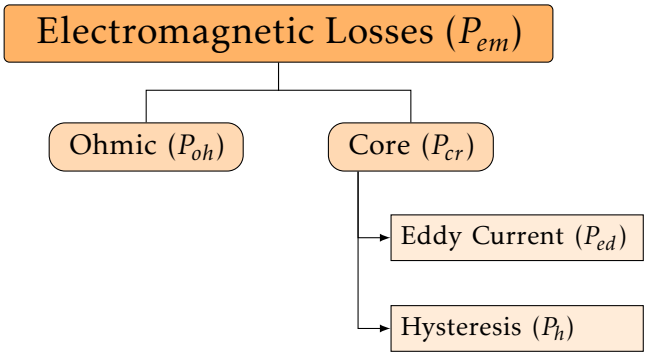

Figure 2.44: Electromagnetic losses.

Considering the ohmic conductor wire of the 2.45, P_{oh} is given by:

$$P_{oh} = I^2 \cdot R_w \tag{2.11}$$

where I and R_w are the wire current and resistance, respectively. R_w can be obtained by the the 2nd Ohm's Law:

$$R_w = \rho(T) \cdot \frac{l_w}{A_w} \tag{2.12}$$

where the conductor cross area and length is A_w and l_w, respectively. ρ is the conductor resistivity that is a temperature (T) dependent function given by the approximated expression:

$$\rho(T) = \rho_0 \cdot [1 + \alpha \cdot (T - T_0)] \tag{2.13}$$

where α is the thermo-resistivity coefficient, T_0 is the initial temperature and ρ_0 is the resistivity at that temperature. It is important to refer that ρ is proportional to α and T. Thus, with an increase of the temperature, the wire resistance will be higher and also the resulting losses (Gieras et al., 2008).

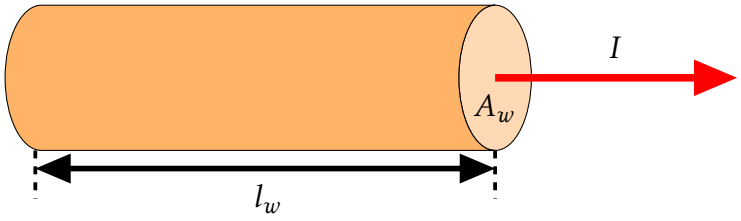

Figure 2.45: Ohmic conductor with length l_w, cross area A_w and current I

The eddy current (also called Foucault) losses (P_{ed}) are due to the induced electromotive force caused by the variation of the magnetic flux on the core. This causes the formation of closed-loop currents that causes ohmic power losses (figure 2.46a). This phenomenon can be minimized by the implementation of a laminated core instead of a solid one. Each core plate is isolated physically and electrically from the others by coating (figure 2.46b) (Fitzgerald et al., 2003; Gieras, 2017).

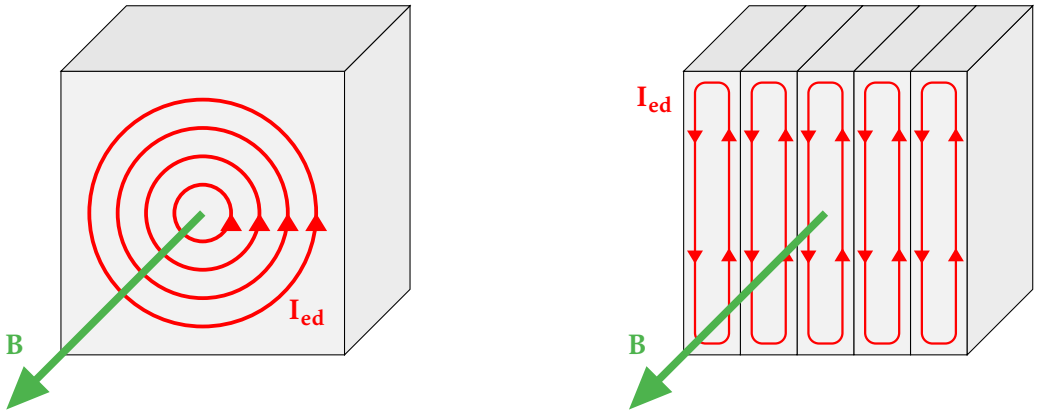

(a) Solid core.

(b) Core laminated in five plates.

Figure 2.46: Cross section of a ferromagnetic core showing the eddy current effect. The magnetic flux density vector (**B**) is represented by green and the eddy current vector ($\mathbf{I_{ed}}$) by red. This figure are not to scale (Gieras, 2017).

The ratio between the thickness of the core and insulator and with the insulator is given by the stacking factor (k_i):

$$k_i = \frac{\lambda_c}{\lambda_c + 2\lambda_i} \tag{2.14}$$

where, λ_c and λ_i are the laminated core and coating thickness, respectively.

P_{ed} depends on the maximum flux density (B_{max}), the operation frequency (f) and the plate thickness (λ_c):

$$P_{ed} = k_{ed} \cdot (B_{max} \cdot f \cdot \lambda_c)^2 \tag{2.15}$$

where k_{ed} is a proportionality constant that depends on the core mass and resistivity (Fitzgerald et al., 2003; Gieras, 2017).

The hysteresis losses (P_h) are related to the magnetization of the ferromagnetic core. When a material is magnetized for the first time, by a magnetic field H, its flux density grows from 0 to the saturation value (B_{sat}) (figure 2.47).

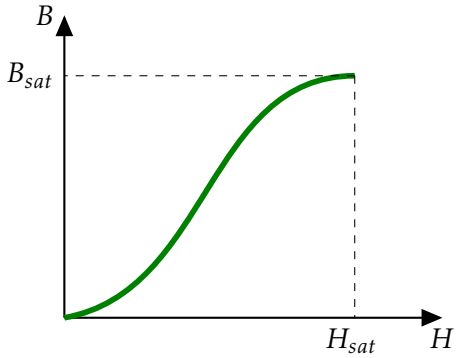

Figure 2.47: Example of magnetization curve for the first magnetization. This figure are not to scale.

After the first magnetization, when the material is demagnetized, there always remains a flux density (B_r). This magnetization loop is called the hysteresis loop (figure 2.48).

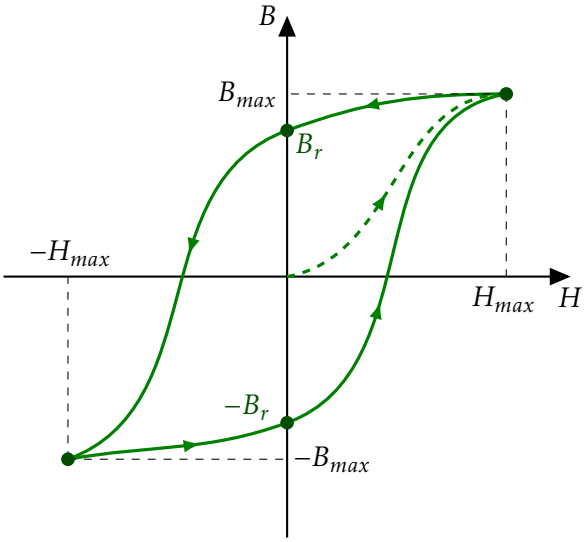

Figure 2.48: Hysteresis loop of any material. The curve of the first magnetization are represented by a dashed line. This figure are not to scale. (Gieras, 2017)

P_h is the energy lost due to the hysteresis effect when the core is magnetized. These losses are proportional to the area of the hysteresis loop and depend on the maximum flux density (B_{max}) and operation frequency (f) (Steinmetz, 1984):

$$P_h = k_h \cdot f \cdot (B_{max})^n \tag{2.16}$$

where the k_h and n depends on the core material (Gieras, 2017).

2.4.3 Thermal Losses

The study of the thermal losses (P_{th}) of the electrical machines is a very important topic. The dissipation of heat is due to electromagnetic and mechanical losses. This

causes the rise of the temperature of the motor and hence, the wear of the material and the reduction of the machine's operational life and efficiency (Gieras et al., 2008).

In the AFM particular case, the study of the thermal losses was not very extensive when compared to the other machines. These machines have a better ventilation capacity because of their larger airgap when compared to the conventional machines (Gieras et al., 2008).

According to the 2nd Law of Thermodynamics, the heat transfer is carried out from the high-temperature region (with temperature T_{hot}) to the low-temperature region (with temperature T_{cold}) to achieve thermal equilibrium. Considering that the electrical machines during their working reach greater temperatures than the surrounding environment, the heat transfer is always from them. So, the heat transfer can be done by three modes: conduction, radiation, and convection (figure 2.49) (Çengel, Boles, & Kanoğlu, 2019; Gieras et al., 2008; Moran, Shapiro, Boettner, & Bailey, 2014).

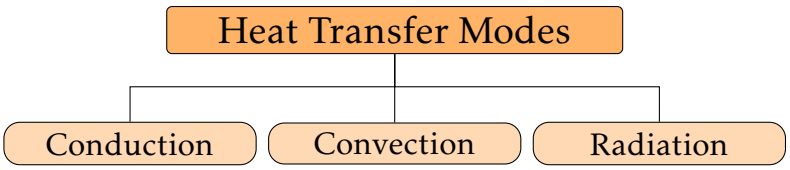

Figure 2.49: Heat transfer modes.

In the conduction process, the heat transfer are done from the more energetic particles, with temperature T_{hot}, to the adjacent less energetic particles, with temperature T_{cold} as presented in figure 2.50. This can happen in solids, liquids, or gases (Çengel et al., 2019; Moran et al., 2014).

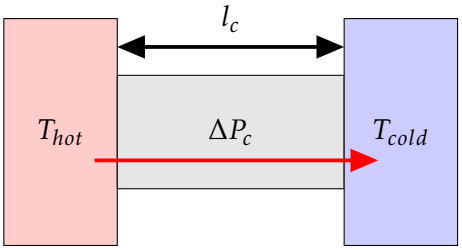

Figure 2.50: Conduction process between two surfaces with different temperatures separated by a medium with length l_c.

The rate of heat transfer by conduction (ΔP_c) is determined by the Fourier's Law (Çengel et al., 2019; Gieras et al., 2008; Moran et al., 2014):

$$\Delta P_c = -\frac{k_c \cdot A_c}{l_c} \cdot \Delta T = \frac{k_c \cdot A_c}{l_c} \cdot (T_{hot} - T_{cold}) \tag{2.17}$$

where k_c is the thermal conductivity coefficient, A_c the area normal to the direction of conduction flow path and l_c the length of the conduction path.

The convection process is the heat transfer between a solid surface at temperature T_{hot} and an adjacent motion fluid or gas at temperature T_{cold} that combines the conduction and fluid motion effects (Çengel et al., 2019; Gieras et al., 2008; Moran et al., 2014). Considering cool air over a hot surface, the heat between these two means is transferred by conduction (figure 2.51). After, this heat is carried away from the surface due to the combined effects of conduction and bulk motion of the fluid or gas (Çengel et al., 2019; Moran et al., 2014).

The rate of heat transfer by convection (ΔP_v) from a hot surface with top area of A_{hot} (2.51) is determined by the Newton's law of cooling (Çengel et al., 2019; Gieras et al., 2008; Moran et al., 2014):

$$\Delta P_v = k_v \cdot A_{hot} \cdot (T_{hot} - T_{cold}) \tag{2.18}$$

where k_v is the convection coefficient experimentally determined regarding variables such as: surface finishing and orientation, fluid properties, velocity and temperature. This coefficient is also directly proportional with the velocity of the cooling medium relative to the cooled surface (Gieras et al., 2008).

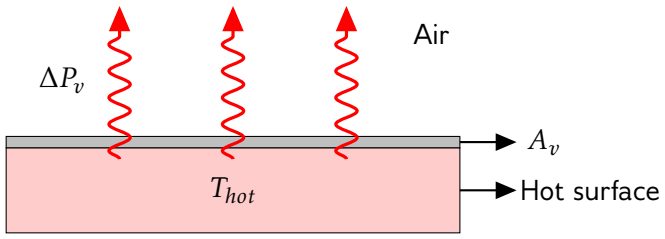

Figure 2.51: Convection process between a solid hot surface (at gray) with area of A_{hot} and cooled air. The red arrows represents the heat flow.

The radiation process is the heat transfer between the matters by electromagnetic waves as a result of changes in the electronic configurations in the atoms or molecules. This process occurs at the speed of light and does not have any attenuation in a vacuum (Çengel et al., 2019; Moran et al., 2014). The thermal radiation does not need an intermediate medium for its propagation, so can even occur in a vacuum.

The rate of heat transfer by radiation (ΔP_r) by a surface with temperature T is given by Stefan-Boltzmann law:

$$\Delta P_r = e \cdot k_{sb} \cdot T^4 \tag{2.19}$$

where k_{sb} is the Stefan-Boltzmann constant (5.67×10^{-8} W/m^2 $\cdot$ K^4) and e the surface emissivity. The emissivity is the propriety which determinate how much the surface radiates ($0 \leq e \leq 1$). An emissivity value of 1 represents a black body or surface which absorbs and emits energy at maximum rate (Çengel et al., 2019; Gieras et al., 2008; Moran et al., 2014).

The net rate of heat transfer by radiation between (ΔP_{rn}) two gray surfaces (figure 2.52), is given by:

$$\Delta P_r = \sigma \cdot \frac{T_{hot}^4 - T_{cold}^4}{\frac{1-\varepsilon_{hot}}{\varepsilon_{hot} \cdot A_{hot}} + \frac{1}{A_{hot} \cdot F_{cold,hot}} + \frac{1-\varepsilon_{cold}}{\varepsilon_{cold} \cdot A_{cold}}} \tag{2.20}$$

and depends on its area (A_{hot} and A_{cold}), temperature (T_{hot} and T_{cold}), emissivity (ε_{hot} and ε_{cold}) (Gieras et al., 2008). The $F_{hot,cold}$ is the shape factor associated to the relative orientation of the two gray surfaces.

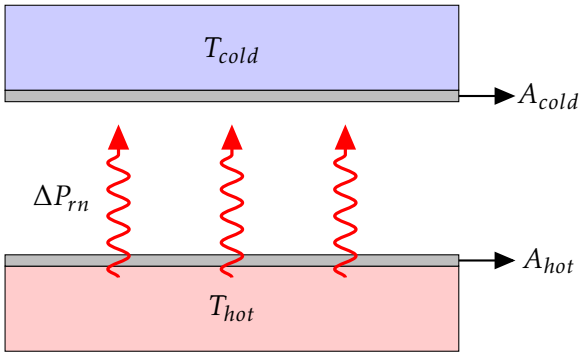

Figure 2.52: Radiation process between two gray surfaces. The red arrows represents the heat flow.

2.5 Chapter Summary

This dissertation is concerned with the thermoelectric-structural simulation of a axial flux superconducting machine stator. So, in this chapter was done a literature review and described the state of the art about the topics that this dissertation deals with.

In section 2.1 and 2.2, a brief introduction about superconductivity and cryogenics is carried out. These sections are not exhaustive, because the machine analysis is focused on the non-superconducting part. For a more in-depth approach on these topics, the reader is recommended to read the bibliography cited throughout these sections.

An overview of superconducting machines is done in section 2.3. There, the history and development of these machines through the years and the respective state of the art are described. Furthermore, an overview of the classification of the superconducting machines and their cryogenic systems is also done.

Finally, in section 2.4, a general overview about the types of losses in electrical machines such as electromagnetic and thermal losses is done.

3

Methodology

3.1 Finite Elements Method (FEM)

3.1.1 Introduction

In 1943, Richard Courant presented discretization methods in triangular elements to solve numerically variational and torsional problems. Later, in 1956 Jon Turner et al. described the types of finite elements, despite at this time this name was not used: triangular, generic quadrangle, and rectangular (Teixeira-Dias, Pinho-da-Cruz, Valente, & Sousa, 2010).

The first mention of Finite Elements Method (FEM) concept was in 1960, by the hands of Ray Clough in the analysis of elasticity problems (Koutromanos, 2018; Teixeira-Dias et al., 2010). At this point, the mathematical rigor of the FEM was very questioned. However, in 1973, Gilbert Strang and George J. Fix, gave a rigorous mathematical formulation of the FEM with a method explication and his convergence conditions. This gave credibility to the FEM (Koutromanos, 2018).

Nevertheless, there is another issue that created difficulties to the extensive use of the FEM: the computational resources. In the 1970s the available hardware does not support sophisticated solutions and the processing time was long. Since then, with the advent of high-performance computing, there was a significant improvement in the speed of processing and quality of the FEM solutions (Koutromanos, 2018).

The FEM is applied in many engineering fields such as: aerospace, automotive, electrical, hydraulic, biomedical, nuclear and structural (Alawadhi, 2016).

3.1.2 Definition and Steps

The FEM is a numerical method to reach a solution related to a variable or stable field which crosses a certain domain that can be or not be homogeneous as well linear or anisotropic. It consists of four main steps (Bianchi, 2005):

- **1º - Discretization of the domain**: the domain Γ with boundary C is discretized into N_m elements (also called sub-domains) connected by N_n nodes (figure 3.1). The

set of finite elements is called mesh. For a static domain, the larger the number of elements, more refined the mesh is (Alawadhi, 2016; Bianchi, 2005).

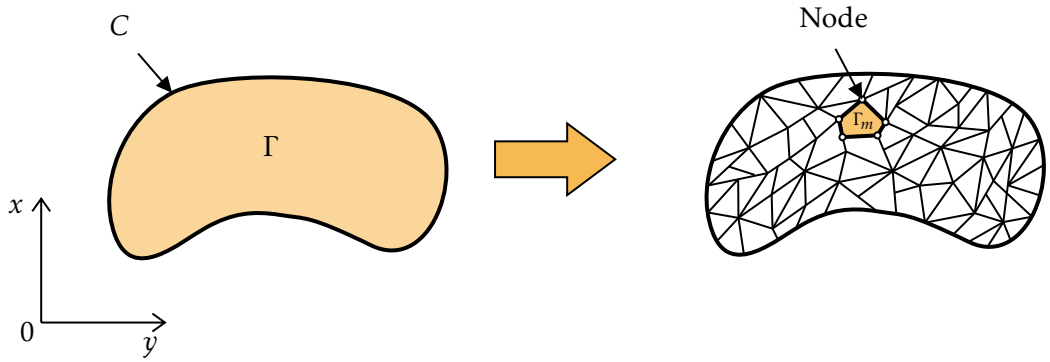

Figure 3.1: FEM discretization process of a domain Γ with boundary C divided into N_m sub-domains (Teixeira-Dias, Pinho-da-Cruz, Valente, & Sousa, 2010).

Each finite element can acquire shapes depending on the dimension of the problem (Bianchi, 2005; Teixeira-Dias et al., 2010):

- Uni-dimensional: net segments (figure 3.2a);
- Bi-dimensional: triangles or quadrilateral (figure 3.2b);
- Tri-dimensional: tetrahedrons, pentahedrons or hexahedrons (figure 3.2c).

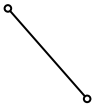

(a) Uni-dimensional

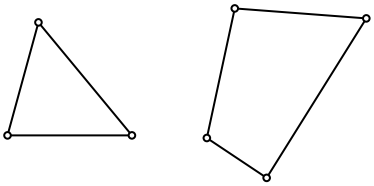

(b) Bi-dimensional

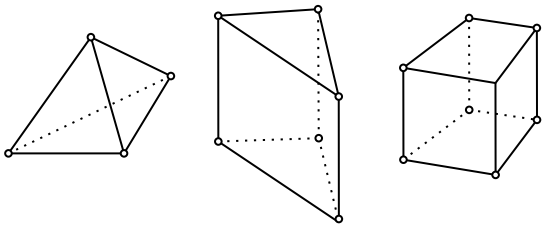

(c) Tri-dimensional

Figure 3.2: Possible shapes for finite elements. The nodes are represented by circles (Bianchi, 2005; Teixeira-Dias, Pinho-da-Cruz, Valente, & Sousa, 2010).

- 2º - **Choice of the interpolating functions**: for each element, an interpolating function is approximated. The higher the approximation order, the more accurate the analysis will be.

- **3º - Formulation of the system**: a system with N_n equations is obtained considering the relations between the N_m elements:

$$\mathbf{F} = [K] \cdot \mathbf{\Delta} \tag{3.1}$$

  where $\mathbf{\Delta}$ is the displacement vector and determines the position after the forces have been applied and $[K]$ is the stiffness matrix with dimension $N_n \times N_n$. So, multiplying both, the force vector $\mathbf{F}$ is obtained. If the three nodes move equally or rotating around a axis without any distortion, the force vector is equal to zero. When a distortion of the sub-domain occurs, this vector assume any value different to zero. It is important to note that both $\mathbf{F}$, $[K]$ and $\mathbf{\Delta}$ for the entire domain are the sum of each N_m elements counterparts:

$$\sum_{m=1}^{N_m} \mathbf{F_m} = \sum_{m=1}^{N_m} [K_m] \cdot \mathbf{\Delta_m} \tag{3.2}$$

  where $\mathbf{F_m}$, $[K_m]$ and $\mathbf{\Delta_m}$ are the $\mathbf{F}$, $[K]$ and $\mathbf{\Delta}$ components of each element, respectively.

- **4º - Solution of the problem**: with the system already computed, through numerical methods, is possible to reach to the problem solution.

The FEM is not an analytical method, but a numerical one. So, the final solution is always an approximation caused by the inherent errors of the numerical computations and model idealizations (Bi, 2018; Bianchi, 2005). Another important issue is the antagonism between the computation time and the accuracy of the final solution. A very accurate solution always demands a computation time that is sometimes not feasible, even when are used computers with high processing capacity. To overcome this problem, without prejudice to the final solution, is to analyze partially the model, though some periodicity or symmetry as described in section 3.1.3.

Furthermore, another important aspect to deal is the dimension of the solution. One-dimensional solution are more expedient to analyse than two-dimensional and three-dimensional. Thus, it is always up to the user to find a compromise solution between computing time and desired accuracy (Bianchi, 2005).

An example of this is described by the 2G High Temperature Superconducting (HTS) (RE)BCO compounds, which have a large width with a thick thickness, resulting in a very large aspect ratio (between 1000 and 10000). Due to that, even in a two-dimensional analysis, the mesh degree of freedom becomes very large, resulting in a large computational time (Brambilla, Grilli, Martini, & Sirois, 2008). This is a problem when, for example, a complete evaluation of a PSCM with conventional and superconducting parts is performed. With that, the order of magnitude between the two parts is different.

On another side, the advantages of the FEM are wide, allowing, for example, a reduction of the prototype number, because it is a purely computational method (Bianchi,

2005). Despite that, the analysis done is very detailed, allowing a complete analysis of a wide variety of engineering problems such as: solid mechanisms, dynamics, heat problems, fluid flows and electromagnetic (Bi, 2018).

3.1.3 Boundary Conditions

The obtained solutions by the FEM are only valid in the interior of the domain Γ and not on its boundary C. To define C, there are three possible conditions: Dirichlet, Neumann and periodic (Bianchi, 2005).

The Dirichlet condition consists of the attribution of a constant value to the magnetic potential vector ($\mathbf{A}$) along the boundary. It is common to give zero value to this vector, to isolate the analyzed model (figure 3.3). Physically, this is equivalent to covering the entire domain by an isolating material (Bianchi, 2005).

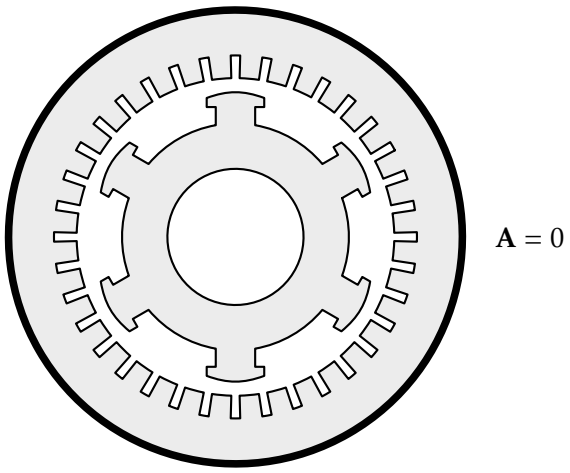

Figure 3.3: Dirichlet condition in a synchronous generator with six salient poles. The bold line around the machine is the boundary where **A** is zero (Bianchi, 2005).

The Neumann condition imposes a value to **A** to the lines that have a determined angle with the boundary (figure 3.4). In the homogeneous condition of Neumann case, the lines are perpendicular. Likewise the Dirichlet condition, this condition is equivalent to covering all the domains by an isolating material. This condition is important to establish symmetries in the model to reduce the computation time as already described in section 3.1.2.

The periodic condition lies in assigning a function that defines the **A** value in function of some partition. This condition could be used in the rotating machine's analysis, because the fields repeat periodically, depending on the pole number. Hence, the model is significantly reduced, with a reduction of the respective computational time (Bianchi, 2005). So, considering the same machine of the figure 3.3, the two types of periodic conditions (even and odd) are presented (figure 3.5). It is important to mention that even

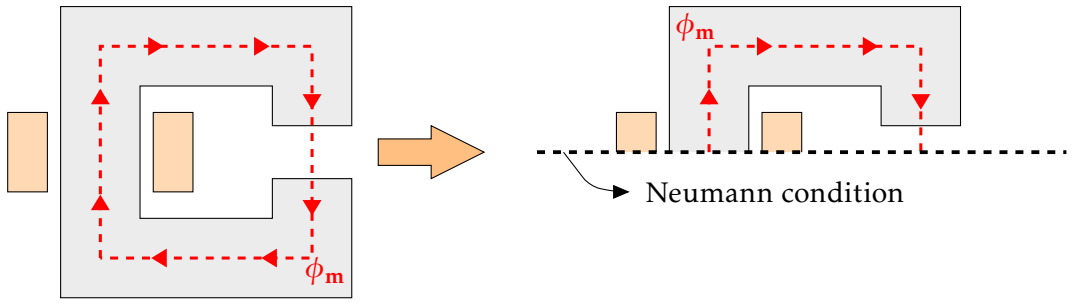

Figure 3.4: Neumann condition in a magnetic circuit with an airgap excited by a winding (at orange), generating the magnetic flux $\phi_{\mathbf{m}}$ (Bianchi, 2005).

in this condition, the Dirichlet one is also applied in the machine exterior boundary (bold black line in figure 3.5).

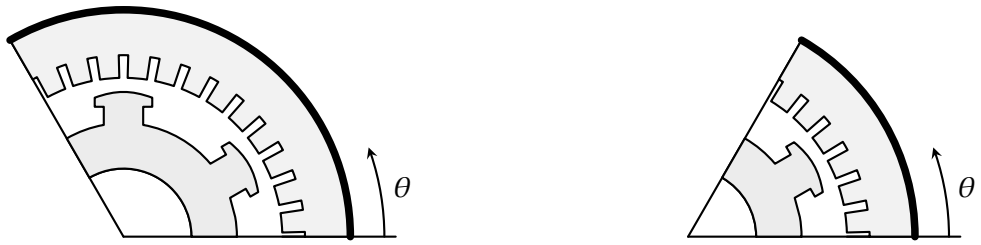

(a) Even. (b) Odd.

Figure 3.5: Periodic functions in the figure 3.3 machine (Bianchi, 2005).

The even condition, analyses one third of the machine (figure 3.5a), imposing in the boundary the following expression for **A**:

$$\mathbf{A}(r_m, \theta) = +\mathbf{A}\left(r_m, \theta + \frac{\pi \cdot k}{p}\right) \tag{3.3}$$

where r_m is the machine radius and p the number of poles. Meanwhile that, the odd condition analyses one sixth of the machine (figure 3.5b) and **A** values in the boundary are defined by:

$$\mathbf{A}(r_m, \theta) = -\mathbf{A}\left(r_m, \theta + \frac{\pi}{2 \cdot p} \cdot (2k - 1)\right) \tag{3.4}$$

3.1.4 Bi-dimensional Example Application

In this section will be presented a simple FEM bi-dimensional example application. Consider a domain Γ constituted by a unique element Γ_1 ($N_m = 1$) with three nodes (figure 3.6). Each node is constituted by a force and displacement component (f_{mn} and δ_{mn}, respectively).

The force ($\mathbf{F_1}$) and displacement vector ($\mathbf{\Delta_1}$) of the element Γ_1 of the figure 3.6 are given by:

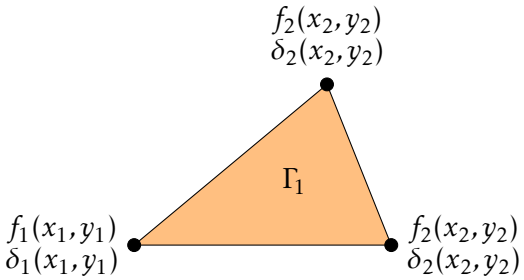

Figure 3.6: Triangular sub-domain Γ_1 with nodal force and displacement components (Teixeira-Dias, Pinho-da-Cruz, Valente, & Sousa, 2010).

$$\mathbf{F_1} = \begin{bmatrix} f_1 \\ f_2 \\ f_3 \end{bmatrix} \tag{3.5}$$

$$\mathbf{\Delta_1} = \begin{bmatrix} \delta_1 \\ \delta_2 \\ \delta_3 \end{bmatrix} \tag{3.6}$$

where f_1, f_2, f_3, δ_1, δ_2 and δ_3 are the respective nodal components. The total number of nodes (N_n) is three, so as already described in section 3.1.2, the stiffness matrix ($[K_1]$) dimension is $N_n \times N_n = 3 \times 3$:

$$[K_1] = \begin{bmatrix} k_{11} & k_{12} & k_{13} \\ k_{21} & k_{22} & k_{23} \\ k_{31} & k_{32} & k_{33} \end{bmatrix} \tag{3.7}$$

Applying the equation 3.1, the equation system of this domain is given by:

$$\begin{bmatrix} f_1 \\ f_2 \\ f_3 \end{bmatrix} = \begin{bmatrix} k_{11} & k_{12} & k_{13} \\ k_{21} & k_{22} & k_{23} \\ k_{31} & k_{32} & k_{33} \end{bmatrix} \cdot \begin{bmatrix} \delta_1 \\ \delta_2 \\ \delta_3 \end{bmatrix} \tag{3.8}$$

Consider now the same domain Γ of figure 3.6 with an adjacent element (Γ_2) (figure 3.7). The N_n of Γ is four, so the stiffness matrix of each element (K_2 and K_2) dimension is $N_n \times N_n = 4 \times 4$. The domain Γ connectivity is represented in table 3.1.

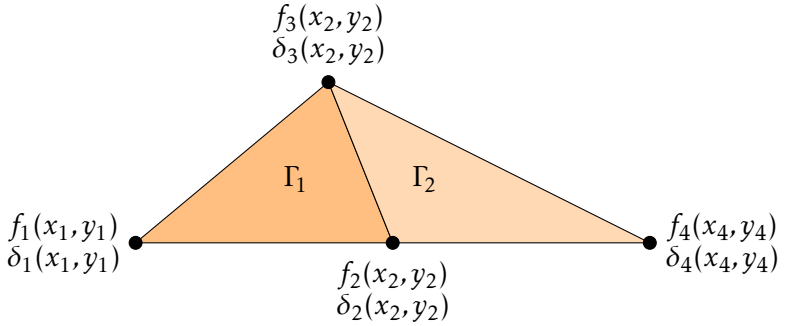

Figure 3.7: Domain Γ with two sub-domains (Γ_1 and Γ_2) with the respective four nodes (Teixeira-Dias, Pinho-da-Cruz, Valente, & Sousa, 2010).

Table 3.1: FEM connectivity of the figure 3.7. The force and displacement component of the n-th node of the m-th element is represented by f_{mn} and δ_{mn}, respectively.

Element (Γ_m)	Nodes (n)	Force vector ($\mathbf{F_m}$)	Stiffness Matrix ($[K_m]$)	Displacement vector ($\mathbf{\Delta_m}$)
Γ_1	1, 2, 3	$\mathbf{F_1} = \begin{bmatrix} f_{11} \\ f_{12} \\ f_{13} \\ 0 \end{bmatrix}$	$[K_1] = \begin{bmatrix} k_{111} & k_{112} & k_{113} & 0 \\ k_{121} & k_{122} & k_{123} & 0 \\ k_{131} & k_{132} & k_{123} & 0 \\ 0 & 0 & 0 & 0 \end{bmatrix}$	$\mathbf{\Delta_1} = \begin{bmatrix} \delta_{11} \\ \delta_{12} \\ \delta_{13} \\ 0 \end{bmatrix}$
Γ_2	2, 3, 4	$\mathbf{F_2} = \begin{bmatrix} 0 \\ f_{22} \\ f_{23} \\ f_{24} \end{bmatrix}$	$[K_2] = \begin{bmatrix} 0 & 0 & 0 & 0 \\ 0 & k_{222} & k_{223} & k_{224} \\ 0 & k_{232} & k_{233} & k_{234} \\ 0 & k_{242} & k_{243} & k_{244} \end{bmatrix}$	$\mathbf{\Delta_2} = \begin{bmatrix} 0 \\ \delta_{22} \\ \delta_{23} \\ \delta_{24} \end{bmatrix}$

As can be seen, the nodes 2 and 3 are shared by Γ_1 and Γ_2. So, according to equation 3.2 the force and displacement components of them is the sum of the respective components of both elements:

$$\begin{bmatrix} f_{11} \\ f_{12}+f_{22} \\ f_{13}+f_{23} \\ f_{24} \end{bmatrix} = \begin{bmatrix} k_{111} & k_{112} & k_{113} & 0 \\ k_{121} & k_{122}+k_{222} & k_{123}+k_{223} & k_{224} \\ k_{131} & k_{132}+k_{232} & k_{133}+k_{233} & k_{134} \\ 0 & k_{242} & k_{243} & k_{244} \end{bmatrix} \cdot \begin{bmatrix} \delta_{11} \\ \delta_{12}+\delta_{22} \\ \delta_{13}+\delta_{23} \\ \delta_{24} \end{bmatrix}$$
$$\Leftrightarrow \begin{bmatrix} f_1 \\ f_2 \\ f_3 \\ f_4 \end{bmatrix} = \begin{bmatrix} k_{11} & k_{12} & k_{13} & 0 \\ k_{21} & k_{22} & k_{22} & k_{24} \\ k_{31} & k_{32} & k_{33} & k_{34} \\ 0 & k_{242} & k_{243} & k_{44} \end{bmatrix} \cdot \begin{bmatrix} \delta_1 \\ \delta_2 \\ \delta_3 \\ \delta_4 \end{bmatrix} \tag{3.9}$$

3.1.5 Electromagnetic Analysis

Regarding the electromagnetic analysis, the FEM study is based on the Maxwell's Laws (Kohnke, 1999):

$$\begin{cases} \nabla \times \mathbf{H} = \mathbf{J} + \dfrac{\partial \mathbf{D}}{\partial t} \\ \nabla \times \mathbf{E} = -\dfrac{\partial \mathbf{B}}{\partial t} \\ \nabla \cdot \mathbf{B} = 0 \\ \nabla \cdot \mathbf{D} = \rho \end{cases} \tag{3.10}$$

where **H**, **B**, **J**, **E**, **D** are the magnetic field, magnetic flux, current density, electric field and electric flux density vector, respectively. **H** is composed by the generalized field $\mathbf{H_g}$ and the gradient of the generalized potential $\mathbf{H}_\phi$:

$$\mathbf{H} = \mathbf{H_g} + \mathbf{H}_\phi \tag{3.11}$$

$\mathbf{H_g}$ is calculated at the integration points using the element shape function ($[N]$) and **B** is calculated by the elementary relation between it and **H**, to according with follows equations, respectively:

$$\mathbf{H}_\phi = -\nabla \cdot [N] \cdot \phi_\mathbf{g} \tag{3.12}$$
$$\mathbf{B} = [\mu] \cdot \mathbf{H} \tag{3.13}$$

where $[\mu]$ is the permeability matrix.

The magnetic forces can given by different method solvers such as magnetic potential results, described by:

$$\mathbf{B} = \nabla \times [N_A] \cdot \mathbf{A_n} \tag{3.14}$$

$$\mathbf{H} = [\mathcal{R}] \cdot \mathbf{B} \tag{3.15}$$

where $[\mathcal{R}]$ is the reluctance matrix, $\mathbf{A_n}$ is the nodal magnetic vector potential and $[N_A]$ is the element shape functions of this last one.

The current density ($\mathbf{J}$) for N_n nodes is calculated according to the following equation:

$$\mathbf{J} = -\frac{1}{[\rho]}\frac{1}{N_n}\sum_{n=1}^{N_n}[N_A]^T \cdot \frac{\partial A_n}{\partial t} - \frac{1}{[\rho]}\frac{1}{N_n}\sum_{n=1}^{N_n}\nabla[N_V]^T \cdot V_n + \mathbf{v_c} \times \mathbf{B} \tag{3.16}$$

where $[\rho]$ is the resistivity matrix, V_n the nodal electric scalar potential, $\mathbf{v_c}$ the current velocity vector. $[N_V]$ is the element shape functions for the electric scalar potential.

To calculate the magnetic forces, there are three available methods: Lorentz, Maxwell and Virtual force. The Lorentz Force ($\mathbf{F_{jb}}$) method is applied in current carrying conductors with volume $\mathcal{V}$:

$$\mathbf{F_{jb}} = \int_{\mathcal{V}} [N]^T (\mathbf{J} \times \mathbf{B}) d\mathcal{V} \tag{3.17}$$

The Maxwell Force ($\mathbf{F_{mx}}$) method is used to determinate forces on ferromagnetic regions with surface $\mathcal{S}$:

$$\mathbf{F_{mx}} = \frac{1}{\mu_0}\int_{\mathcal{S}} \begin{bmatrix} B_x^2 - \frac{1}{2}|\mathbf{B}|^2 & B_x \cdot B_y \\ B_x \cdot B_y & B_y^2 - \frac{1}{2}|\mathbf{B}|^2 \end{bmatrix} \cdot \begin{bmatrix} d_x \\ d_y \end{bmatrix} d\mathcal{S} \tag{3.18}$$

where B_x and B_y are the x and y components of $\mathbf{B}$. δ_x and δ_y are the displacement vector x and y components. In virtual force ($\mathbf{F_s}$) method, the body acting forces in the surroundings are summed is used for determinate the body total force acting. To do that the forces in the surrounding air can be summed. So, the virtual force ($\mathbf{F_s}$) expression determines the force of an air element in the virtual displacement $[d_v]$ direction:

$$\mathbf{F_s} = \int_{\mathcal{V}} [B]^T \frac{\partial H}{\partial d_v} d\mathcal{V} + \int_{\mathcal{V}} \left(\int [B]^T dH \right) \frac{\partial}{\partial d_v} d\mathcal{V} \tag{3.19}$$

As the magnetic forces, the electric ones are also obtained by many solvers. In this case the equations for the electric potential results are described by:

$$\mathbf{E} = -\nabla \cdot [N]^T \cdot V_n \tag{3.20}$$

$$\mathbf{D} = -[\varepsilon] \cdot \mathbf{E} \tag{3.21}$$

where $[\varepsilon]$ is the permittivity matrix. Similarly to the equation 3.18, the electrostatic force ($\mathbf{F_{el}}$) in a surface with area $\mathcal{S}$, are obtained by the following equation:

$$\mathbf{F_{el}} = \varepsilon_0 \int_{\mathcal{S}} \begin{bmatrix} E_x^2 - \frac{1}{2}|\mathbf{E}|^2 & E_x \cdot E_y \\ E_x \cdot E_y & E_y^2 - \frac{1}{2}|\mathbf{E}|^2 \end{bmatrix} \cdot \begin{bmatrix} d_x \\ d_y \end{bmatrix} d\mathcal{S} \tag{3.22}$$

where E_x and E_y are respectively the x and y components for the electric field vector and ε_0 is the vacuum permeability.

The Joule heat per unit volume ($\dddot{Q}$), for electrostatic and transient analysis is given by:

$$\dddot{Q} = \frac{1}{N_n} \sum_{n=1}^{N_n} [\rho] \cdot J_n^2 \tag{3.23}$$

where J_n is the nodal current density.

3.1.5.1 Thermal Analysis

The FEM study in thermal problems is based on the thermal energy conservation, i.e, 1st Law of Thermodynamics (Kohnke, 1999). Considering the temperature as space and time function ($T(x,y,z,t)$):

$$T(x,y,z,t) = [N(x,y,z)]^T \cdot \mathbf{T_n(t)} = [N]^T \cdot \mathbf{T_e} \tag{3.24}$$

$$\frac{T(x,y,z,t)}{dt} = [N(x,y,z)]^T \cdot \frac{\mathbf{T_n(t)}}{dt} = [N]^T \cdot \frac{\mathbf{T_n(t)}}{dt} \tag{3.25}$$

$$\Delta T = \Delta \mathbf{T_n(t)}^T \cdot [N(x,y,z)] = \Delta \mathbf{T_n}^T \cdot [N] \tag{3.26}$$

$$\nabla T(x,y,z,t) = \nabla \mathbf{T_n(t)} \cdot [N(x,y,z)]^T = \nabla \mathbf{T_n} \cdot [N]^T \tag{3.27}$$

where $[N(x,y,z)]$ is the element shape functions matrix regarding the space and $\mathbf{T_n(t)}$ is the time vary nodal temperature vector. So, the heat generation rate per unit volume ($\mathbf{\Delta \dddot{Q}}$) is given by:

$$\Delta \dddot{Q} = \mathcal{D} \cdot c_p \cdot \left(\frac{\partial T}{\partial t} + \mathbf{v_h} \cdot \nabla T \right) + \nabla \cdot \phi_\mathbf{q} \tag{3.28}$$

where $\mathcal{D}$ is the density, c_p the specific heat, $\mathbf{v_h}$ the heat velocity vector and $\phi_\mathbf{q}$ the heat flux vector. Applying the Fourier's Law as described on the equation 2.17 in a differential form:

$$\phi_\mathbf{q} = -[k_c] \cdot \nabla T \tag{3.29}$$

where $[k_c]$ is the thermal conductivity matrix. Combining the equations 3.28 and 3.29:

$$\Delta \dddot{Q} + \nabla \cdot ([k_c] \cdot \nabla T) = \mathcal{D} \cdot c_p \cdot \left(\frac{\partial T}{\partial t} + \mathbf{v_h} \cdot \nabla T \right) \tag{3.30}$$

Considering a body with volume $\mathcal{V}$, temperature T_B, conduction area of $\mathcal{S}_c$, convection area of $\mathcal{S}_v$ and multiplying the equation 3.30 by a nodal temperature variation ΔT_n the following is obtained:

$$\begin{aligned} &\int_\mathcal{V} \mathcal{D} \cdot c_p \cdot \Delta T_n \cdot \left(\frac{\partial T_n}{\partial t} + \mathbf{v_h} \cdot \nabla T_n \right) + \nabla \cdot \phi_\mathbf{q} \cdot \Delta T_n \, d\mathcal{V} = \\ &\int_{\mathcal{S}_c} \phi_\mathbf{q} \cdot \Delta T_n \, d\mathcal{S}_c + \int_{\mathcal{S}_v} k_v \cdot (T_B - T_n) \cdot \Delta T_n \, d\mathcal{S}_v + \int_\mathcal{V} \Delta \dddot{Q} \cdot \Delta T \, d\mathcal{V} \end{aligned} \tag{3.31}$$

By equations 3.24, 3.25, 3.26 and 3.27, the equation 3.31 can be rewritten as:

$$[c_p] \cdot \frac{\delta \mathbf{T_n}}{dt} + ([K_T] + [K_D] + [K_C]) \cdot \mathbf{T_n} = \mathbf{Q_F} + \mathbf{Q_C} + \mathbf{Q_H} \tag{3.32}$$

where each element are described in table 3.2.

Table 3.2: Element thermal equations (Kohnke, 1999)

Description	Formula	
Specific heat matrix - $[c_p]$	$\int_{\mathcal{V}} \mathcal{D} \cdot c_p \cdot [N] \cdot [N]^T \, d\mathcal{V}$	(3.33)
Mass transport conductivity matrix - $[K_T]$	$\int_{\mathcal{V}} \mathcal{D} \cdot c_p \cdot \nabla \mathbf{v_h} \cdot [N] \, d\mathcal{V}$	(3.34)
Diffusion conductivity matrix - $[K_D]$	$\int_{\mathcal{V}} [k_c] \cdot \nabla^2 \cdot [N] \cdot [N]^T \, d\mathcal{V}$	(3.35)
Convection surface conductivity matrix - $[K_C]$	$\int_{\mathcal{S}_v} [k_v] \cdot [N] \cdot [N]^T \, d\mathcal{S}_v$	(3.36)
Mass flux vector - $\mathbf{Q_F}$	$\int_{\mathcal{S}_c} \phi_{\mathbf{q}} \cdot [N] \, d\mathcal{S}_c$	(3.37)
Convection surface heat flow vector - $\mathbf{Q_C}$	$\int_{\mathcal{S}_v} k_v \cdot T_B \cdot [N] \, d\mathcal{S}_v$	(3.38)
Heat generation load vector - $\mathbf{Q_H}$	$\int_{\mathcal{V}} \Delta \ddot{Q} \cdot [N] \, d\mathcal{V}$	(3.39)

3.1.6 Structural Analysis

For simplicity reasons, in this section will be discussed the structural analysis for linear materials. In the structural analysis, there are two important material characteristics: Young's modulus, Poisson's ratio, and shear modulus.

Considering a linear material (figure 3.8), the Young's modulus (Y) is the ratio between the material stress (σ) and strain (ϵ):

$$Y = \frac{\sigma}{\epsilon} = \frac{\frac{F_\sigma}{A_\sigma}}{\frac{\delta L}{L}} = \frac{F_\sigma \cdot L}{A_\sigma \cdot \delta L} \tag{3.40}$$

where the L is the material length that changes with the strain. Generally, Y is the same for stress and strain, and its value is high. For instance, 200×10^9 for steel (Hearn, 1997).

For other side, when the figure 3.8 material is subjected to a stress load with a variation positive of the L, it lateral dimensions b and d are reduced. Hence, the lateral strains will be equal and negative:

$$\varepsilon_{lat} = -\frac{\delta b}{b} = -\frac{\delta d}{d} \tag{3.41}$$

So, the Poisson's ratio (ν) is the ratio between the lateral and longitudinal strain (ε_{lat} and ε_L, respectively) and is given by:

$$\nu = \frac{\epsilon_{lat}}{\epsilon_L} = -\frac{\frac{\delta d}{d}}{\frac{\delta L}{L}} = -\frac{\delta d \cdot L}{\delta L \cdot d} \tag{3.42}$$

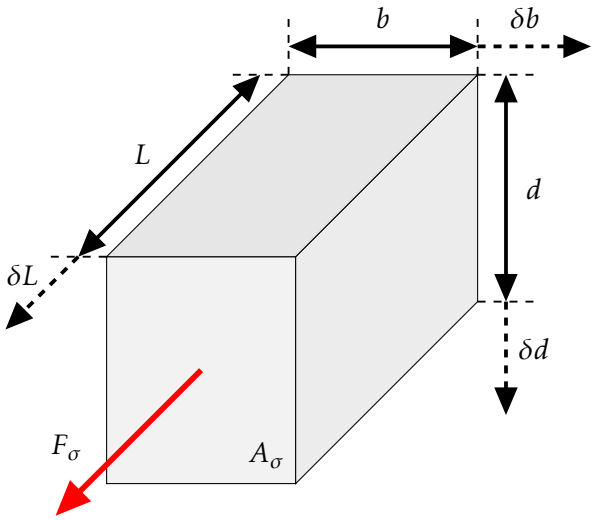

Figure 3.8: Linear material bar with stress load F_σ applied in the area A_σ.

In the most part of the materials, ν is between 0.25 and 0.33 (Hearn, 1997).

The shear or rigidity (G) is the ratio between the shear stress (τ) and shear strain (γ). τ is always tangential to the area on which it acts (figure 3.9) and is calculated by:

$$\tau = \frac{F_G}{A_G} \tag{3.43}$$

where F_G is the shear load and A_G is the area tangential to the last one. While that, the γ is the angle caused by τ in radians.

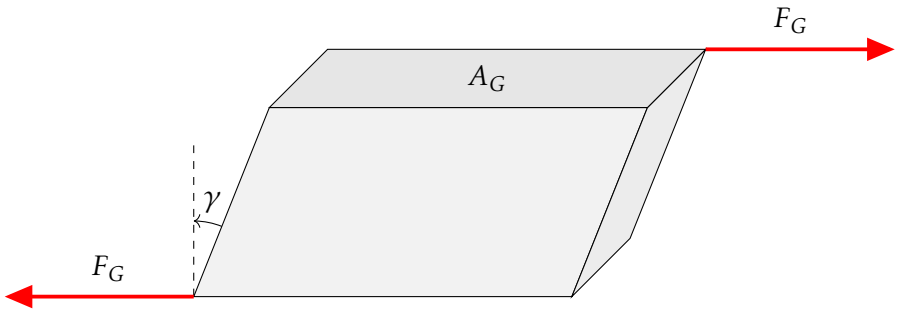

Figure 3.9: Shear applied to a linear material with load F_{sh}, area resisting shear A_{sh} and shear strain of γ.

Thus, G is given by:

$$G = \frac{\tau}{\gamma} = \frac{F_G}{A_G \cdot \gamma} \tag{3.44}$$

Regarding the FEM, the structural analysis is done based on the equation 3.1. Rewriting that equation in function of coordinates, instead of the FEM nodes for the tri-dimensional

case (Kohnke, 1999):

$$\epsilon_{\mathbf{el}} = \epsilon_{\mathbf{th}} + K^{-1} \cdot \sigma \Leftrightarrow \begin{bmatrix} \epsilon_{el}^{x} \\ \epsilon_{el}^{y} \\ \epsilon_{el}^{z} \\ \epsilon_{el}^{xy} \\ \epsilon_{el}^{yz} \\ \epsilon_{el}^{xz} \end{bmatrix} = \Delta T \cdot \begin{bmatrix} \epsilon_{th}^{x} \\ \epsilon_{th}^{y} \\ \epsilon_{th}^{y} \\ 0 \\ 0 \\ 0 \end{bmatrix} + \begin{bmatrix} \frac{1}{E_x} & -\frac{\gamma_{xy}}{Y_y} & -\frac{\gamma_{xz}}{Y_z} & 0 & 0 & 0 \\ -\frac{\gamma_{yx}}{Y_x} & \frac{1}{Y_y} & -\frac{\gamma_{yz}}{Y_z} & 0 & 0 & 0 \\ -\frac{\gamma_{zx}}{Y_x} & -\frac{\gamma_{zy}}{Y_y} & -\frac{1}{Y_z} & 0 & 0 & 0 \\ 0 & 0 & 0 & \frac{1}{G_{xy}} & 0 & 0 \\ 0 & 0 & 0 & 0 & \frac{1}{G_{yz}} & 0 \\ 0 & 0 & 0 & 0 & 0 & \frac{1}{G_{xz}} \end{bmatrix} \cdot \begin{bmatrix} \sigma^{x} \\ \sigma^{y} \\ \sigma^{z} \\ \sigma^{xy} \\ \sigma^{yz} \\ \sigma^{xz} \end{bmatrix} \quad (3.45)$$

where $\epsilon_{\mathbf{el}}$ and $\epsilon_{\mathbf{th}}$ is the elastic and thermal strain vector, $[K]^{-1}$ is the stiffness inverse matrix and the σ is the stress vector. For orthotropic materials[1], $[K]^{-1}$ is symmetric:

$$\frac{\gamma_{yx}}{Y_x} = \frac{\gamma_{xy}}{Y_y} \quad (3.46) \qquad \frac{\gamma_{zx}}{Y_x} = \frac{\gamma_{xz}}{Y_z} \quad (3.47) \qquad \frac{\gamma_{zy}}{Y_y} = \frac{\gamma_{yz}}{Y_z} \quad (3.48)$$

For isotropic materials[2] the shear modulus components (G_{xy}, G_{yz} and G_{xz}) are obtained by the equation 3.49. While that, for orthotropic materials, the shear modulus must be a calculation input.

$$G_{xy} = G_{yz} = G_{xz} = \frac{E_x}{2 \cdot (1 + \gamma_{xy})} \quad (3.49)$$

3.2 Analysed Machine

3.2.1 Description

The analysed machine is called Axial Flux Superconducting Motor (AFSM). Is an hysteresis motor that belongs to the Partially Superconducting Machines (PSCM) class, under investigation by the Centre for Technologies and Systems of UNINOVA (CTS-UNINOVA) in partnership with the Institute of Materials Science of Barcelona (ICMAB-CISC) and the University of Extremadura (UEx). The configuration of this machine is Double-Stator Single-Rotor (DSSR) with an Axial Flux Interior Rotor (AFIR). As represented in figure 3.10, it is constituted by a disk rotor made of thin YBCO 2G HTS strips between two conventional ferromagnetic semi-stators.

The Axial Flux Superconducting Motor (AFSM) is based on the concept of *Polyphase Motor with Variable Number of Poles* described on the registered patent Pina, 2010b. The stator windings configuration can be changed to change the number of poles to optimize the performance of the machine at each moment of operation. For instance, in the start, more torque is necessary to take the motor out of the inertia, so the number of poles is increased. With the motor already started, more rotation speed are needed and the number of poles decreased.

The first prototype of this machine was constituted by a solid HTS disc rotor and conventional ferromagnetic stator. This prototype was tested and characterized in D.

[1] With different mechanical and thermal properties in every direction.
[2] With uniform mechanical and thermal properties in every direction.

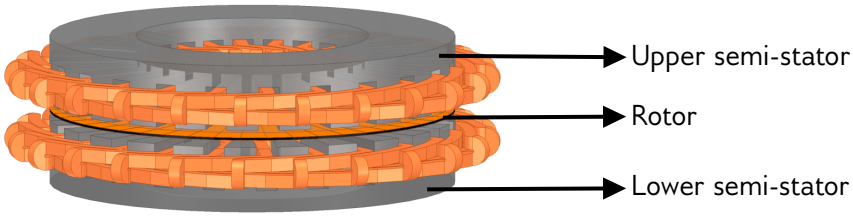

Figure 3.10: AFSM constitution.

Inácio et al., 2009; D. Inácio et al., 2011; D. D. P. Inácio, 2014. The obtained results were far beyond the expectations. The torque of the AFSM was expected to be 3 to 5 times higher than the conventional counterpart, but that does not happen. The possible explanations for this behavior are (D. D. P. Inácio, 2014):

- The considered excitation was low;
- The considered airgap of 0.5 cm was large;
- The magnetic saturation;
- The HTS solid disc was damaged during the tests.

Focusing on the last item, the disc rotor topology of the figure 3.11 was proposed by ICMAB-CISC. It is constituted by carbon fiber, glass fiber, YBCO 2G HTS tape and epoxy layers. The carbon and the glass fiber grant resistance and lightness to the rotor, meanwhile, the epoxy is a coating that is an insulator. Its function is to ensure the adherence of the HTS strips to the rest of the rotor. The HTS strips are radially arranged side-by-side and electrically isolated from each other.

(a) Prototype.

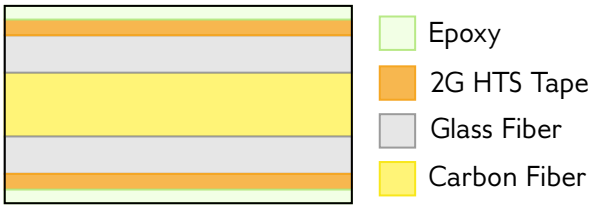

(b) Cross section with its layers. This figure are not to scale.

Figure 3.11: AFSM disc rotor constitution.

3.2.2 Dimensions

Each AFSM semi-stator have 24 winding double-layer slots with width (c) given by the following expression (D. Inácio et al., 2009):

$$c = \frac{p_{avg}}{48} = \frac{\pi \cdot D_{avg}}{48} \tag{3.50}$$

where p_{avg} is the average perimeter of the semi-stator, represented by a dashed line in figure 3.12. D_{avg} is the average semi-stator diameter and is obtained by the average value between the inner and outer diameter (D_{in} and D_{out}, respectively):

$$D_{avg} = \frac{D_{in} + D_{out}}{2} \tag{3.51}$$

The relation between D_{in} and D_{out} is given by the equation 3.52 (D. Inácio et al., 2009).

$$D_{out} = \sqrt{3} \cdot D_{in} \tag{3.52}$$

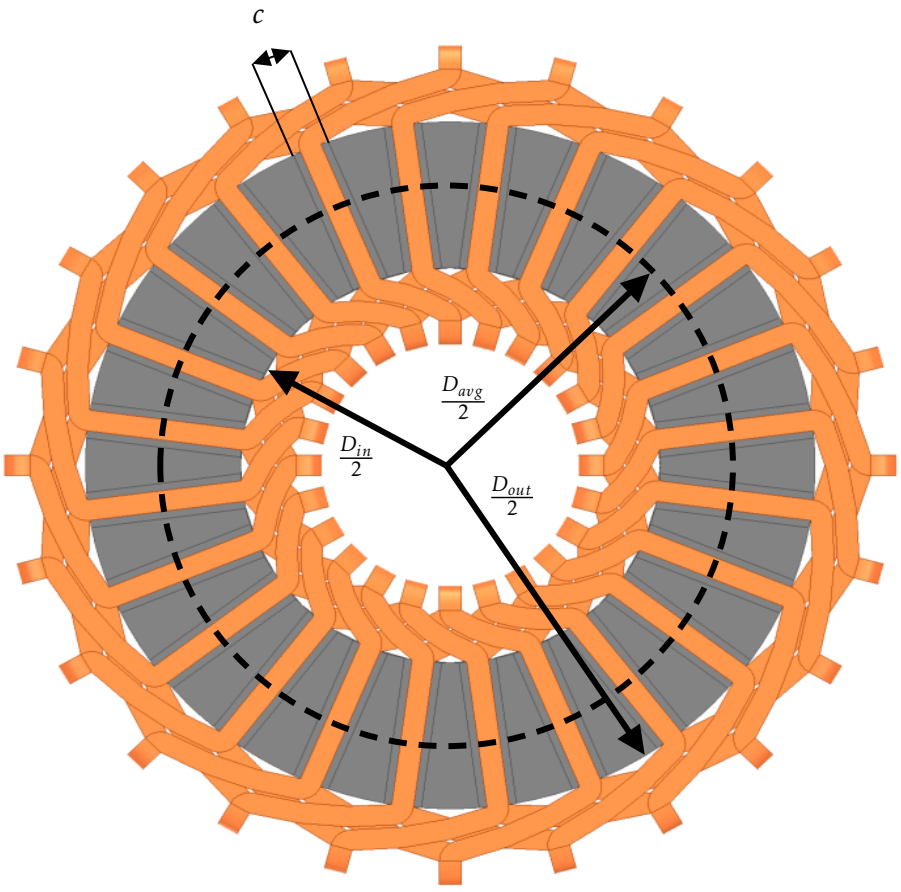

Figure 3.12: Semi-stator parameters. The semi-stator and coils is represented by gray and orange, respectively (D. Inácio et al., 2009).

From equations 3.50, 3.51 and 3.52 the dimensions of the AFSM analysed are represented in table 3.3 (D. Inácio et al., 2009).

Table 3.3: AFSM semi-stator dimensions.

Parameter	**Dimensions** [mm]
c	10.31
D_{out}	200
D_{in}	115
D_{avg}	157.7

The disc rotor has a thickness of 1.2 mm with 48 HTS strips electrically isolated on each side (figure 3.11a). The airgap between the rotor and the semi-stators is 4.3 mm. For more AFSM dimensions, see annex I.

3.3 Types of Analysis

In this dissertation, a thermoelectric-structural AFSM stator analysis is performed using a FEM software which is Ansys, that uses the equations and methodology described in section 3.1. So, the stator analysis is divided into three main components, connected with each other by Ansys Workbench (figure 3.13):

- **Electromagnetic** - to obtain the stator core AC losses ($P_{cr,st}$). As mentioned in section 2.4.2, these losses are the sum between the hysteresis and eddy current losses. The software used is Ansys Electronics Desktop;

- **Thermal** - to obtain the stator temperature variation along the time (T_{st}), as well the thermal flux through the thermal conductivity coefficient (k_c). The software used is Ansys Mechanical;

- **Structural** - to analyse the deformation forces which acts in the semi-stators, like stress (σ_{st}) and strain (ϵ_{st}), caused by the machine heat. The software used is Ansys Mechanical.

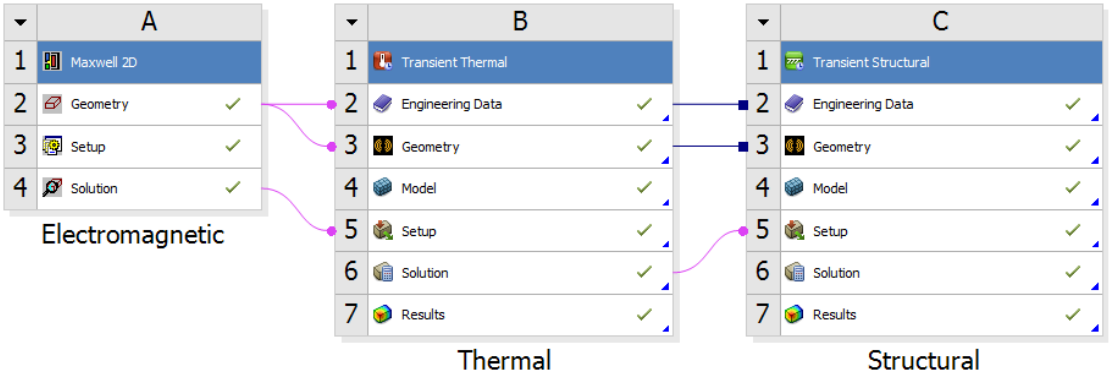

Figure 3.13: Electromagnetic, thermal and structural analysis connectivity on Ansys Workbench.

3.4 Analysed Models

3.4.1 Stator Models

In the present dissertation, a 2D linearized model with 27 winding double-layer slots (figure 3.14a) is considered. This model is a spread-out version of the original 3D rotary (figure 3.14b). The advantage of this model is the less time-consuming analysis when compared to the original 3D rotary model, as already described in section 3.1.2.

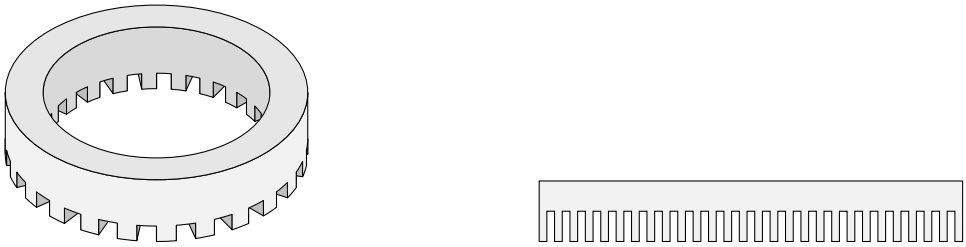

(a) Original 3D rotary model.

(b) Linearized 2D model.

Figure 3.14: Semi-stator models. This figures are not in scale.

The rotor HTS tapes is considered as a perfect conductor. This is a valid approach to this problem because the focus is the stator losses. After all, the HTS losses are negligible comparably to the first ones. In addition, the rotor of both models is stationary, performing thus, an blocked-rotor test with unitary slip ($s = 1$).

The selected semi-stators core material, is Steel M19 with electromagnetic, thermal, and structural properties and B-H curve (table 3.4 and figure 3.4.1, respectively).

Regarding the semi-stator lamination, in this analysis are considered solid and laminated topologies, to found the most efficient configuration. As described in section 2.4.2, laminated stators are used for minimize eddy currents. The analysed semi-stator lamination are described in section 3.4.2. For laminated models, the considered stacking factor (k_i) is 0.95. Considering the equation 2.13, a thermal modifier for the resistivity is also

set. For the thermal analysis, is important to mention that a convection coefficient (k_v) of 50 W/m^2.K has been set.

Table 3.4: Main parameters used for the AFSM stator.

Steel M19 Parameters	
Electromagnetic	
ρ	$5.14\times10^{-7}\cdot[1+\alpha\cdot(T-20)]$
k_i	0.95
Thermal	
α	3×10^{-3} K^{-1}
c_p	448 J/kg.K
k_v	50 W/m^2.K
Structural	
$\mathcal{D}$	7650 kg/m^3
Y	2.04×10^{11} N/m^2
ν	0.3

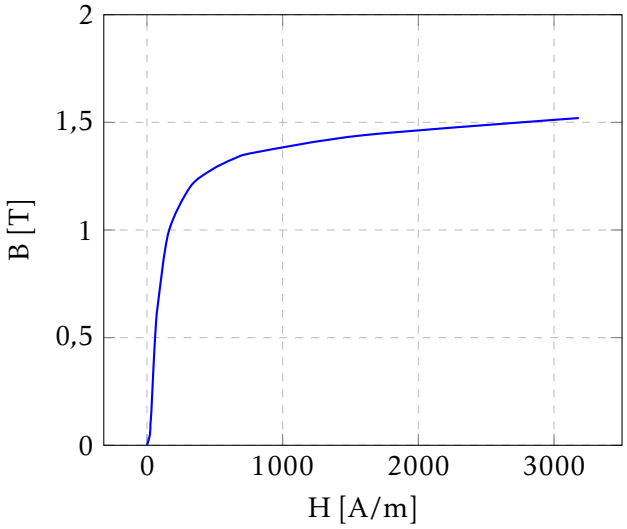

Figure 3.15: B-H curve of the M19 steel.

3.4.2 Semi-stators Lamination Topologies

Regarding the semi-stators lamination, the considered topologies are described in table 3.5.

Table 3.5: Lamination correspondence between rotary and laminated semi-stators.

Topology	Rotary Lamination	Linear Lamination	Representation
1	Solid	Solid	Figure 3.16a
2	Horizontally	Horizontally	Figure 3.16b
3	Circularly	Vertically (y-direction)	Figure 3.16c
4	Radially	Vertically (x-direction)	Figure 3.16d

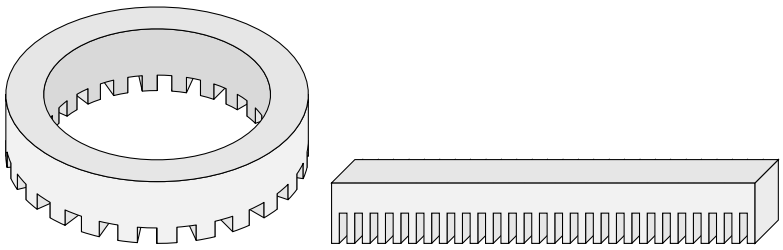

(a) Topology 1

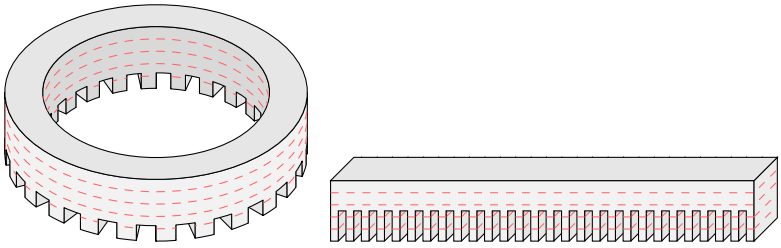

(b) Topology 2

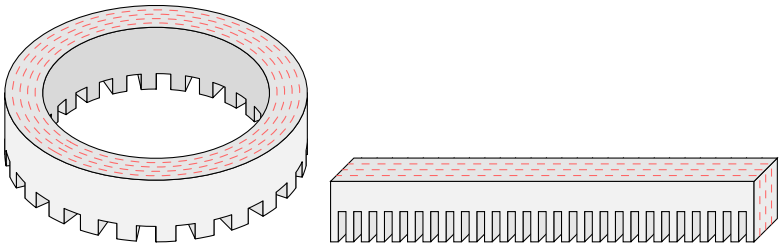

(c) Topology 3

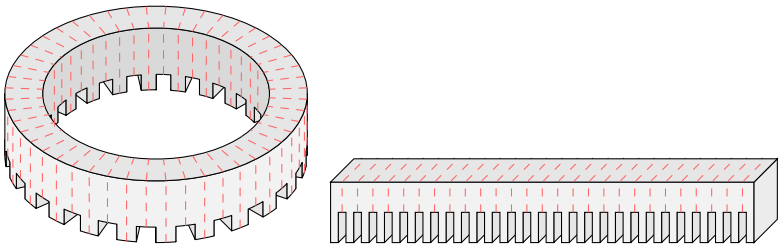

(d) Topology 4

Figure 3.16: Equivalence between the original rotary (at left) and linear model (at right) regarding the semi-stators lamination topologis. The lamination lines are represented by dashed red lines. This figure are not in scale.

3.4.3 Phase and Pole Configurations

Although the AFSM have the capability to change the number of phases, in this dissertation just the three-phase case is studied. So, there are three Y-connected windings, with voltage given by:

$$u_{in}(t) = \begin{cases} u_1(t) = \sqrt{2}\, U_{in,rms}\, \sin(2\pi f t) \\ u_2(t) = \sqrt{2}\, U_{in,rms}\, \sin\left(2\pi f t + \frac{2}{3}\pi\right) \\ u_3(t) = \sqrt{2}\, U_{in,rms}\, \sin\left(2\pi f t + \frac{4}{3}\pi\right) \end{cases} \tag{3.53}$$

where f is the operation frequency which is 50 Hz. The RMS input voltage ($U_{in,rms}$) chosen was 230 V with winding resistance of 10 Ω.

Regarding the pole configuration, the consequent pole configuration is chosen. Three configurations are analysed: two, four and eight poles (figure 3.17).

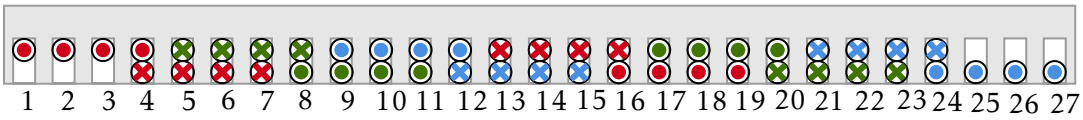

(a) Two-poles.

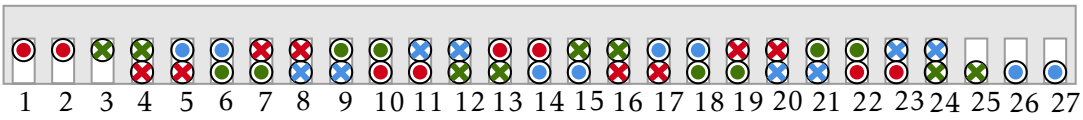

(b) Four-poles.

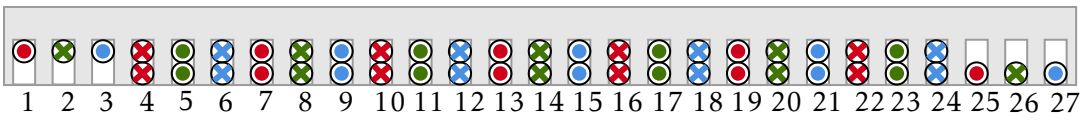

(c) Eight-poles.

Figure 3.17: Consequent pole configurations studied for the linear model. The phase 1, 2 and 3 are represented by red, green and blue, respectively.

3.5 Chapter Summary

In the present chapter, the adopted methodology for the AFSM thermoelectric-structural simulation is described. In this dissertation, the decision to analyze first a 2D linearized model was made to save computational time to obtain results with more celerity.

In section 3.1 there is a brief description about the FEM which simulation software used is based. Furthermore, a description of the equations that this method uses to solve electromagnetic, thermal, and structural problems is carried out.

A detailed description of the analyzed AFSM, as well the respective dimensions, is present in section 3.2.

In section 3.3 is described in detail the three analysis components: electromagnetic, thermal, and structural. In sum, the AFSM semi-stators core losses are analyzed to draw considerations about the stator temperature variation and structural changes.

As described in the first paragraph, two stator models are analyzed. For each one, four stator lamination are analyzed, to compare the losses on each one. These ones, are described in section 3.4.2. Each model is also simulated for three different number of poles: two, four, and eight. All configurations have three phases and consequent poles.

4

Simulation Results and Discussion

4.1 Simulation Settings

In the electromagnetic analysis, the AFSM semi-stators AC losses are analyzed during 50 ms to combine the accuracy of the results and computation time. Nevertheless, in the present analysis, the transient-state is disregarded, with the focus on the steady-state, from 20 ms to 50 ms.

Regarding the thermal analysis, the AFSM semi-stators temperature is analyzed during 30 s to get a more complete and realistic analysis of the machine heat. In this analysis, the AC losses of the electromagnetic analysis are considered. However, it should be noted that the time windows of both analyses are different (50 ms vs. 30 s). So, in thermal analysis, the steady-state losses are considered constant. The initial temperature set is −196.15 °C which is LN_2 operation temperature. This analysis does not consider the evaporation effects of this coolant. For this first approach, the simplest evaluation focused on stator heat is performed.

In the structural analysis, the semi-stator distortion due to the heat is evaluated in the same window time as the thermal analysis. The main goal of this analysis is to evaluate the airgap variation. This is a very important issue because the airgap variation must be minimal to maintain the correct operation of the AFSM.

As already described in section 3.4, in this dissertation three-pole configurations (two, four, and eight) with four semi-stator lamination topologies each other. It is important to remember the reader about the notation used in this chapter for the semi-stator lamination topologies (figure 4.1).

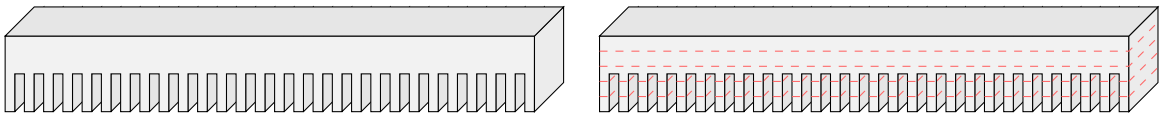

(a) Topology 1: solid.

(b) Topology 2: horizontally laminated.

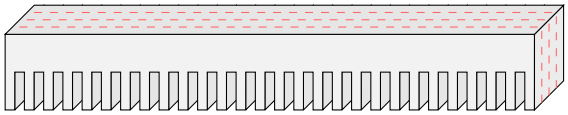

(c) Topology 3: vertically laminated (y-direction).

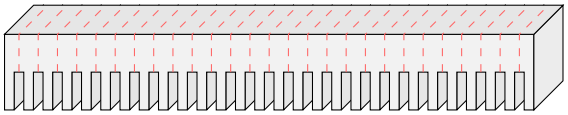

(d) Topology 4: vertically laminated (x-direction).

Figure 4.1: Linearized 2D semi-stators considerated for simulation. The lamination lines are represented by dashed red lines. This figure are not in scale.

4.2 Simulation Results

4.2.1 Electromagnetic Analysis

As described in section 3.4.3, three configurations are analysed: two, four and eight poles. The analyzed machine flux is axial, so the flux lines must be circular in the 2D linearized model (figure 4.2). Another important observation is the decrease of the magnetic flux as the number of pole increases.

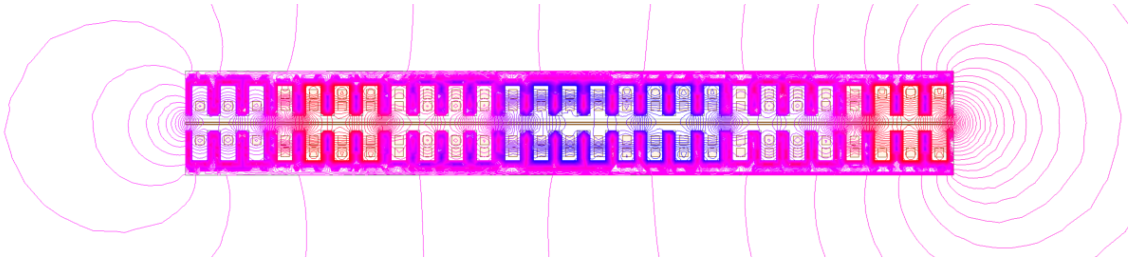

(a) Two-poles .

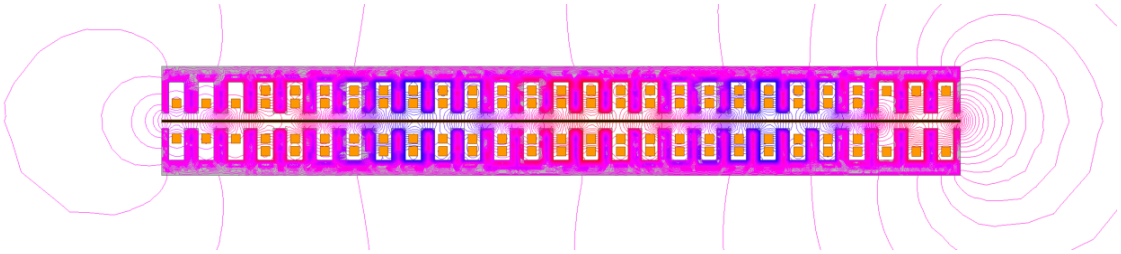

(b) Four-poles.

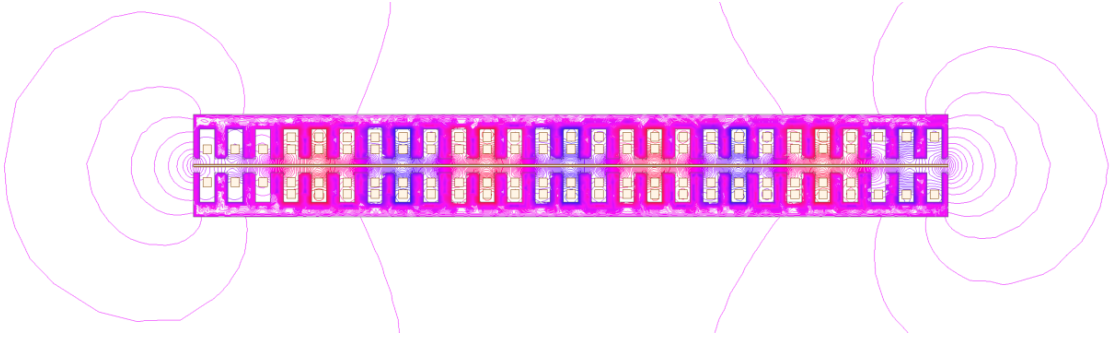

(c) Eight-poles.

Figure 4.2: AFSM flux lines with the poles represented.

The semi-stator AC core losses ($P_{cr,st}$) are obtained for the steady-state (figure 4.3) and it can be observed that in all pole configurations the relative progress is similar, i.e, the topology 3 and 4 have about 39% lower losses than the 1 and 2. Nevertheless, the topology 3 has a small advantage over 4, becoming so, the less AC core losses topology.

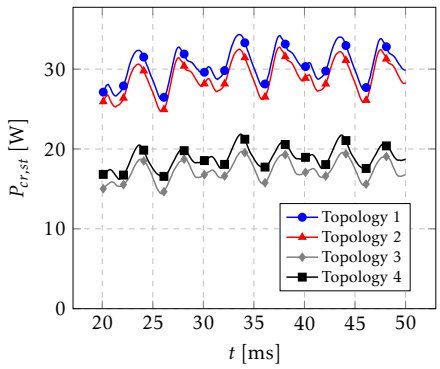

(a) Two-poles.

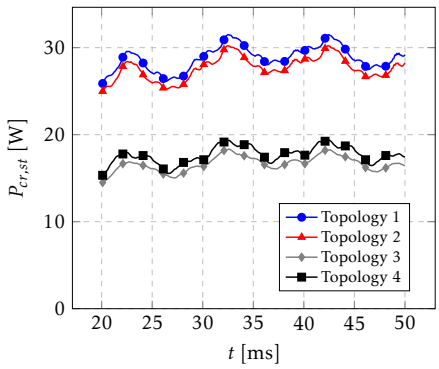

(b) Four-poles.

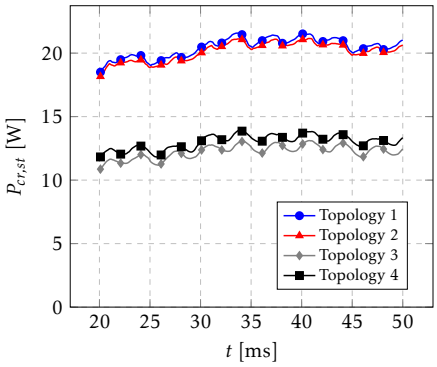

(c) Eight-poles.

Figure 4.3: Steady-state AFSM AC core losses.

4.2.2 Thermal Analysis

The semi-stators temperature distribution is different between pole configurations, while is similar between lamination topologies with the same pole number. In the semi-stators with topology 1 (solid), the temperature distribution at 30 s of operation is represented in figure 4.4. For other topologies, see annex II.1.

As can be seen, whatever the pole configurations, the AFSM tooths is a critical spot. There, the heat is more concentrated because is the nearest point to the windings and between both semi-stators, the heat is transferred by convection. In two-pole configuration (figure 4.4a), there is a hot spot in the middle of the semi-stators concentrated in one tooth. In four and eight-pole configurations (figure 4.4a and 4.4b, respectively), the hot spot is more extensive. In the first configuration is concentrated in both stators, while the second is more concentrated in the lower semi-stator.

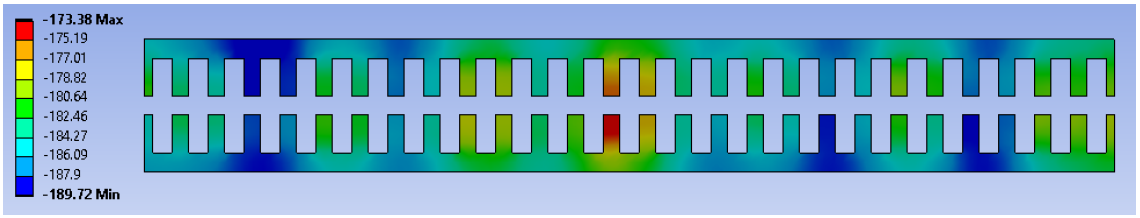

(a) Two-poles.

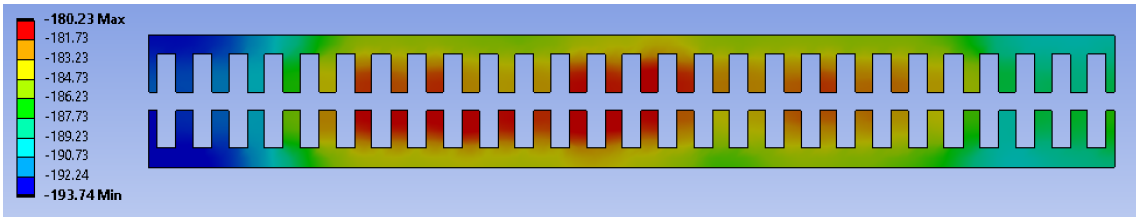

(b) Four-poles.

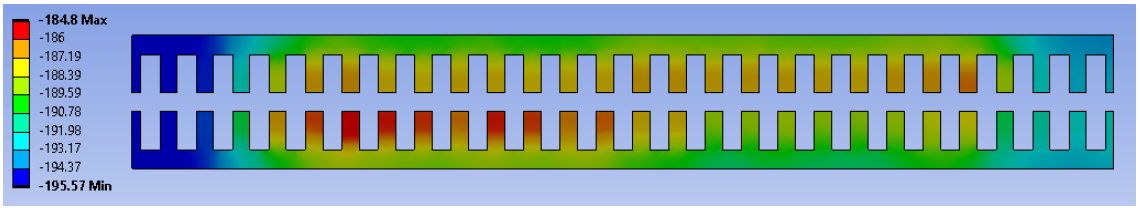

(c) Eight-poles.

Figure 4.4: Topology 1 (solid) AFSM semi-stator temperature in °C distribution at 30 s.

The AFSM semi-stators temperature time evolution is proportional to core losses, as predictable (figure 4.5). At the last moment of this simulation, the stator temperature increase of topology 1 and 2 (solid and horizontally laminated, respectively) is about double of 3 and 4 (vertically laminated in y and x, respectively). Nevertheless, topology 3 has a small advantage against 4, resulting thus in a less temperature increase.

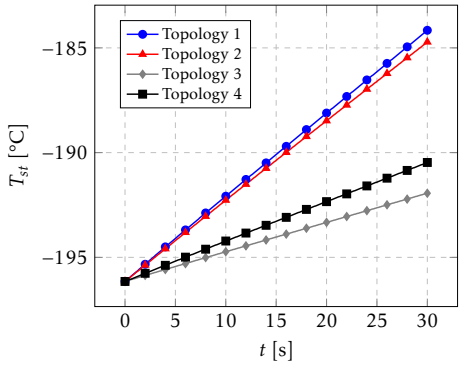

(a) Two-poles.

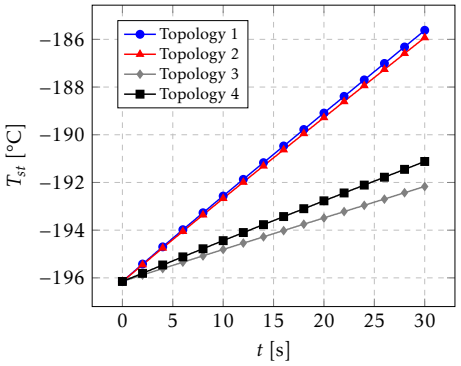

(b) Four-poles.

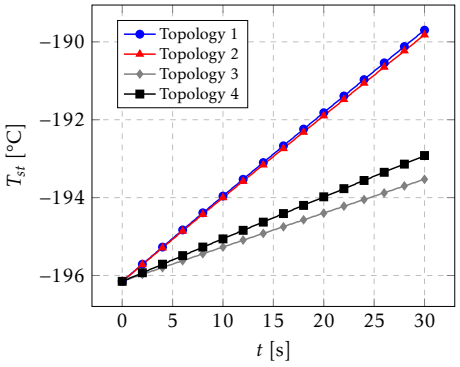

(c) Eight-poles.

Figure 4.5: AFSM semi-stators temperature time evolution.

4.2.3 Structural Analysis

In the structural analysis is observed that the deformation of the AFSM semi-stators acquire different behaviors depending on the pole configuration. Is desirable that the semi-stators deformation be as small as possible. High deformation may cause an airgap reduction which leads to rotor destruction because this one is between the two semi-stators.

The direction of the deformation displacement is the same for each semi-stator topology, differing only in their module. The structural results for topology 1 are represented in figure 4.6. For the other topologies, see annex II.2. The stator deformation in that figure is amplified to get an idea about the directions of the forces. It is important to mention also that the 2D model is not the more suitable for the structural analysis, because the analysis is limited the XY plan.

After 30 s of operation, in a two-pole configuration (figure 4.6a), the direction of the forces tends to an airgap increase, because the hottest point is concentrated in the middle of the machine, so the airgap tends to be decreased. In four and eight-pole configuration (figure 4.6b and 4.6c, respectively), due to the extensive hot points, the airgap in most part tend to be decreased. However, in the eight-pole configuration, the deformation value is smaller, due to the lower temperature increase.

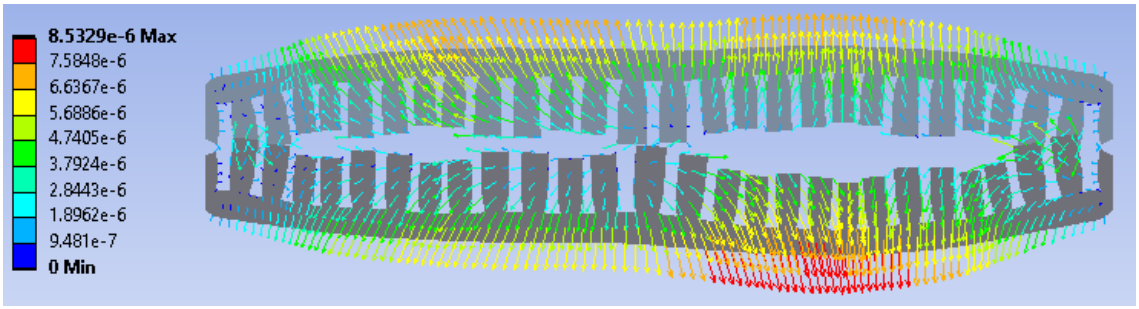

(a) Two-poles.

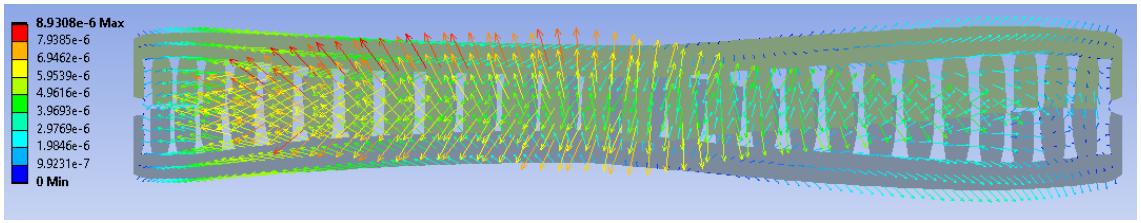

(b) Four-poles.

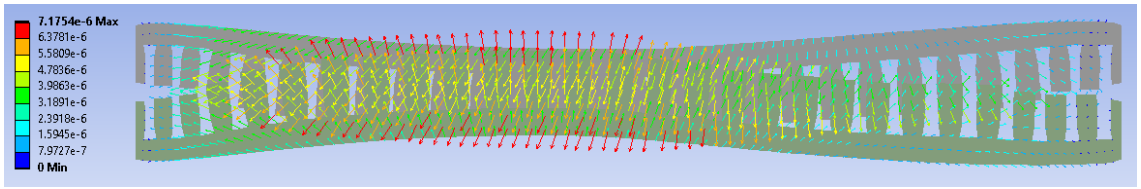

(c) Eight-poles.

Figure 4.6: Topology 1 (solid) AFSM semi-stator deformation displacement in meters at 30 s. The stator deformation in this figure is amplified in order to evaluate the forces direction.

Regarding the semi-stator maximum strain time evolution, on every pole configuration, topology 1 and 2 (solid and horizontally laminated, respectively), have about double of topology 3 and 4 (vertically laminated in x and y-direction, respectively) (figure 4.7). These results are according to the electromagnetic and thermal results, so the topologies that exhibit the lowest strain are 3 and 4.

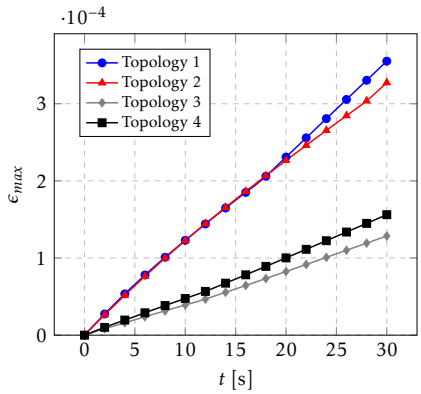

(a) Two-poles.

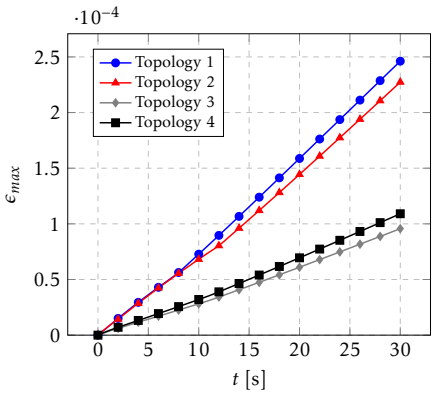

(b) Four-poles.

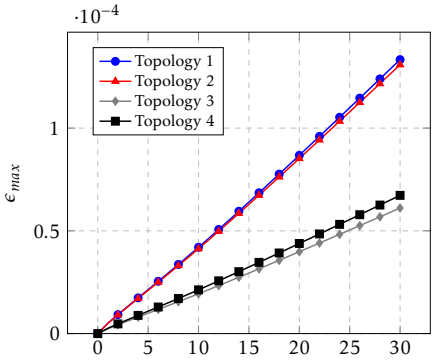

(c) Eight-poles.

Figure 4.7: AFSM semi-stators maximum strain time evolution.

The semi-stators maximum stress time evolution is according to the maximum strain results, with a variation similar to these. This is expected because the ratio between them, i.e, Young modulus (Y) is maintained at the value mentioned in table 3.4. So, the lower stress topologies are 3 and 4 (vertically laminated in x and y-direction, respectively).

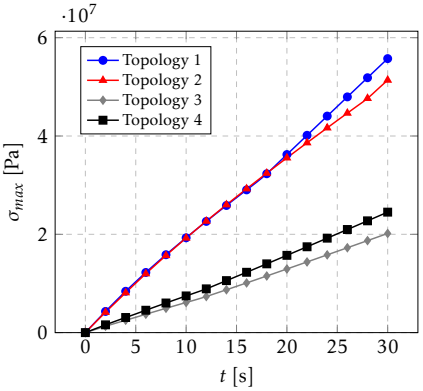

(a) Two-poles.

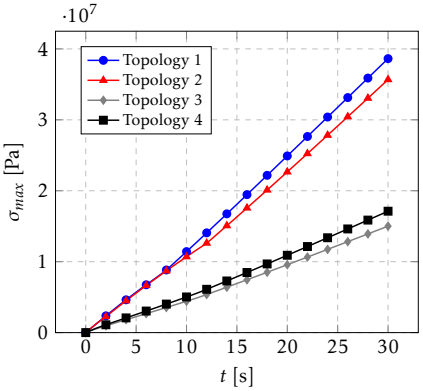

(b) Four-poles.

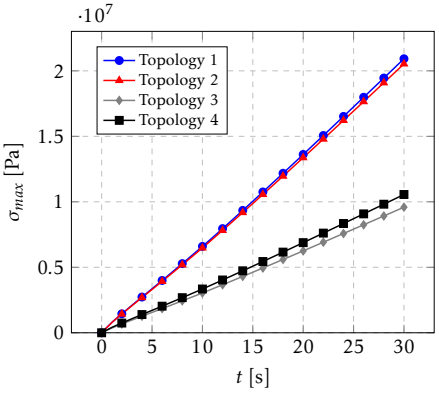

(c) Eight-poles.

Figure 4.8: AFSM semi-stators maximum stress time evolution.

4.3 Results Discussion

In the last three sections, is described each AFSM semi-stators analysis component. Regarding the semi-stator AC core losses, it is higher as the pole number decreases (figure 4.9). So, the semi-stator AC core losses are inversely proportional to the number of poles, whatever stator lamination topology. This occurs because, the AFSM magnetic flux decreases with the number of poles increase, resulting in lower losses. As described in section 3.2.1, this AFSM can change the number of poles to produce more binary or speed. With that, it can be inferred that when the AFSM starts and more torque is needed, the semi-stator losses and consequent heat and deformation are higher because the number of poles needs to be minor. This is something important to take into account when sizing a possible cryogenic refrigeration system, for example.

Another important observation is the similarity between topologies 1/2 (solid and horizontally laminated, respectively) and 3/4 (vertically laminated in y and x-direction, respectively) losses, whatever the pole configuration. With this, it can be stated that the lower losses configuration is the eight-pole with semi-stator topology 3 (vertically laminated in the y-direction). However, it is important to note that topology 4 (vertically laminated in the x-direction) has similar, but slightly larger losses.

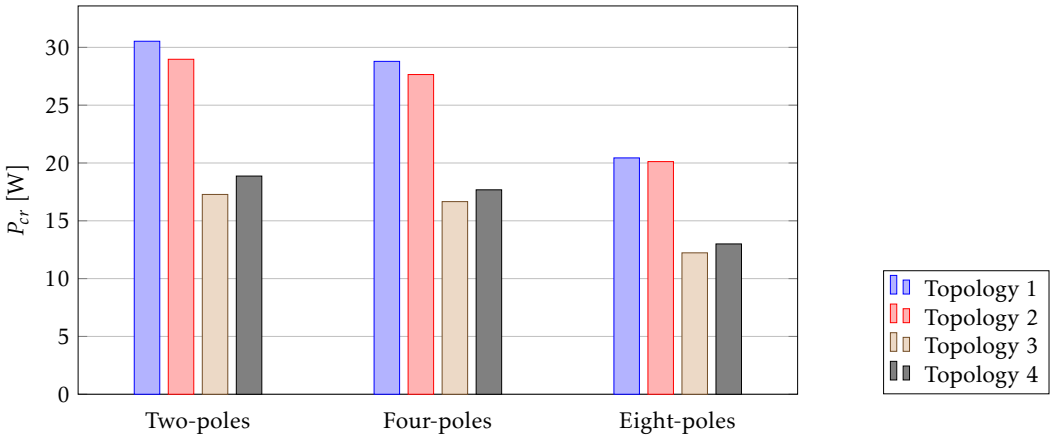

Figure 4.9: Semi-stators average AC core loss in steady-state.

The main results obtained in the analysis performed in this dissertation are represented in table 4.1, where $\overline{P_{cr}}$ is the semi-stator average losses during the steady state, ΔT_{30} is the temperature variation in 30 s, $\epsilon_{30,max}$ and $\sigma_{30,max}$ is the maximum semi-stator stress and strain at 30 s. Comparing that results, it can be noted that the results are in concordance, i.e, the lower losses configurations present the less heat and deformation. The opposite happens for the configuration with more losses. So, the two configurations with less losses are highlighted in that table: topology 3 and 4 (vertically laminated in y and x-direction, respectively) with both eight-pole configurations.

Table 4.1: Electromagnetic, thermal and structural obtained results. The configurations with the lowest losses and deformation is highlighted by bold.

Stator	Poles	$\overline{P_{cr}}$ [W]	ΔT_{30} [°C]	$\epsilon_{30,max}$ $(\cdot 10^{-4})$	$\sigma_{30,max}$ [GPa]
Topology 1	2	30.53	+11.99	3.55	55.75
	4	28.79	+10.53	2.46	38.63
	8	20.44	+6.45	1.33	20.92
Topology 2	2	28.97	+11.43	3.27	51.37
	4	27.65	+10.22	2.27	35.67
	8	20.12	+6.33	1.31	20.53
Topology 3	2	17.28	+4.21	1.29	20.17
	4	16.66	+3.98	0.96	15.01
	8	**12.23**	**+2.62**	**0.61**	**9.59**
Topology 4	2	18.87	+5.68	1.56	24.51
	4	17.68	+5.03	1.09	17.12
	8	**13.00**	**+3.23**	**0.67**	**10.56**

Finally, two considerations about the effectiveness of the results are relevant to be done. The first one concerns the 2D linearization of the AFSM which allows a more expeditious obtaining of results but has limitations. The analysis where this problem is more evident is in the structure where the obtained deformation forces are limited to the XY plane. So, the results obtained there are worthy of being compared with a 3D AFSM analysis to evaluate the airgap variation which is important for the machine performance.

The second and last consideration is about the simulation window time chosen. These results consider a very low time window for an analysis of the real machine behavior. However, the available hardware limitations do not allow such a long analysis in a feasible time frame.

4.4 Chapter Summary

In this chapter, the results for the three AFSM analyses are presented and discussed. In section 4.1, the simulation conditions are presented. For electromagnetic analysis, the simulation time window chosen was different from the thermal and structural analysis to manage more efficiently the simulation computational resources.

In section 4.2.1, 4.2.2 and 4.2.3, the obtained results for the electromagnetic, thermal and structural analysis are shown. In the electromagnetic analysis, the flux lines for each pole configuration are presented with the AC core losses plot as a function of time. In the thermal analysis, the semi-stator temperature distribution and their evolution in the function of time are presented. Finally, in the structural analysis is presented the stator deformation in the last simulation moment and the respective plot of maximum strain and stress as a function of time.

Finally, in section 4.3 a discussion of the results obtained through the mentioned analysis is carried out. It is inferred that the number of poles is inversely proportional to the

semi-stator AC core losses. This one is also proportional to the semi-stator temperature increase and deformation in all simulated configurations and topologies. Furthermore, regarding the stator lamination topology, it is observed that topology 3 and 4 (vertically laminated in y and x-direction, respectively) have lower losses, with a small advantage for the first one.

5

Conclusions and Future Work

5.1 Conclusions

The present dissertation described a thermo-structural analysis of a AFSM is carried out through a FEM simulation program which is Ansys Electronics Desktop, Mechanical, and Workbench. This analysis was focused on semi-stators losses because, in the superconducting rotor, the losses are much lower compared to the first ones. Because the FEM 3D analysis of this machine is very time-consuming and spends too much computer resources, in this dissertation is considered a linearized 2D model. This analysis was divided into three parts: electromagnetic, thermal, and structural.

So, in this first approach to the AFSM semi-stators thermo-structural analysis some conclusions may be drawn. It can be noted that the obtained semi-stators AC core losses is inversely proportional to the number of poles. So, when more torque is required by the machine (in the start, for example) is predictable that the semi-stator losses and deformation will be minor. This is an important aspect to take into account in a possible future cryogenic cooling system design.

Regarding the semi-stator lamination topology, in all analyses performed, topology 1 and 2 (solid and horizontally laminated) present about 39% of the AC losses, and double temperature increase and deformation comparably to the topology 3 and 4 (vertically laminated in y and x-direction). Considering the equivalence between the 3D rotary and the 2D linear semi-stator, the topologies of the last one are equivalent to the circularly and radially laminated, respectively (figure 5.1). However, among these two, the one that showed the lowest losses was topology 3. So, can be concluded that in this analysis the stator lamination that has lower losses is circularly laminated. This topology is the one that can allow a less powerful cryogenic cooling system with the smallest possible airgap variation, resulting in a more AFSM efficiency.

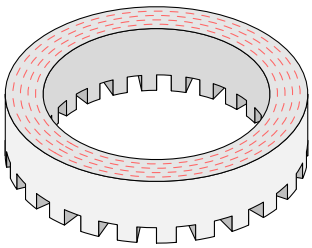

(a) Topology 3: circularly laminated.

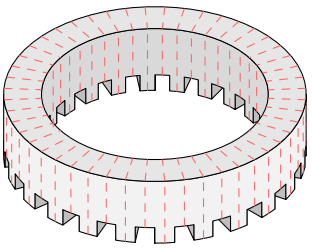

(b) Topology 4: radially laminated.

Figure 5.1: AFSM semi-stator lower losses topologies.

5.2 Future Work

The topic developed through this dissertation was never analyzed before. So, this dissertation consists of a first approach to the AFSM semi-stator thermo-structural analysis. So, the results presented should be the basis for a more complex study of this topic through the following topics:

- Perform a similar 3D analysis of the AFSM with increased window time analysis to compare it to the present 2D linearized model;
- Perform a more complete analysis, considering the AFSM immersed by LN_2 with the respective evaporation rate due to the machine heat caused by the losses.
- Taking advantage of the AFSM capability to change the number of input phases, the analysis of various phase configurations is an interesting point;
- Use the simulated data to test the prototype present in the laboratory with the lamination with less losses and compare it with the simulated results;
- Project the cryogenic system using the obtained thermal data.

Bibliography

Abrikosov, A. (1957). The magnetic properties of superconducting alloys. *Journal of Physics and Chemistry of Solids*, *2*(3), 199–208. doi:https://doi.org/10.1016/0022-3697(57)90083-5. (Cit. on p. 8)

Airbus. (2021). Cryogenics and superconductivity for aircraft, explained. Retrieved August 16, 2021, from https://www.airbus.com/newsroom/stories/ascend-cryogenics-superconductivity-for-aircraft-explained.html. (Cit. on p. 26)

Alawadhi, E. M. (2016). *Finite element simulations using ansys*. CRC Press. (Cit. on pp. 41, 42).

Ballarino, A., & Flükiger, R. (2017). Status of MgB2 wire and cable applications in Europe. *Journal of Physics: Conference Series*, *871*(1). doi:10.1088/1742-6596/871/1/012098. (Cit. on p. 4)

Barnes, G. J., Mcculloch, M. D., & Dew-Hughes, D. (2000). *Torque from hysteresis machines with type-ii superconducting segmented rotors*. Retrieved from www.elsevier.nlrlocaterphysc. (Cit. on p. 30)

Bednorz, J. G., & Miiller, K. A. (1986). *Condensed possible high T_c superconductivity in the ba-la-cu-0 system*. (Cit. on p. 4).

Bi, Z. (2018). *Finite element analysis applications : A systematic and practical approach*. American Press. (Cit. on pp. 43, 44).

Bianchi, N. (2005). *Electrical Machine Analysis Using Finite Elements*. CRC. (Cit. on pp. 41–45).

Blundell, S. (2009). *Superconductivity: a very short introduction*. New York: Oxford University Press. (Cit. on p. 8).

Brambilla, R., Grilli, F., Martini, L., & Sirois, F. (2008). Integral equations for the current density in thin conductors and their solution by the finite-element method. *Superconductor Science and Technology*, *21*. doi:10.1088/0953-2048/21/10/105008. (Cit. on p. 43)

Çengel, Y. A., Boles, M. A., & Kanoğlu, M. (2019). *Thermodynamics: an Engineering Approach* (9th ed.). McGraw-Hill. (Cit. on pp. 37, 38).

Chan, C. C. (1987). Axial-field Electrical Machines—Design and Applications. *IEEE Power Engineering Review, PER-7*(6), 49–50. doi:10.1109/MPER.1987.5527133. (Cit. on p. 32)

Chapman, S. J. (1991). *Electric machinery fundamentals* (5th ed.). McGraw-Hill. (Cit. on pp. 30, 31).

Chen, A., Xu, F., Liu, X., He, Y., Wu, Z., Zhu, Y., ... Li, L. (2012). Sub-cooled liquid nitrogen test system for cooling hts synchronous motor. *IEEE Transactions on Applied Superconductivity, 22*(3), 13–16. doi:10.1109/TASC.2011.2174558. (Cit. on pp. 20, 33)

Duvelleroy, M. (2021). Airbus to boost "cold"technology testing as part of decarbonisation roadmap. Retrieved August 16, 2021, from https://www.airbus.com/newsroom/press-releases/en/2021/03/airbus-to-boost-cold-technology-testing-as-part-of-its-decarbonisation-roadmap.html. (Cit. on p. 26)

Essmann, U., & Trauble, H. (1964). *A83. 2. m. born and k. huang; dynamical theory of crystal lattices (oxford atclarendon, 1954) sec. 44. 3.* (Cit. on p. 9).

Fitzgerald, A., Kingsley Jr., C., & Umans, S. D. (2003). *Electric machinery*. McGraw-Hill. (Cit. on pp. 33–35).

Gieras, J. F. (2009). Superconducting electrical machines - state of the art. *Organ, 12*(9). (Cit. on pp. 4, 25, 28–30).

Gieras, J. F. (2008). *Advancements in Electric Machines*. Springer. (Cit. on pp. 4, 5, 9, 10, 28, 29).

Gieras, J. F. (2017). *Electrical machines : fundamentals of electromechanical energy conversion*. CRC Press. (Cit. on pp. 35, 36).

Gieras, J. F., Wang, R.-J., & Kamper, M. J. (2008). *Axial Flux Permanent Magnet Machines*. Springer. (Cit. on pp. 31, 32, 34, 37–39).

González-Parada, A., Guía, M., Ibarra, O., & Guzmán, R. (2012). Development of axial flux hts induction motors. (Vol. 35, pp. 4–13). doi:10.1016/j.proeng.2012.04.159. (Cit. on p. 31)

Han, H.-S., & Kim, D.-S. (2016). *Magnetic Levitation: Maglev Technology and Applications*. doi:10.1088/0143-0807/9/3/112. (Cit. on pp. 17, 18)

Haran, K. S., Kalsi, S., Arndt, T., Karmaker, H., Badcock, R., Buckley, B., ... Stautner, E. W. (2017). High power density superconducting rotating machines - development status and technology roadmap. *Superconductor Science and Technology, 30*(12), 123002. doi:10.1088/1361-6668/aa833e. (Cit. on pp. 10, 11, 23–25, 27, 28)

Hearn, E. J. (J. (1997). *Mechanics of materials 1: An introduction to the mechanics of elastic and plastic deformation of solids and structural materials*. Butterworth-Heinemann. (Cit. on pp. 50, 51).

Husain, T., Tekgun, B., Sozer, Y., & Hamdan, M. (2017). Comparison of axial flux machine performance with different rotor and stator configurations. *2017 IEEE International Electric Machines and Drives Conference (IEMDC)*, 1–8. doi:10.1109/IEMDC.2017.8002354. (Cit. on p. 32)

Inácio, D., Inácio, S., Pina, J., Valtchev, S., Neves, M. V., Martins, J. F. A., & Leão Rodrigues, A. (2009). Conventional and hts disc motor with pole variation control. *48*(3), 513–518. doi:10.1109/POWERENG.2009.4915250. (Cit. on pp. 52, 54, 55)

Inácio, D., Pina, J. M., Luis, G., Martins, J. F., Ventim-Neves, M., & Álvarez, A. (2011). Experimental characterization of a conventional (aluminum) and of a superconducting (YBCO) axial flux disc motor. *IEEE Transactions on Applied Superconductivity*, *21*(3), 1146–1150. doi:10.1109/TASC.2010.2098832. (Cit. on p. 53)

Inácio, D. D. P. (2014). *Estudo do Motor em Disco com o Rotor em Alumínio e em Supercondutor Multi-semente* (Doctoral dissertation, Faculdade de Ciências e Tecnologia da Universidade Nova de Lisboa). (Cit. on pp. 8, 53).

Jensen, B. B., & Masson, P. J. (2012). *History and latest development of superconducting machines*. Retrieved February 21, 2022, from http://richard.grisel.free.fr/ICEM2012/TUTORIALS/TUT5.pdf. (Cit. on p. 11)

Kleiner, R., & Buckel, W. (2016). *Superconductivity: an introduction*. Wiley-VCH. (Cit. on pp. 3–5, 14, 16).

Kohnke, P. (1999). *ANSYS: Theory Reference*. Ansys, Inc. (Cit. on pp. 47, 49, 50, 52).

Kotari, M., Kojima, H., Hayakawa, N., Endo, F., & Okubo, H. (2010). Development of 2 MVA Class Superconducting Fault Current Limiting Transformer (SFCLT) with YBCO Coated Conductors. *Journal of Physics: Conference Series*, *234*(3). doi:10.1088/1742-6596/234/3/032070. (Cit. on p. 12)

Koutromanos, I. (2018). *Fundamentals of Finite Element Analysis: Linear Finite Element Analysis*. Wiley. (Cit. on p. 41).

London, F., & London, H. (1935). The electromagnetic equations of the supraconductor. *Proceedings of the Royal Society of London. Series A - Mathematical and Physical Sciences*, *149*, 71–88. doi:10.1098/rspa.1935.0048. (Cit. on p. 4)

Lourenço, J. M. (2021). *The NOVAthesis LaTeX Template User's Manual*. NOVA University Lisbon. Retrieved from https://github.com/joaomlourenco/novathesis/raw/master/template.pdf. (Cit. on p. iii)

Malozemoff, A. (2012). Second-generation high-temperature superconductor wires for the electric power grid. *Annual Review of Materials Research*, *42*(1), 373–397. doi:10.1146/annurev-matsci-100511-100240. (Cit. on pp. 4, 9–14, 16)

Masson, P. J., Soban, D. S., Upton, E., Pienkos, J. E., & Luongo, C. A. (2005). HTS motors in aircraft propulsion: Design considerations. *IEEE Transactions on Applied Superconductivity*, *15*(2 PART II), 2218–2221. doi:10.1109/TASC.2005.849616. (Cit. on p. 32)

Meinert, M., Henning, U., Schlosser, R., & Leghissa, M. (2002). Hts-transformers for electric rail vehicles. *RTR*. (Cit. on p. 12).

Melhem, Z. (2012). *High temperature superconductors (hts) for energy applications*. Woodhead Publishing. (Cit. on pp. 4, 10, 11, 20, 33).

Moore, S. K. (2018). The troubled quest for the superconducting wind turbine. Retrieved August 18, 2021, from https://spectrum.ieee.org/the-troubled-quest-for-the-superconducting-wind-turbine. (Cit. on p. 26)

Moran, M. J., Shapiro, H. N., Boettner, D. D., & Bailey, M. B. (2014). *Fundamentals of Engineering Thermodynamics* (8th ed.). Wiley. (Cit. on pp. 37, 38).

Oliveira, R. A., Berger, D., Schultz, L., Stephan, R. M., & Ferreira, A. C. (2015). Finite element analysis of the forces developed on linear induction motors. *2015 IEEE 13th Brazilian Power Electronics Conference and 1st Southern Power Electronics Conference, COBEP/SPEC 2016*. doi:10.1109/COBEP.2015.7420063. (Cit. on pp. 17, 18)

Onnes, H. K. (1913). *Investigations into the proprieties of substances at low temperatures, which have led, amongst other things, to the preparation of liquid helium*. (Cit. on p. 3).

Pina, J. M. M. (2010a). *Desenho e Modelização de Sistemas de Energia Empregando Materiais Supercondutores de Alta Temperatura* (Doctoral dissertation, Faculdade de Ciências e Tecnologia da Universidade Nova de Lisboa). (Cit. on pp. 6, 7).

Pina, J. M. M. (2010b). Motor Polifásico com Número de Pólos Variáveis. Organização Mundial da Propriedade Intelectual. (Cit. on pp. 4, 30, 52).

Poole Jr., C. P., Farach, H. A., Creswick, R. J., & Prozorov, R. (2007). *Superconductivity*. Elsevier. (Cit. on pp. 4, 6, 7).

Rogalla, H., & Kes, P. H. (2011). *100 Years of Superconductivity*. CRC Press. (Cit. on pp. 3, 4, 10–16).

Sayed, E., Abdalmagid, M., Pietrini, G., Sa'adeh, N.-M., Callegaro, A. D., Goldstein, C., & Emadi, A. (2021). Review of electric machines in more/hybrid/turbo electric aircraft. *IEEE Transactions on Transportation Electrification*, 1–1. doi:10.1109/TTE.2021.3089605. (Cit. on pp. 27, 28)

Seidel, P. (2015). *Applied Superconductivity*. Wiley-VCH. (Cit. on pp. 14–23).

Staines, M. P., Jiang, Z., Glasson, N., Buckley, R. G., & Pannu, M. (2015). *High-temperature superconducting (HTS) transformers for power grid applications*. doi:10.1016/B978-1-78242-029-3.00012-1. (Cit. on p. 12)

Steinmetz, C. P. (1984). On the law of hysteresis. *Proceedings of the IEEE*, *72*(2), 197–221. doi:10.1109/PROC.1984.12842. (Cit. on p. 36)

Sun, J., Sanz, S., & Neumann, H. (2015). Conceptual design and thermal analysis of a modular cryostat for one single coil of a 10 MW offshore superconducting wind turbine. *IOP Conference Series: Materials Science and Engineering*, *101*(1). doi:10.1088/1757-899X/101/1/012088. (Cit. on p. 25)

Teixeira-Dias, F., Pinho-da-Cruz, J., Valente, R. F., & Sousa, R. A. (2010). *Método dos Elementos Finitos Técnicas de Simulação Numérica em Engenharia*. Lidel. (Cit. on pp. 41, 42, 46).

Terao, Y., Kong, W., Ohsaki, H., Oyori, H., & Morioka, N. (2018). Electromagnetic Design of Superconducting Synchronous Motors for Electric Aircraft Propulsion. *IEEE Transactions on Applied Superconductivity*, *28*(4), 4–8. doi:10.1109/TASC.2018.2823503. (Cit. on p. 28)

Thinkham, M. (1996). *Introduction to superconductivity*. McGraw-Hill: McGraw-Hill. (Cit. on pp. 4, 6, 8).

Vajda, I., Szalay, A., Göbl, N., Meerovich, V., & Sokolovsky, V. (1999). Requirements for the industrial application of superconducting rotating electrical machines. *IEEE Transactions on Applied Superconductivity*, *9*, 1225–1228. doi:10.1109/77.783521. (Cit. on p. 10)

Ventura, G., & Risegari, L. (2008). *The Art of Cryogenics - Low-Temperature Experimental Techniques*. Elsevier. (Cit. on pp. 18–20).

Yuan, W., & Zhang, M. (2015). Superconducting Magnetic Energy Storage (SMES) Systems. *Handbook of Clean Energy Systems*. doi:10.1002/9781118991978.hces210. (Cit. on p. 13)

I

Machine Schematic

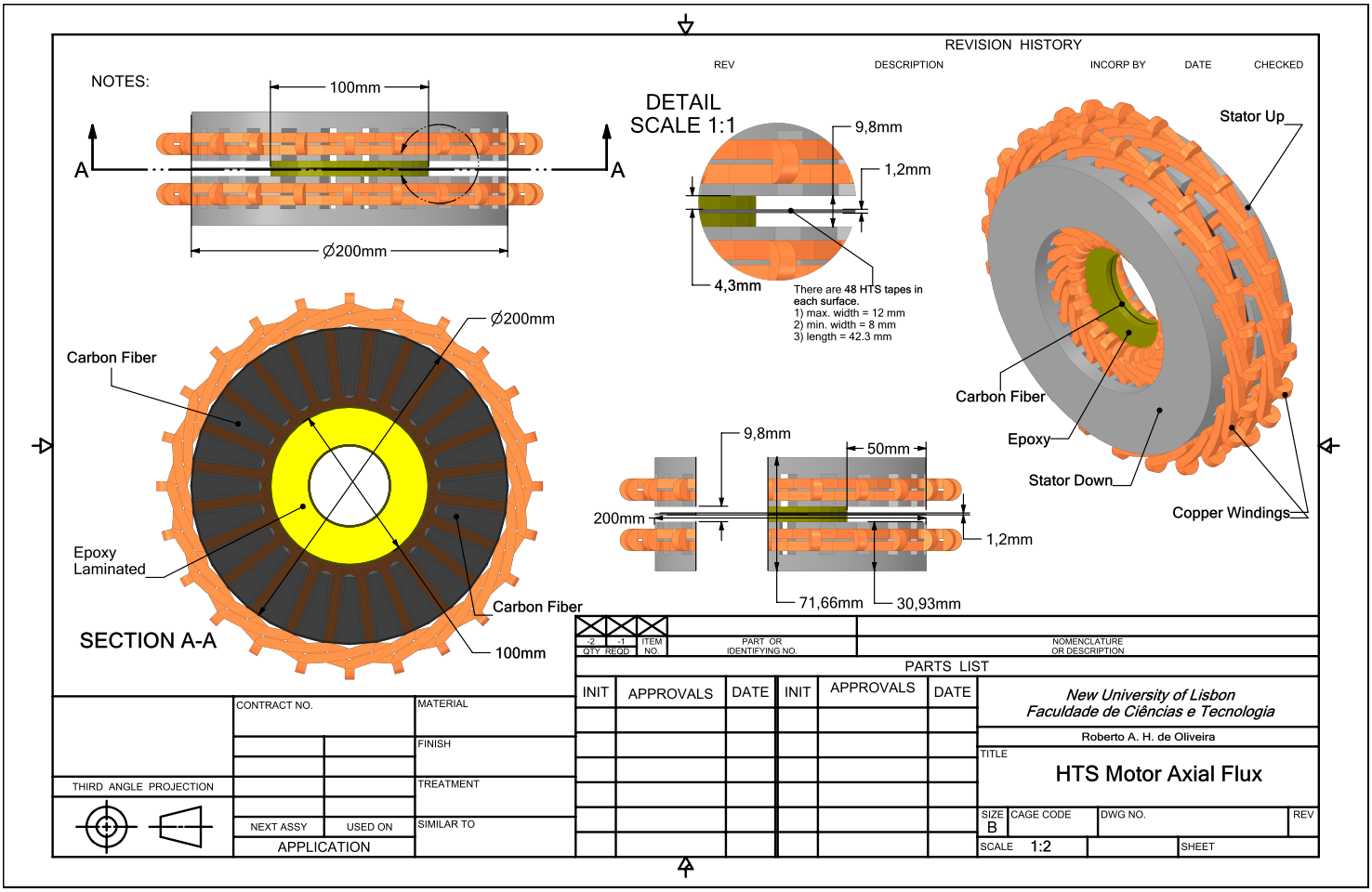

II

Simulation Results

II.1 Thermal Analysis

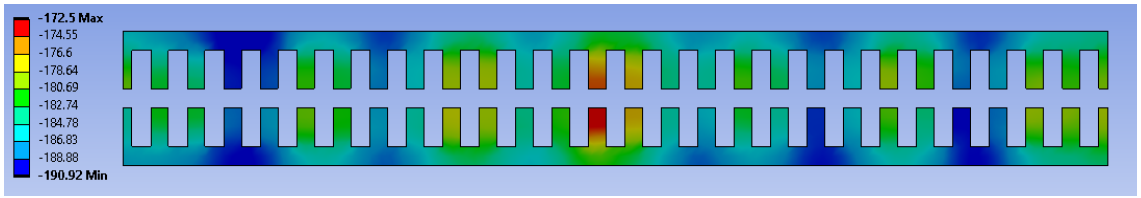

(a) Two-poles.

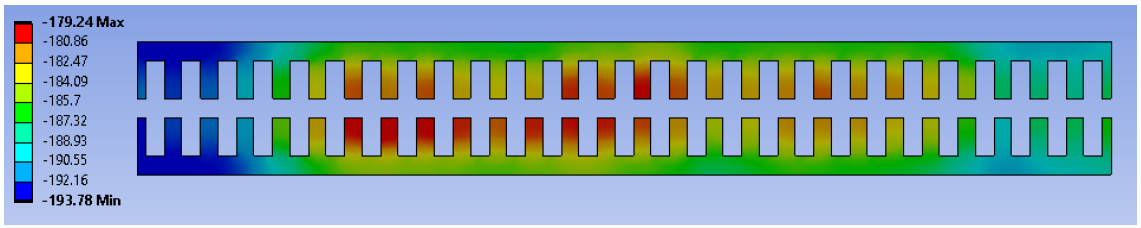

(b) Four-poles.

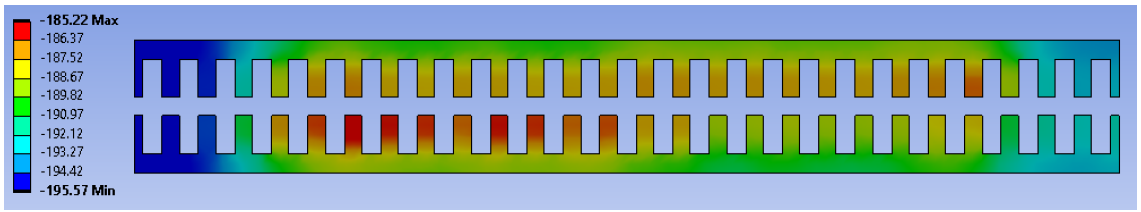

(c) Eight-poles.

Figure II.1: Topology 2 (horizontally laminated) AFSM semi-stator temperature in °C distribution at 30 s.

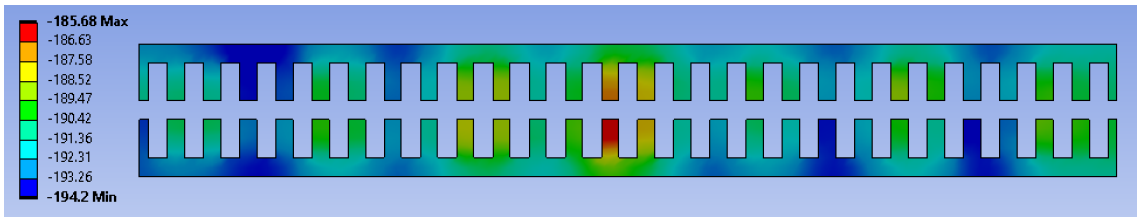

(a) Two-poles.

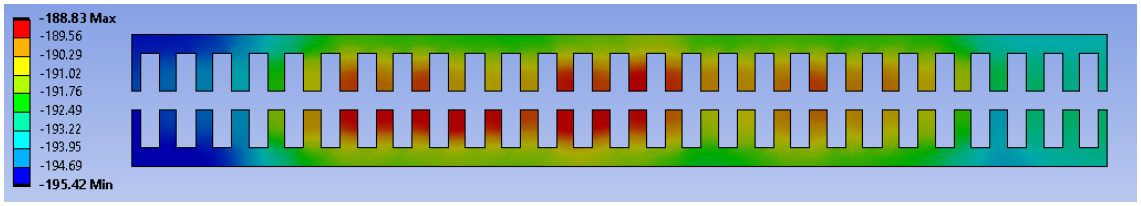

(b) Four-poles.

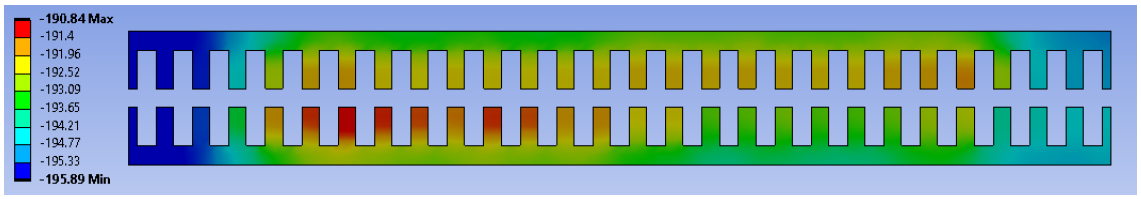

(c) Eight-poles.

Figure II.2: Topology 3 (vertically laminated in y-direction) AFSM semi-stator temperature in °C distribution at 30 s.

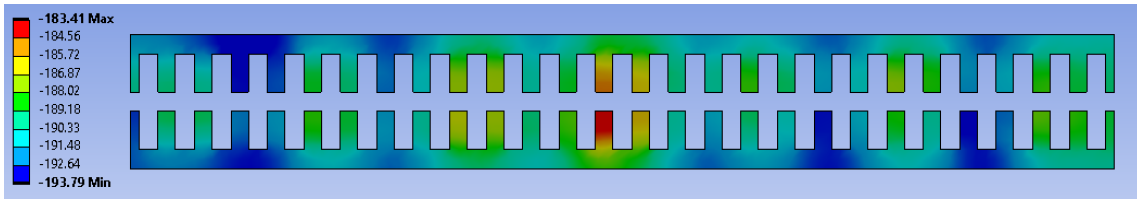

(a) Two-poles.

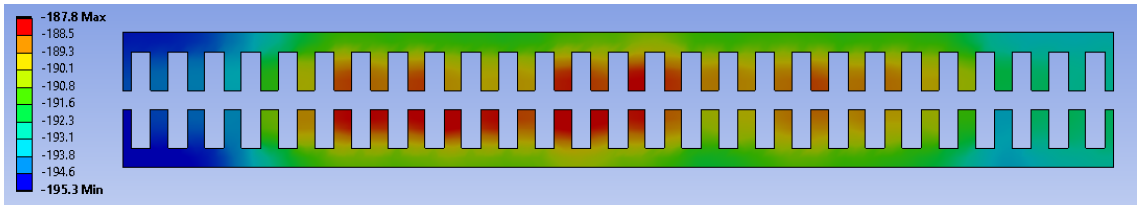

(b) Four-poles.

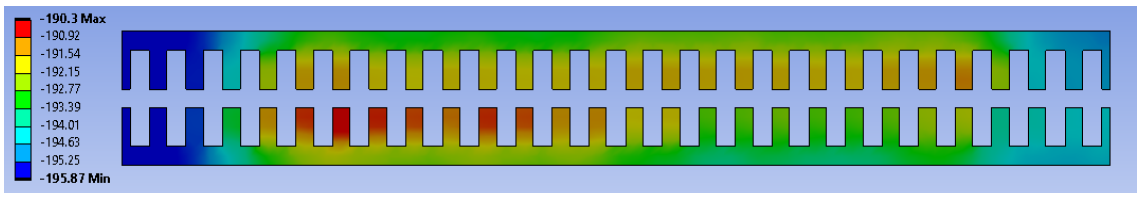

(c) Eight-poles.

Figure II.3: Topology 4 (vertically laminated in x-direction) AFSM semi-stator temperature in °C distribution at 30 s.

II.2 Structural Analysis

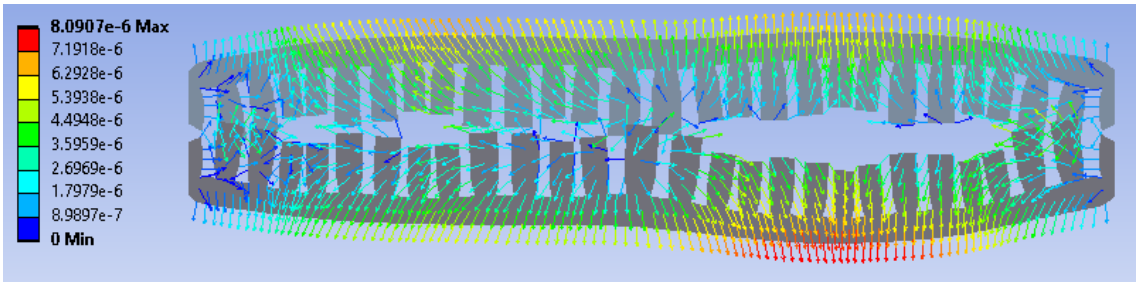

(a) Two-poles.

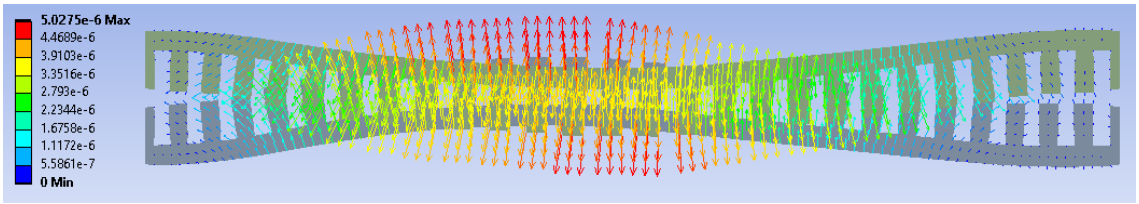

(b) Four-poles.

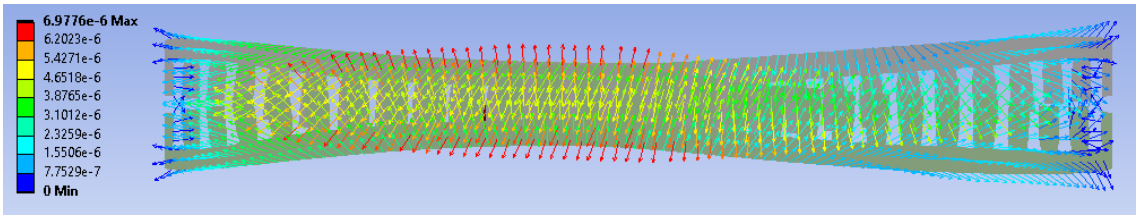

(c) Eight-poles.

Figure II.4: Topology 2 (horizontally laminated) AFSM semi-stator deformation displacement in meters at 30 s. The stator deformation in this figure is amplified in order to evaluate the forces direction.

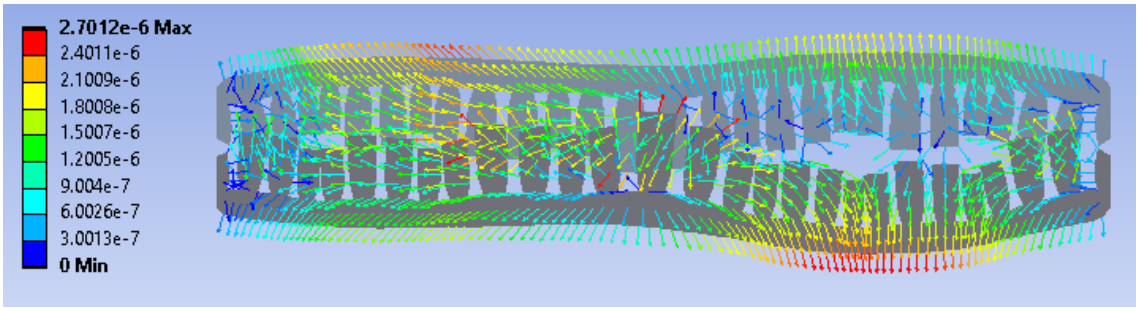

(a) Two-poles.

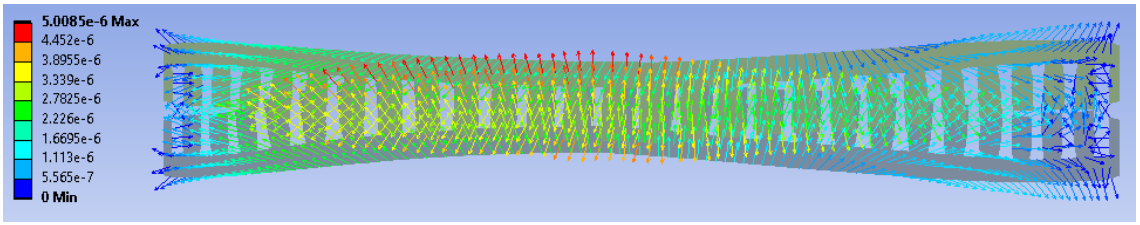

(b) Four-poles.

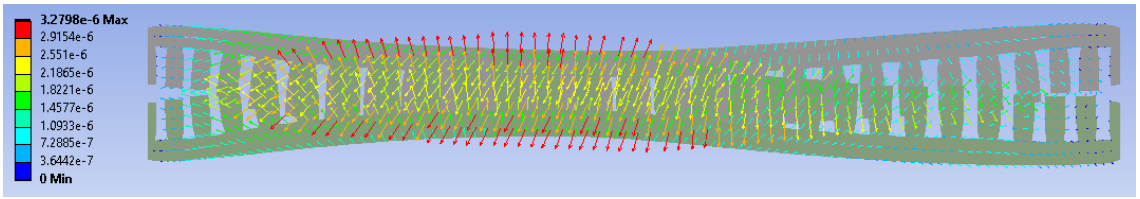

(c) Eight-poles.

Figure II.5: Topology 3 (vertically laminated in y-direction) AFSM semi-stator deformation displacement in meters at 30 s. The stator deformation in this figure is amplified in order to evaluate the forces direction.

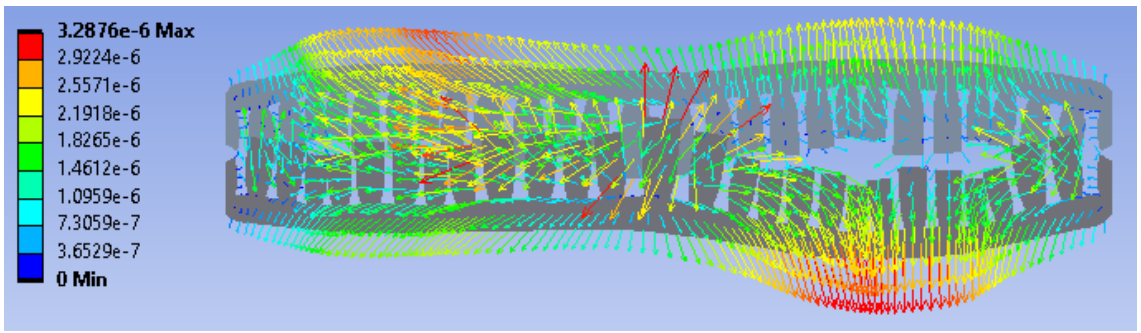

(a) Two-poles.

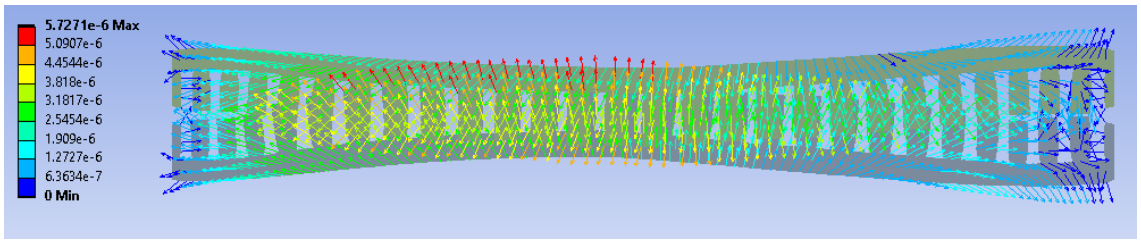

(b) Four-poles.

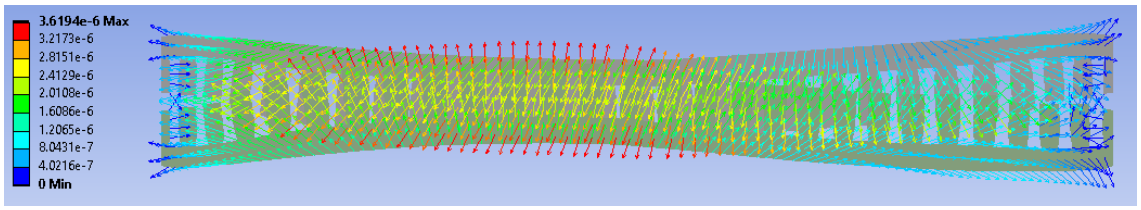

(c) Eight-poles.

Figure II.6: Topology 4 (vertically laminated in x-direction) AFSM semi-stator deformation displacement in meters at 30 s. The stator deformation in this figure is amplified in order to evaluate the forces direction.